TECHNISCHE UNIVERSITÄT
ILMENAU

Stefan Moldenhauer

ANALYSIS AND DEVELOPMENT
OF THE PULSE TUBE ENGINE

Analysis and development of the pulse tube engine

DISSERTATION

zur Erlangung des akademischen Grades

DOKTORINGENIEUR

(Dr.-Ing.)

vorgelegt der

Fakultät für Maschinenbau der

Technischen Universität Ilmenau

von Herrn

Dipl.-Phys. Stefan Moldenhauer,

geboren am 29.01.1980 in Rudolstadt, Deutschland

Gutachter

Prof. Dr. rer. nat. habil. André Thess

Prof. Dr.-Ing. habil. Salman Ajib

Dr.-Ing. Wilhelm Tegethoff

Die Arbeit wurde am 8. Februar 2013 eingereicht.

Die wissenschaftliche Aussprache fand am 15. April 2013 statt.

Danksagung

Zusammenfassung

Thermische Energiewandlungsprozesse werden für gewöhnlich von einer beträchtlichen Menge Abwärme begleitet, welche oft ungenutzt an die Umgebung abgegeben wird. Ein Verbrennungsmotor wandelt beispielsweise nur etwa ein Drittel der ihm zugeführten Verbrennungswärme in nutzbare mechanische oder elektrische Energie um. Etwa zwei Drittel der chemischen Kraftstoffenergie werden als Abwärme abgegeben. Die Rückgewinnung von Energie aus dem verbrennungsmotorischen Abgas ist ein Weg, um den Kraftstoffverbrauch zu senken und zu einer vernünftigen Verwendung der Energieressourcen beizutragen.

Die vorliegende Dissertationsschrift hat die Analyse und Entwicklung einer neuen und bisher kaum erforschten Technologie − den Pulsrohrmotor − zum Ziel, der für niedrigtemperierte Abwärme angewandt werden soll. Um das zu erreichen, besteht diese Arbeit aus einem theoretischen und einem experimentellen Teil. Sowohl ein analytisches als auch ein numerisches Simulationsmodell des Pulsrohrmotors werden entwickelt, um sein thermodynamisches Arbeitsprinzip aufzuklären und Vorhersagen über seine Leistung und Effizienz bei Variation von Design und Arbeitsbedingungen zu treffen. Die theoretischen Ergebnisse werden benutzt, um einen Experimentalpulsrohrmotor im Labor aufzubauen. Dieser verwendet unter Druck stehendes Helium als Arbeitsgas und ist mit einer Vielzahl von Sensoren zur Messung von Temperatur, Druck und Leistung ausgestattet, was einen Vergleich der gemessenen Motorleistung mit den theoretischen Vorhersagen ermöglicht.

In der Arbeit wird erstmalig gezeigt, dass die Anordnung von Pulsrohr und Regenerator eine thermodynamische Asymmetrie bewirkt, welche den grundlegenden Funktionsmechanismus des Pulsrohrmotors darstellt und der Regenerator − im Gegensatz zum Stirlingmotor − für dessen Funktion essentiell ist. Es wird analytisch bewiesen, dass der Pulsrohrmotor intrinsisch irreversibel arbeitet. Eine Relation für das zum Betrieb der Maschine minimal benötigte Temperaturverhältnis von Wärmequelle zu Wärmesenke wird analytisch abgeleitet und anhand des im Labor aufgebauten Pulsrohrmotors experimentell bestätigt.

Aus den theoretischen und experimentellen Leistungsdaten werden die Eigenschaften des Pulsrohrmotors bestimmt und Beschränkungen seiner Effizienz aufgezeigt. Der im Labor aufgebaute Pulsrohrmotor besitzt eine maximale Nettoleistung von 6 W bei einer Nettoeffizienz von 8%. Um Leistung und Effizienz zu erhöhen, werden Vorschläge für ein verbessertes Design geschlussfolgert und für die Entwicklung eines leistungsstarken Pulsrohrmotors benutzt. Weiterhin wird das Potential des Pulsrohrmotors für dessen Anwendung in der Rückgewinnung verbrennungsmotorischer Abgasenergie diskutiert und mit dem thermoelektrischen Energiewandler verglichen.

Résumé

Les procédés de conversion de l'énergie thermique sont généralement accompagnés d'importantes pertes de chaleur, souvent rejetée dans l'environnement, inutilisée. Un moteur à combustion interne, par exemple, ne convertit qu'environ un tiers de l'énergie issue de la combustion en énergie mécanique ou énergie électrique utilisable. Environ deux tiers de l'énergie chimique du combustible sont rejetés comme chaleur perdue. La récupération de l'énergie du gaz d'échappement du moteur à combustion interne est un moyen de réduction de la consommation en carburant et contribue à l'utilisation des sources d'énergie de façon économe.

Cette thèse de doctorat a pour objectif l'analyse et le développement d'une nouvelle technologie peu étudiée jusqu'à présent - le moteur à tube à gaz pulsé - en ce qui concerne son utilisation pour la récupération de la chaleur perdue. Pour cela, ce travail se compose d'une partie théorique et d'une partie expérimentale. Un modèle analytique et un modèle numérique du moteur à tube à gaz pulsé sont développés et utilisés pour expliquer son principe de fonctionnement thermodynamique et prédire sa performance et son efficacité, en fonction de la variation de ses caractéristiques de construction et de son mode opératoire. Les résultats de l'étude théorique sont utilisés pour la réalisation d'un moteur à tube à gaz pulsé expérimental à l'échelle du laboratoire. Ce moteur fonctionne à l'hélium sous pression et est équipé d'une multitude de capteurs pour la mesure de la température, de la pression et de la puissance, permettant une comparaison de la performance mesurée du moteur expérimental aux prédictions théoriques.

Dans ce travail, il est montré pour la première fois, que la combinaison du tube à gaz pulsé et du régénérateur conduit à une asymétrie thermodynamique, ce qui constitue le principe de fonctionnement du moteur à tube à gaz pulsé et le régénérateur est - contrairement au moteur Stirling - essentiel pour son fonctionnement. Il est prouvé analytiquement que le moteur à tube à gaz pulsé a un fonctionnement intrinsèquement irréversible. Le rapport minimal de la température de la source de chaleur à celle du dissipateur thermique, nécessaire au fonctionnement du moteur, est établi analytiquement et validé expérimentalement en utilisant le moteur à tube à gaz pulsé à l'échelle du laboratoire.

Les propriétés du moteur à tube à gaz pulsé sont déduites des résultats théoriques et expérimentaux de performance, et les limites de son efficacité sont cernées. Le moteur à tube à gaz pulsé construit au laboratoire dispose d'une puissance maximale nette de $6\,\mathrm{W}$ pour une efficacité nette de 8%. Afin d'augmenter la performance et l'efficacité, des suggestions sont proposées et utilisées pour le développement d'un moteur à tube à gaz pulsé performant. En outre, le potentiel d'application du moteur à tube à gaz pulsé pour la récupération de l'énergie du gaz d'échappement du moteur à combustion interne est discuté et comparé à celui du convertisseur d'énergie thermoélectrique.

Abstract

Thermal energy conversion processes are usually accompanied by considerable amounts of waste heat, which are often released into the environment unutilized. An internal combustion engine, for instance, only converts about one third of the supplied combustion heat into usable mechanical or electrical energy. About two third of the fuel's chemical energy are released as waste heat. Recovering energy from the exhaust gas of an internal combustion engine is one way to reduce fuel consumption and to contribute to a reasonable use of energy resources.

This PhD dissertation aims to analyze and develop a new and to date rarely investigated technology − the pulse tube engine − with respect to its applicability for low grade waste heat recovery. To do so, this work consists of a theoretical and an experimental part. An analytical and a numerical simulation model of the pulse tube engine are developed and used to clarify its thermodynamic working principle and to predict its power output and efficiency under variation of design features and operating conditions. The results of the theoretical investigations are used to build an experimental pulse tube engine at a laboratory scale. It uses pressurized helium as working gas and is equipped with a high number of sensors for the measurement of temperature, pressure and power, which enables a comparison of the measured engine performance with the theoretical predictions.

In this work, it is shown for the first time that the combination of a pulse tube and a regenerator results in a thermodynamic asymmetry, which forms the underlying working principle of the pulse tube engine, and the regenerator is − in contrast to the Stirling engine − essential for its functioning. It is proven analytically that the pulse tube engine's operation is intrinsically irreversible. A relation for the minimal necessary temperature ratio of heat source to heat sink, which enables the engine to operate, is derived analytically and confirmed experimentally using the built laboratory-scale pulse tube engine.

From the theoretical and experimental performance results, the properties of the pulse tube engine are derived and limitations for its efficiency are outlined. The pulse tube engine built to laboratory scale has a maximum net power output of 6 W at a net efficiency of 8%. In order to increase power output and efficiency, suggestions for an advanced design are concluded and used for the development of a powerful pulse tube engine. Furthermore, the potential of the pulse tube engine for its application in energy recovery from the internal combustion engine's exhaust gas is discussed and compared to that of the thermoelectric energy converter.

Contents

List of Symbols

Roman Symbols

Δc_p	error of bar. spec. heat cap.
Δt_{max}	maximum time increment
Δt_{min}	minimum time increment
$\dot{E}$	energy flux
$\dot{E}_{cyc}$	cycle energy flux
$\dot{H}$	enthalpy flux
$\dot{m}$	mass flux
$\dot{m}_{chx}$	mass flux via chx
$\dot{m}_{hhx}$	mass flux via hhx
$\dot{m}_{tr}$	mass flux threshold value
$\dot{Q}$	heat flux
$\dot{Q}_{cg}$	conductive heat flux gas
$\dot{Q}_{cm}$	conductive heat flux material
$\dot{Q}_{cyc}$	cycle heat flux
$\dot{Q}_{ext}$	external heat flux
$\dot{Q}_{hx,id}$	ideal gas-material heat flux
$\dot{Q}_{hx,re}$	real gas-material heat flux
$\dot{Q}_{hx}$	gas-material heat flux
$\dot{Q}_{in}$	thermal power input
$\dot{Q}_t$	total heat flux
$\dot{S}$	entropy flux
$\dot{S}_{cg}$	conductive entropy flux gas
$\dot{S}_{hx}$	gas-material entropy flux
$\dot{W}$	compr./exp. (pV-) power
$\frac{dS_{irr}}{dt}$	entropy production rate
A, B	fitting parameters
A_f	free flow area
a_i, b_i	series exp. coefficients

A_m	cross-section area material
A_{hx_0}	min. cyl. heat transfer area
A_{hx_d}	displacement area
A_{hx}	heat transfer area
b	cylinder bore
c_m	specific heat capacity material
c_p	barometric spec. heat capacity
c_v	volumetric spec. heat capacity
$c_{1/2/3}$	fitting parameters
C_c	compression constant
C_e	expansion constant
$c_{h/k/l}$	fitting parameters
C_{hp}	high pressure constant
C_{lp}	low pressure constant
d	diameter
d_b	bearing diameter
d_w	wire diameter
d_h	hydraulic diameter
d_{pt}	pulse tube diameter
d_{reg}	regenerator diameter
e	porosity
f	operating frequency
f_1, f_2	efficiency functions
F_f	flow friction force
f_f	flow friction factor
F_f^{cyl}	friction force cylinder
F_I	momentum force
F_p	pressure force
f_s	solid body friction factor

L	length	Q_{cyl}	heat transf. per cycle cylinder
L_r	piston rod length	Q_{ex}	released heat via exhaust gas
L_{pt}	pulse tube length	Q_{hhx}	heat transf. per cycle hhx
L_{reg}	regenerator length	Q_{in}	supplied heat
m	gas mass	Q_{pt}	heat tr. per cycle pulse tube
M_f^{sh}	shaft friction momentum	Q_{reg}	heat tr. per cycle regenerator
M_{br}	brake momentum	Q_r	recovered waste heat
M_{dr}	drive momentum	r_c	compression ratio
n	number of sub-control volumes	r_d	distribution ratio
n_m	mesh number	R_s	specific gas constant
n_p	polytropic exponent	r_{cr}	crank ratio
Nu	Nusselt number	Re	Reynolds number
p	pressure	S	entropy gas
p^0	pressure of reference state	s	stroke length
p_a	ambient pressure	S^0	entropy of reference state
p_c	compression pressure	$S_{irr,chx}$	entropy production chx
p_e	expansion pressure	$S_{irr,cyl}$	entropy production cylinder
p_f	filling pressure	$S_{irr,hhx}$	entropy production hhx
P_g	gross power output	$S_{irr,pt}$	entropy production pulse tube
P_n	net power output	$S_{irr,reg}$	entropy production regenerator
p_{1-2}	experiment: pressure sensors	$S_{irr,t}$	total entropy production
$p_{1/2/3/4}$	pressure at states $1/2/3/4$	T	(gas) temperature
P_{br}	brake power	t	time variable
P_{dr}	drive power	T^0	temperature of reference state
$P_{l,cd}$	heat conduction power loss	T_c	heat sink temperature
$P_{l,ext}$	external power loss	T_g	gas temperature
$P_{l,fg}$	gas friction power loss	T_h	heat source temperature
$P_{l,hx}$	heat transfer power loss	T_m	material temperature
$P_{l,int}$	internal power loss	T_{chx}	gas temperature chx
p_{max}	maximum pressure	T_{cyl}	gas temperature cylinder
p_{min}	minimum pressure	T_{hhx}	gas temperature hhx
P_{sh}	shaft power output	T_{m,chx_1}	material temperature chx$_1$
Pr	Prandtl number	T_{m,chx_2}	material temperature chx$_2$
Q_h	supplied combustion heat	$T_{m,cyl}$	material temperature cylinder
Q_{c1}	released heat via cooling water	$T_{m,hhx}$	material temperature hhx
Q_{c2}	released heat via cooling water	$T_{m,pt}$	mat. temperature pulse tube
Q_{chx}	heat transf. per cycle chx	$T_{m,reg}$	mat. temperature regenerator

$T_{pt,c}$	compr. gas temp. pulse tube	χ_{cyl}	linear perturb. cylinder heat
$T_{pt,e}$	exp. gas temp. pulse tube	χ_{hhx}	linear perturbation hhx heat
T_{pt}	gas temperature pulse tube	χ_{pt}	lin. perturb. pulse tube heat
T_{reg}	gas temperature regenerator	χ_{pV}	linear perturbation pV-work
U	internal energy gas	F	correction function
u	gas velocity	ϵ	compression/expansion factor
U_m	internal energy material	ϵ_c	compression factor
u_p	piston velocity	ϵ_e	expansion factor
V	gas volume	η_g	gross efficiency
V^0	volume of reference state	η_n	net efficiency
V_0	dead volume	η_{sh}	shaft efficiency
V_0^a	known dead volume	η_{th}	thermal efficiency
V_0^b	unknown dead volume	$\eta_{th}^{<}$	lower thermal efficiency
V_m	material volume	$\eta_{th}^{=}$	upper thermal efficiency
V_{1-5}	experiment: valves	Γ	smoothing function
V_{chx_1}	gas volume chx$_1$	γ	heat transfer capacity
V_{chx_2}	gas volume chx$_2$	$\hat{p}$	pressure amplitude
V_d	displacement volume	κ	adiabatic exponent
V_{hhx}	gas volume hhx	λ	boundary condition factor
V_{hx}	total heat exchanger gas vol.	λ_g	heat conductivity gas
V_{max}	max. engine gas volume	λ_m	heat conductivity material
V_{min}	min. engine gas volume	λ_{Υ}	averaging factor
V_{pt}	pulse tube gas volume	μ	dynamical viscosity
V_{reg}	regenerator gas volume	ν_i	angular velocity bearing
W_m	mechanical work	ω	angular frequency
W_c	compression work	ϕ	piston starting position
W_e	expansion work	Π	pressure ratio
W_{pV_l}	linear component of pV-work	ψ	heat transfer module
W_{pV}	pV-work	ρ	gas density
W_r	recovered mechanical work	ρ_m	material density
x	space variable	σ	sign function
x_{pt}	pulse tube position	τ	temperature ratio
x_{reg}	regenerator position	τ_0	minimal temperature ratio
		τ_{opt}	optimal temperature ratio

Greek Symbols

		Υ_1	first order expansion
α	heat transfer coefficient	Υ_2	second order expansion
χ_{chx}	linear perturbation chx heat	ζ	heat transfer module

Chapter 1

Introduction

"Das Glück des Forschers besteht nicht darin eine Wahrheit zu besitzen, sondern die Wahrheit zu erringen. In diesem fortschreitenden, erfolgreichen Suchen nach der Wahrheit, da liegt die eigentliche Befriedigung... Dieses erfolgreiche Arbeiten, das ist dasjenige, was den Quell jeder Anstrengung und auch den Quell eines jeden geistigen Genusses darstellt. Wenn der Quell versiegt, wenn die Wahrheit gefunden ist, dann ist es zu Ende, dann kann man sich geistig und körperlich schlafen legen. Aber dafür ist gesorgt, dass wir das nicht erleben, und darin besteht unser Glück."

− Max Planck, German physicist. Berlin 1942 −

1.1   Thermal energy conversion and waste heat

Thermal energy conversion processes are usually accompanied by considerable amounts of waste heat, which are often released into the environment unutilized. An Internal Combustion Engine (ICE), for instance, only converts about one third of the supplied combustion heat Q_h into usable mechanical work W_m. Two third of the fuel's energy are released as waste heat − about one third via the cooling water Q_{c1} and one third via the exhaust gas Q_{ex} [1]. Fig. 1.1 illustrates the thermodynamic situation. The cooling water temperature of an Otto engine is slightly higher than that of a Diesel engine [1]. The mean temperature of the cooling water is about $90\,°\text{C}$.

In passenger cars the cooling water waste heat is used for heating purposes. A further conversion into mechanical or electrical energy is, due to the low temperature, technically difficult and not economical [2].

The waste heat released from the internal combustion engine via the exhaust gas is on a temperature level which is sufficient for its further conversion into a usable form of energy. This is state of the art and done with the installation of a gas turbine in the exhaust gas system of the engine. The turbine converts a portion of the exhaust gas

1
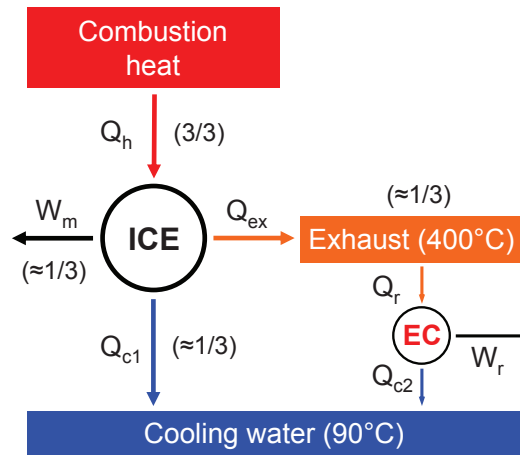
Figure 1.1: Principle of Internal Combustion Engine's (ICE) waste heat recovery. Combustion heat Q_h is delivered to the ICE. About one third of the fuel's energy is converted into usable mechanical work W_m. Two third of the supplied energy are released unused via the cooling water Q_{c1} and the exhaust gas Q_{ex}. A portion of the exhaust gas waste heat Q_r can be recovered and converted into mechanical work W_r by an additional Energy Converter (EC). The EC also releases waste heat Q_{c2} to the cooling water.

waste heat into mechanical work, which is used to drive a turbo compressor charging the engine with compressed fresh air [1]. The turbocharger technology, originally invented for aviation engines, is widely used in the automotive industry, especially in combination with Diesel engines.

Nevertheless, even if a turbocharger reduces the temperature of the exhaust gas, its turbine exit temperature is still at a temperature level which is high enough to be used in an additional thermal energy conversion process. The exhaust gas temperature is − depending on the engine (turbo-charged or uncharged, Otto or Diesel engine) and the mode of operation (full or part load, engine speed) − on a temperature level between $200\,°C$ and $600\,°C$ [3].

Fig. 1.1 shows how the thermal energy of the exhaust gas can be used by an additional Energy Converter (EC). The additional energy converter recovers a portion of the exhaust gas waste heat Q_r and converts it into mechanical work W_r. The waste heat Q_{c2} of the additional energy converter is released to the cooling water of the internal combustion engine. Since the exhaust gas waste heat − having an assumed mean temperature of about $400\,°C$ − allows only for an inefficient usage of this heat, in general, the thermal efficiency of the additional energy converter is quite low. However, even if the additional system converts only 5% of the exhaust gas waste heat into a usable form of energy, such as mechanical work or electrical energy, the fuel efficiency of the entire system, shown in Fig. 1.1, increases by about 1.6%. Harvesting this amount of energy is much less a question of efficiency than of economy relating to the cost of the additional energy converter.

In recent years, the automotive industry has made huge efforts regarding the development of such a working, low-cost additional energy converter. The main pursued technological approaches are (organic) Rankine cycle based systems like [4, 5] and thermoelectric energy converters [6, 7, 8]. However, other heat engines for the usage of internal combustion engine's waste heat, such as [9] are continuously proposed as well.

The working principle of the (organic) Rankine cycle [10, 11] is based on the Clausius-Rankine cycle [12], used in steam power plants for the provision of electrical energy. An organic Rankine cycle does not use water, but an organic substance, e.g. R134a, NH_3 or others [13] as working fluid, thus enabling the utilization of heat energy at low temperatures in an energy conversion process with a phase change. Depending on the working fluid and the temperature of the heat supply, the thermal efficiency and the power output of this technology are quite high [13]. Since numerous components, such as evaporator, fluid pumps, condenser, expansion engine (turbine or piston engine) are required for the process, the procedural effort and technical complexity of the (organic) Rankine cycle are also relatively high.

The second, currently pursued approach to utilize internal combustion engine's waste heat is the application of thermoelectric materials, which enable the direct conversion of heat energy into electric energy, without the detour via a thermo-mechanical process. This technology is preferably applied at low temperature waste heat. Its principle is based on the Seebeck effect [14]. The efficiency of thermoelectric energy converters only covers a single digit percentage range [15], its power output is quite low, and the costs of thermoelectric materials as well as of the auxiliary cooling system are still too high to allow its wide utilization yet [3, 16].

Moreover, the internal combustion engine is a highly dynamic system. In addition to the mentioned temperature range of the exhaust gas, its mass flux also varies in a wide range. As an example, the mass flux of the exhaust gas of a turbo-charged Diesel engine for full load at an engine speed of 3000 rpm and a charging pressure of 2 bar is one order of magnitude higher than for idling at an engine speed of 600 rpm and a charging pressure of 1 bar (bypassed turbocharger). For an Otto engine this ratio is even higher [17]. Thus, the available exhaust gas enthalpy flux is highly variable.

So far, due to the disadvantages of the (organic) Rankine cycle and thermoelectric energy converter in combination with the highly dynamic situation of the exhaust gas of internal combustion engines, both technologies have not been able to establish themselves on a large scale in internal combustion engine's waste heat recovery.

This overview demonstrates that there is a need for alternative concepts of waste heat recovery. The present work is intended to contribute to the solution of this problem.

1.2   The pulse tube engine for waste heat recovery

Since the discussed technologies for the recovery of internal combustion engine's waste heat are unsatisfying, a new concept is needed.

A thermodynamic process with the potential to be a good compromise between simplicity, cost and efficiency, therefore being suitable for internal combustion engine's waste heat utilization, is the pulse tube process. It was invented in the 1960's by Gifford and Longsworth [18] and has since found extensive practical application for cryogenic cooling purposes. So called pulse tube refrigerators have been research and development objects for the last 40 years, e.g. [19, 20, 21, 22], and are employed in cryogenic technologies to provide as one-stage refrigerators temperatures around the condensation temperature of nitrogen (77.2 K at atmospheric pressure) or as two-stage refrigerators temperatures down to the condensation temperature of helium (4.2 K at atmospheric pressure).

The reversing of the pulse tube process enables the design of an astonishingly simple prime mover − the pulse tube engine − for the conversion of externally supplied thermal energy into mechanical energy or, using an electrical generator, into electrical energy. The pulse tube engine, investigated in this work, was first reported by Hamaguchi et al. [23] in 2005. Although the pulse tube engine is thermodynamically similar to the pulse tube refrigerator, its operation and performance is much less understood than for its cryogenic counterpart. The purpose of the present work is to fill this gap by a symbiotic interaction between theory and experiment. It represents the first comprehensive attempt to model and improve the pulse tube engine.

1.2.1   Working principle of the pulse tube engine

A brief introduction of the pulse tube engine's working principle [24] is given below.

The basic engine design is shown in Fig. 1.2. A compression/expansion cylinder
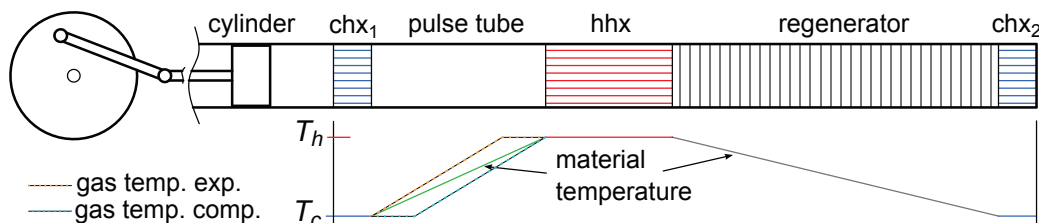
Figure 1.2: Basic design of the pulse tube engine. chx$_1$ − cold heat exchanger 1, chx$_2$ − cold heat exchanger 2, hhx − hot heat exchanger. For the sake of simplification, the material temperature distribution is assumed to be linear in the pulse tube and the regenerator, and spatial constant in the other components. The ideally assumed gas temperature distributions in the pulse tube during compression and expansion are illustrated using dotted lines.

supplies a pressure swing and gas shifting to the connected system consisting of an almost adiabatic buffer space (pulse tube) and an isothermalizer (regenerator). Both components are fluidically linked via a gas heater (hhx) at the temperature T_h, providing the heat input. A gas cooler (chx$_1$) at the temperature T_c is located between cylinder and pulse tube. A heat sink (chx$_2$) at the temperature T_c — to set the depicted material temperature distribution — is located at the cold side of the regenerator. The conversion of compression/expansion work (pV-work) into mechanical work and vice versa is carried out by the resulting pressure force on the piston within the cylinder, which is located at cold temperature level. A generator for the conversion of mechanical energy into electrical energy can be joined to the cylinder/piston configuration via a crank gear mechanism.

The functional principle of the pulse tube engine is based on a broken thermodynamic symmetry. Thermodynamic asymmetry results from the fluidic linkage of the almost adiabatic pulse tube and the almost isothermal regenerator. A simultaneous compression and moving of the working gas into an area of high material temperature is followed by a simultaneous expansion and moving of the working gas into an area of low material temperature. Therefore, the piston moving from its bottom dead center (BDC) to its top dead center (TDC) compresses the working gas and pushes gas from the cylinder via chx$_1$ into the cold side of the pulse tube. Passing chx$_1$, the gas is cooled down to T_c. The situation is illustrated in Fig. 1.2 by the dotted gas temperature distribution in the pulse tube during the compression stroke. Meanwhile, in the pulse tube, gas is compressed and shifted from the cold to the hot side of the tube. Gas leaving the pulse tube at its hot side via hhx takes on heat and enters the hot side of the regenerator with the temperature T_h. The regenerator material, having the depicted material temperature distribution of Fig. 1.2, absorbs heat from the working gas. Thus, the heat taken on in hhx is entirely given off to the regenerator material. The thermal capacity of the regenerator material is high enough to experience no significant temperature swing. Since cold gas was shifted during compression from the cold to the hot side of the pulse tube, it is able to take on heat from the tube's wall material while the piston is moving around TDC (high pressure thermal relaxation). The pressure increases slightly. Now the piston moves from TDC back to BDC which results in an expansion of the working gas flowing from the regenerator via hhx into the hot side of the pulse tube. The situation is illustrated in Fig. 1.2 by the dotted gas temperature distribution in the pulse tube during the expansion stroke. The regenerator material gives back the heat stored during the compression phase. Since the gas entering hhx is already at T_h, it receives only an insignificant amount of heat. Meanwhile, in the pulse tube, gas is expanded and shifted from the hot to the cold side of the tube. Gas

leaving the pulse tube at its cold side via chx$_1$ is cooled and enters the cylinder with the temperature T_c. In the cylinder the gas is further expanded and its temperature goes below T_c. Since hot gas was shifted during expansion from the hot to the cold side of the pulse tube, it is able to give off heat to the tube's wall material while the piston is moving around BDC (low pressure thermal relaxation). The pressure decreases slightly till the initial state is reached again. Absorbing heat at high pressure and rejecting heat at low pressure results in a higher mean pressure during expansion than during compression and in a release of pV-work.

1.2.2 State of knowledge and objectives of this thesis

First concepts of prime movers similar to the pulse tube engine were presented in 1987 by Chen and West [25]. In 1995, Tailer was granted a patent [26] for a heat engine based on a phase delay between pressure fluctuations and heat transfer (thermal lag [27, 28, 29]). A patent describing a device resembling the pulse tube engine was published in 2000 by Hofmann [30]. The concept of the pulse tube engine was first presented in its entirety by Hamaguchi et al. [23] in 2005, and later by Organ [24] in 2007. A number of experimental investigations to characterize the pulse tube engine were also published by Hamaguchi et al. [23, 31]. Since 2007 further patents of the pulse tube engine by Shauwei [32], Shiyoui [33] and Kaiser et al. [34] appeared. A proposition for its application in internal combustion engine's waste heat recovery is reported by Keen et al. [35] and patented by Kaiser et al. [36].

A different concept of the pulse tube engine having two pistons is patented by Ishizaki et al. [37]. This type of pulse tube engine is an extension of the Stirling engine by a pulse tube between the hot heat exchanger and the expansion cylinder of the Stirling engine. An investigation of the pulse tube engine having two pistons is reported by Ki et al. [38]. Moreover, Kaiser et al. [39] patented a version of this type of pulse tube engine using a working fluid with phase change. However, the purpose of this thesis is restricted to an investigation of the pulse tube engine having just one piston and using a working fluid without phase change.

According to work flux measurements of Yoshida et al. [40] in 2009, the pulse tube engine can be classified into the thermoacoustic [41] standing wave engine group [42, 43, 44, 45] with an underlying intrinsically irreversible thermodynamic cycle [46], although the pulse tube engine is − by comparing its working principle with the thermoacoustic engines investigated in [47, 48, 49, 50] − analogous to the Stirling engine [51, 52], not a thermoacoustic device.

However, no full-scale thermodynamic analysis of the pulse tube engine has ever been comprehensively compared with accurate experiments over a wide range of parameters.

Moreover, no relations to calculate the power output and efficiency of the pulse tube engine exist. Up to now the exact influence of design features is not clear and working pulse tube engines are designed through experiments. The object of the present work is to bridge this gap, and to find detailed correlations between design features and working conditions of the pulse tube engine, and its developed power output and efficiency.

This thesis is split into two main goals. The first goal is to get a deep theoretical understanding of the pulse tube engine's underlying thermodynamic process. To do so, an analytical and a numerical model of the pulse tube engine are developed in chapter 2. Both models are used to study the working principle of the engine, to derive relations for its power output and efficiency, and to find pathways for its optimal design. The results of the two approaches are compared and used for the second goal of this thesis, the design of a working engine in chapter 3. In contrast to prior works, in which non-pressurized pulse tube engines using air as working fluid have been built, the development focuses on the design of a pressurized pulse tube engine using helium as working fluid. Compared to the investigated non-pressurized engines of [23, 31, 35, 40] with power outputs of some hundreds of milliwatt the projected power output of the working pulse tube engine in this thesis is in the range of several watts, which will enable obtaining reliable experimental results from the test rig. Furthermore, the present approach has the virtue that all design parameters such as heat transfer areas, diameters, porosity, dead volumes etc. are well known and available for the parametrization of the simulation models. The experimental test engine is equipped with a high number of temperature and pressure sensors, equipment for the measurement of the heat power input and the mechanical power output as well as frequency and crank angle measurement techniques. Furthermore, the test set-up is designed to perform difference power measurements to identify power losses and get access to the power delivered to the piston rod, which is calculated by the numerical simulation model. The measured data, such as the time-dependent pressure, the temperature distribution and the power outputs shall be used to quantify the accuracy of the developed simulation models and to systematically compare the performance of this engine with the theoretical predictions.

The overall aim of this research is to study the working conditions and the performance of the pulse tube engine using theoretical and experimental methods simultaneously. The results are used first to quantify the potential of the pulse tube engine for its usage in internal combustion engine's waste heat recovery, and second to provide general characteristics of the pulse tube engine, which are interesting for other applications as well. In chapter 4 the results and conclusions of this thesis are summarized and discussed. Finally, a concept for an advanced pulse tube engine, resulting from this work is presented.

Chapter 2

Theory of the pulse tube engine

In this chapter the differential equations describing the transient behavior of the pulse tube engine are derived. The purpose is to predict the time-dependent pressure and the time-dependent heat fluxes in the cylinder, the heat exchangers, the pulse tube and the regenerator for prescribed values of the heating and cooling temperatures, filling pressure and operating frequency as well as for specified geometry features and working gas parameters. The differential equations are obtained from the balances for mass, momentum, energy and entropy of the engine components.

(a) Zero-dimensional approach of the analytical model

(b) Mixed zero/one-dimensional approach of the numerical model
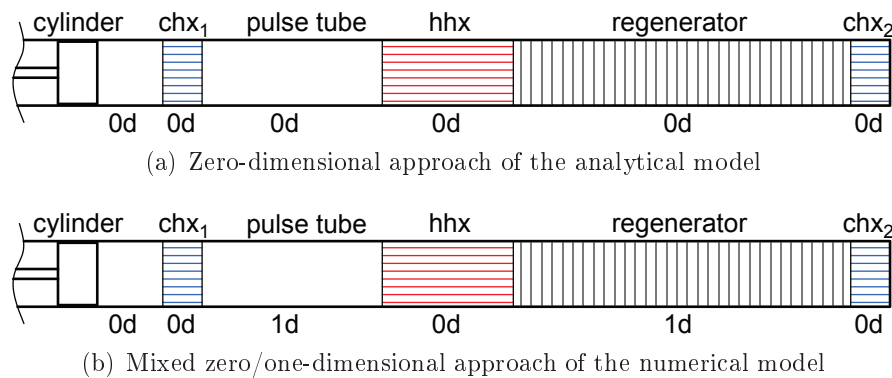
Figure 2.1: Modeling approaches for the pulse tube engine. (a) Zero-dimensional (0d) approach for all engine components used in the analytical model; (b) Zero-dimensional approach for the cylinder and the heat exchangers combined with a one-dimensional (1d) approach for the pulse tube and the regenerator used in the numerical model.

Two modeling approaches are performed. In the first approach all engine components are regarded as zero-dimensional with one representative value of each physical property depending on the time only. A graphical visualization of this method is shown in Fig. 2.1 (a). It is used to develop an analytical model of the pulse tube engine. The second approach is an extension of the zero-dimensional model of Fig. 2.1 (a) by a one-dimensional approach on the thermodynamics of the pulse tube and the regenerator,

where the respective physical properties are time- and space-dependent. A graphical visualization of this method is shown in Fig. 2.1 (b). It is used to develop a numerical model of the pulse tube engine.

2.1   Governing equations

The derivation of the underlying differential equations is based on a control volume analysis [53, 54]. The control volumes are in the case of a zero-dimensional analysis the engine components and in the case of a one-dimensional analysis sub-volumes of the engine component regarded. In order to formulate the governing equations of the pulse tube engine process, the following simplifications are made:

1) The physical properties are assumed to be uniform within the control volume.

2) The working fluid is a perfect gas with constant specific heat capacities c_p, c_v.

3) Kinetic and potential energy changes are disregarded.

4) Pressure wave reflections at the system boundaries are neglected.

5) Only forces parallel to the direction of motion are considered.

6) The mass of the working fluid is constant.

The relative error implied by the use of constant specific heat capacities, within a temperature range of $20\,^\circ$C to $600\,^\circ$C, for the working gas air, is $\frac{\Delta c_p}{c_p} = 5\%$ [55], and is negligible for the working gas helium.

Fig. 2.2 shows the schematic representation of the control volume. The internal energies of the gas and the material are represented by U and U_m. The gas mass content of the control volume is m and its entropy S. Heat can be exchanged between the surroundings and the engine material via the heat flux $\dot{Q}_{ext}$ as well as between the engine material and the working gas via the heat flux $\dot{Q}_{hx}$. The entropy flux due to heat transfer between the gas and the material is represented by $\dot{S}_{hx}$. Entropy fluxes between the material and the surroundings are disregarded. In the cylinder the working gas is charged with the compression/expansion power (pV- power) $\dot{W}$.

Between the control volumes mass fluxes $\dot{m}$, enthalpy fluxes $\dot{H}$ and entropy fluxes $\dot{S}$ are exchanged. Fluxes at the control volume's left side are marked with $'$ and fluxes at the control volume's right side with $''$. Heat and entropy fluxes due to conduction in the gas and the material are denoted with $\dot{Q}_{cg}$, $\dot{S}_{cg}$ and $\dot{Q}_{cm}$. Entropy fluxes in the material are not considered. All entering fluxes are given a positive sign. The kinematical situation of the gas mass m will be discussed in subsection 2.1.5.
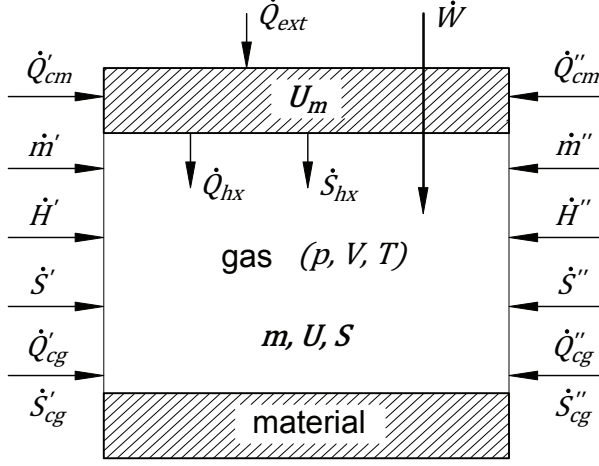
Figure 2.2: Schematic representation of the control volume with internal energies of the gas U and the material U_m as well as the gas mass m and the gas entropy S. Heat and entropy exchanged between gas and material are represented by $\dot{Q}_{hx}$ and $\dot{S}_{hx}$. The heat flux $\dot{Q}_{ext}$ is exchanged between the material and the surroundings. Mass, enthalpy and entropy fluxes between the control volumes are denoted with $\dot{m}$, $\dot{H}$ and $\dot{S}$. Left and right side fluxes are marked with $'$ and $''$, respectively. Heat fluxes due to conduction in the gas and the material are denoted with $\dot{Q}_{cg}$ and $\dot{Q}_{cm}$. Conductive entropy fluxes in the gas are $\dot{S}_{cg}$. The compression/expansion power (pV- power) is represented by $\dot{W}$.

All balances used for the two modeling approaches of the pulse tube engine process are presented in the following subsections.

2.1.1   Mass balance

The temporal change of the gas mass content within the control volume is given by

$$\frac{dm}{dt} = \dot{m}' + \dot{m}''. \tag{2.1}$$

The thermal state equation of a perfect gas [56] with the pressure p, the volume V and the temperature T is represented by $p\,V = m\,R_s\,T$, where R_s is the specific gas constant. The total differential of the thermal state equation is

$$dm = m\left(\frac{dp}{p} + \frac{dV}{V} - \frac{dT}{T}\right). \tag{2.2}$$

Inserting Eq. (2.2) in Eq. (2.1) leads to

$$\frac{dm}{dt} = m\left(\frac{1}{p}\frac{dp}{dt} + \frac{1}{V}\frac{dV}{dt} - \frac{1}{T}\frac{dT}{dt}\right) = \dot{m}' + \dot{m}''.$$

Converted, this results with the thermal state equation in the differential equation for the pressure of the control volume

$$\frac{dp}{dt} = \frac{R_s\,T}{V}\left(\dot{m}' + \dot{m}''\right) - \frac{p}{V}\frac{dV}{dt} + \frac{p}{T}\frac{dT}{dt}. \tag{2.3}$$

2.1.2   Energy balance of the working fluid

Within the control volume the temporal change of the internal energy of the gas content is given by

$$\frac{dU}{dt} = \dot{Q}_{hx} + \dot{Q}'_{cg} + \dot{Q}''_{cg} + \dot{W} + \dot{H}' + \dot{H}''. \tag{2.4}$$

The caloric state equation of a perfect gas is $U = m\,c_v\,T$. Derived, this results in

$$dU = dm\,c_v\,T + m\,c_v\,dT. \tag{2.5}$$

Inserting Eq. (2.5) in Eq. (2.4) leads to

$$\frac{dU}{dt} = c_v\,T\frac{dm}{dt} + m\,c_v\frac{dT}{dt} = \dot{Q}_{hx} + \dot{Q}'_{cg} + \dot{Q}''_{cg} + \dot{W} + \dot{H}' + \dot{H}''. \tag{2.6}$$

The compression/expansion power and the enthalpy fluxes between the control volumes are $\dot{W} = -p\,dV/dt$, $\dot{H}' = \dot{m}'\,c_p\,T'$ and $\dot{H}'' = \dot{m}''c_p\,T''$, where the gas temperatures at the borders of the control volume are denoted with T' and T''. Eq. (2.6), together with Eq. (2.1) and the thermal state equation of a perfect gas results in the differential equation for the gas temperature of the control volume

$$\frac{c_v\,p\,V}{R_s\,T}\frac{dT}{dt} = -c_v\,T\left(\dot{m}' + \dot{m}''\right) + \dot{Q}_{hx} + \dot{Q}'_{cg} + \dot{Q}''_{cg} - p\frac{dV}{dt} + \dot{m}'\,c_p\,T' + \dot{m}''c_p\,T''. \tag{2.7}$$

2.1.3   Energy balance of the solid material

The temporal change of the material's internal energy is given by

$$\frac{dU_m}{dt} = -\dot{Q}_{hx} + \dot{Q}'_{cm} + \dot{Q}''_{cm} + \dot{Q}_{ext}. \tag{2.8}$$

With the constant material density ρ_m and the constant specific material heat capacity c_m, the differential equation for the material temperature T_m can be written in the form

$$\rho_m\,V_m\,c_m\frac{dT_m}{dt} = -\dot{Q}_{hx} + \dot{Q}'_{cm} + \dot{Q}''_{cm} + \dot{Q}_{ext}, \tag{2.9}$$

where the material volume is represented by V_m.

2.1.4   Entropy balance

Within the control volume the temporal change of the entropy of the gas content is given by

$$\frac{dS}{dt} = \dot{S}_{hx} + \frac{dS_{irr}}{dt} + \dot{S}'_{cg} + \dot{S}''_{cg} + \dot{S}' + \dot{S}'', \tag{2.10}$$

where the entropy production rate due to irreversibility is denoted with dS_{irr}/dt. The terms $\dot{S}'_{cg}$ and $\dot{S}''_{cg}$ are entropy fluxes due to heat conduction. For a perfect gas, the entropy can be expressed through [57]

$$S(T, V) = m\, c_v\, ln\, \frac{T}{T^0} + m\, R_s\, ln\, \frac{V}{V^0} + S^0 \qquad (2.11)$$

or

$$S(T, p) = m\, c_p\, ln\, \frac{T}{T^0} - m\, R_s\, ln\, \frac{p}{p^0} + S^0, \qquad (2.12)$$

in which the constant S^0 is set to be $S^0(T^0, V^0) = S^0(T^0, p^0) = 0$. The temporal derivative of Eq. (2.11) is

$$\frac{dS}{dt} = \frac{dm}{dt}\left(c_v\, ln\, \frac{T}{T^0} + R_s\, ln\, \frac{V}{V^0}\right) + \frac{m\, c_v}{T}\frac{dT}{dt} + \frac{m\, R_s}{V}\frac{dV}{dt},$$

which, together with Eq. (2.1) and (2.7) as well as the thermal state equation of a perfect gas results in

$$\frac{dS}{dt} = (\dot{m}' + \dot{m}'')\left(c_v\left(ln\, \frac{T}{T^0} - 1\right) + R_s\, ln\, \frac{V}{V^0}\right) + \frac{\dot{Q}_{hx}}{T} + \frac{\dot{Q}'_{cg}}{T} + \frac{\dot{Q}''_{cg}}{T} + \dot{m}'c_p\frac{T'}{T} + \dot{m}''c_p\frac{T''}{T}. \qquad (2.13)$$

Using Eq. (2.12), the entropy fluxes between the control volumes can be expressed trough

$$\dot{S}' = \dot{m}'\, c_p\, ln\, \frac{T'}{T^0} - \dot{m}'\, R_s\, ln\, \frac{p'}{p^0} \qquad (2.14)$$

and

$$\dot{S}'' = \dot{m}''\, c_p\, ln\, \frac{T''}{T^0} - \dot{m}''\, R_s\, ln\, \frac{p''}{p^0}. \qquad (2.15)$$

Inserting Eq. (2.13) to (2.15) in Eq. (2.10) and using $\dot{S}_{hx} = \dot{Q}_{hx}/T$ for the entropy flux due to heat transfer between gas and material as well as $\dot{S}'_{cg} = \dot{Q}'_{cg}/T$ and $\dot{S}''_{cg} = \dot{Q}''_{cg}/T$ for the conductive entropy fluxes, the entropy production rate due to irreversibility results in

$$\frac{dS_{irr}}{dt} = (\dot{m}' + \dot{m}'')\left(c_v\left(ln\, \frac{T}{T^0} - 1\right) + R_s\, ln\, \frac{V}{V^0}\right)$$
$$+ \dot{m}'\left(c_p\left(\frac{T'}{T} - ln\, \frac{T'}{T^0}\right) + R_s\, ln\, \frac{p'}{p^0}\right) + \dot{m}''\left(c_p\left(\frac{T''}{T} - ln\, \frac{T''}{T^0}\right) + R_s\, ln\, \frac{p''}{p^0}\right). \qquad (2.16)$$
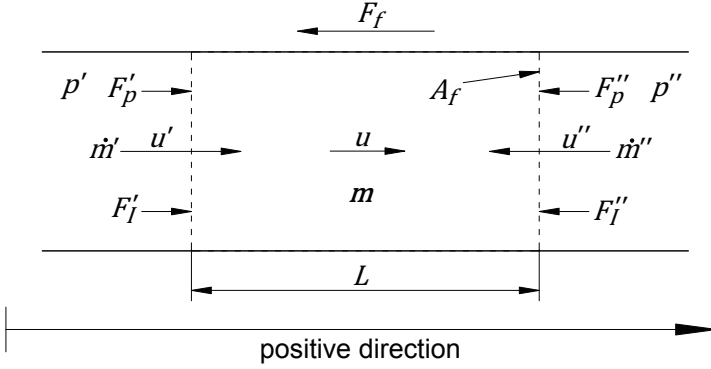
Figure 2.3: Schematic representation of the acting forces on the control volume gas mass m having the velocity u. The acting forces are pressure forces F_p' and F_p'', momentum forces F_I' and F_I'', and the flow friction force F_f, which is always opposite to the direction of motion.

2.1.5 Momentum balance

The momentum balance is applied to the gas mass m of the control volume. According to Fig. 2.3 the gas mass m is exposed to momentum forces F_I' and F_I'', pressure forces F_p' and F_p'', and the flow friction force F_f. The forces F_I' and F_p' acting on the gas mass m are in the positive direction, whereas the forces F_I'' and F_p'' act in the negative direction. The flow friction force is always opposite to the direction of motion.

The temporal change of the momentum $I = m\,u$ of the gas mass m having the velocity u is

$$\frac{dI}{dt} = \frac{d(m\,u)}{dt} = F_I' - F_I'' + F_p' - F_p'' - F_f\,. \tag{2.17}$$

With the expression

$$\dot{m} = \rho\,A_f\,u\,, \tag{2.18}$$

which relates the flux $\dot{m}$ of the gas mass m to its velocity u, the free flow area A_f and its density $\rho = m/V$ follows

$$u = \frac{\dot{m}}{\rho\,A_f} = \frac{V\,\dot{m}}{m\,A_f} = L\,\frac{\dot{m}}{m}\,, \tag{2.19}$$

where L represents the length of the control volume. Using Eq. (2.19), the momentum results in $I = m\,u = \dot{m}\,L$, and Eq. (2.17) becomes

$$\frac{dI}{dt} = L\,\frac{d\dot{m}}{dt} = F_I' - F_I'' + F_p' - F_p'' - F_f\,. \tag{2.20}$$

The momentum forces are calculated with the mass fluxes $\dot{m}'$ and $\dot{m}''$ at the control volume borders $'$ and $''$ according to $F_I' = \dot{m}'\,u'$ and $F_I'' = \dot{m}''u''$, where u' and u'' are the respective velocities of the fluid. With Eq. (2.18) and the thermal state equation of a perfect gas follows $F_I' = \dot{m}'^2\,R_s\,T'/(p'\,A_f)$ and $F_I'' = \dot{m}''^2 R_s\,T''/(p''A_f)$. The pressure forces are calculated with $F_p' = p'\,A_f$ and $F_p'' = p''A_f$.

Inserting the relations for the momentum and pressure forces in Eq. (2.20) leads,

together with $V = L\,A_f$ to

$$\frac{d\dot{m}}{dt} \;=\; \frac{R_s\,T'}{p'\,V}\,\dot{m}'^2 \;-\; \frac{R_s\,T''}{p''V}\,\dot{m}''^2 \;+\; \frac{A_f}{L}\,(p' - p'') \;-\; \frac{F_f}{L}\,. \qquad (2.21)$$

According to [58] the flow friction force can be modeled using

$$F_f \;=\; f_f\,\frac{2\,\dot{m}\,|\dot{m}|\,L}{\rho\,A_f\,d_h}\,, \qquad (2.22)$$

where d_h represents the hydraulic diameter of the structure and f_f the flow friction factor.

With $A_f/L = A_f^2/V$ and the thermal state equation of a perfect gas the temporal change of the mass flux $\dot{m}$ becomes

$$\frac{d\dot{m}}{dt} \;=\; \frac{R_s}{V}\left(\frac{\dot{m}'^2\,T'}{p'} - \frac{\dot{m}''^2\,T''}{p''}\right) \;+\; \frac{A_f^2}{V}\,(p' - p'') \;-\; \frac{2\,f_f\,R_s\,T\,\dot{m}\,|\dot{m}|}{p\,A_f\,d_h}\,. \qquad (2.23)$$

The use of absolute value for the mass flux ensures that the direction of the flow friction force is always opposite to the direction of motion.

The derived system of non-linear coupled ordinary differential equations (2.3), (2.7), (2.9), (2.16) and (2.23) represents the basis of the theoretical analysis of the pulse tube engine in the following sections of this chapter. The equations will be applied to the control volumes of the cylinder, the heat exchangers, the pulse tube and the regenerator. The differential equations of each control volume are coupled to the differential equations of its neighboring control volumes through the mass fluxes m' and m'', the enthalpy fluxes H' and H'', the entropy fluxes S' and S'', the conductive fluxes of the gas and the material Q'_{cg}, Q''_{cg}, S'_{cg}, S''_{cg}, Q'_{cm} and Q''_{cm} as well as the neighboring pressures p' and p''.

2.2   Parameter definitions

A generalized characterization of the pulse tube engine process requires the definition of dimensionless operating and design parameters.

The operating parameters are the **temperature ratio** τ, defined as the ratio between the hot temperature T_h and the cold temperature T_c

$$\tau \;:=\; \frac{T_h}{T_c} \qquad (2.24)$$

as well as the **pressure ratio** Π, representing the ratio between maximum pressure

p_{max} and minimum pressure p_{min}

$$\Pi := \frac{p_{max}}{p_{min}} \,. \tag{2.25}$$

Design parameters are the **distribution ratio** r_d, calculated as the ratio between the regenerator gas volume V_{reg} and the pulse tube gas volume V_{pt}

$$r_d := \frac{V_{reg}}{V_{pt}} \tag{2.26}$$

as well as the **compression ratio** r_c, representing the ratio between the maximum engine gas volume V_{max} and the minimum engine gas volume V_{min} minus one

$$r_c := \frac{V_{max}}{V_{min}} - 1 = \frac{V_{pt} + V_{reg} + V_{hx} + V_d}{V_{pt} + V_{reg} + V_{hx}} - 1 = \frac{V_d}{V_{pt} + V_{reg} + V_{hx}} \,. \tag{2.27}$$

The displacement volume of the cylinder and the sum of the heat exchanger gas volumes are denoted with V_d and V_{hx}, respectively.

For the description of a working pulse tube engine it may be reasonable to add the volume V_{chx_1} of chx$_1$ to the pulse tube volume and the volumes V_{hhx} and V_{chx_2} of hhx and chx$_2$ to the regenerator volume. For the purpose of these definitions additional dead volumes of the engine remain disregarded.

The four introduced parameters are used for all further investigations of the engine.

2.3   Analytical model of the pulse tube engine

In order to discover fundamental characteristics of the pulse tube engine and to derive mathematical relations for its power output and efficiency, an ideal analytical model describing the engine process is derived. Analytical approaches to describe the pulse tube refrigerator are given, for instance in [59, 60]. A similar work for the pulse tube engine has not been done.

The pulse tube engine is typically operating at low frequencies of only a few Hz. Such slow thermodynamic processes can be approached using an isothermal model [55, 61, 62, 63]. An isothermal analysis ($dT/dt = 0$) of the cycle decouples the system of differential equations (2.3), (2.7), (2.9) and (2.16), and enables an analytical integration of the decoupled differential equations.

In the analytical model heat conduction is not considered. The pressure is regarded as uniform throughout all engine components. Thus, the temporal change of the mass fluxes may be disregarded.

2.3.1 Isothermal approach

This subsection explains the basics of the applied isothermal model.

As already shown in Fig. 1.2 the cylinder has the uniform material temperature $T_{m,cyl} = T_c$, the two cold heat exchangers have the uniform material temperatures $T_{m,chx_1} = T_{m,chx_2} = T_c$ and the hot heat exchanger has the uniform material temperature $T_{m,hhx} = T_h$. Pulse tube and regenerator show the space-dependent linear material temperature distributions

$$T_{m,pt}(x_{pt}) = T_c + \frac{x_{pt}}{L_{pt}}(T_h - T_c) \qquad (2.28)$$

and

$$T_{m,reg}(x_{reg}) = T_h - \frac{x_{reg}}{L_{reg}}(T_h - T_c), \qquad (2.29)$$

with x_{pt} denoting the pulse tube position starting at its cold side with $x_{pt} = 0$ and x_{reg} denoting the regenerator position starting at its hot side with $x_{reg} = 0$. The length of the pulse tube is L_{pt} and of the regenerator L_{reg}. For the following considerations these temperature distributions are regarded as being constant over time. Thus, Eq. (2.9) does not have to be solved.

Furthermore, all engine components consist of one control volume each, whereas the gas volumes of the heat exchangers are neglected (see Fig. 2.1 (a) for the zero-dimensional approach). Thus, the cold heat exchanger chx_2 does not need to be considered in this analysis. For pulse tube and regenerator the (spatial) mean material temperatures are given through

$$< T_{m,pt} > = < T_{m,reg} > = \frac{1}{2}(T_h + T_c) = \frac{T_c}{2}(\tau + 1). \qquad (2.30)$$

In the isothermal analysis of the pulse tube engine the gas in the cylinder, the heat exchangers and the regenerator is always in thermal equilibrium with the material [57]. The constant gas temperatures in these components are $T_{cyl} = T_{g,cyl} = T_c$, $T_{chx} = T_{g,chx_1} = T_c$, $T_{hhx} = T_{g,hhx} = T_h$ and $T_{reg} = T_{g,reg} = < T_{m,reg} > = T_c(\tau + 1)/2$.

Due to cold gas being pushed into the cold side of the pulse tube during the compression stroke, the pulse tube's mean gas temperature is below its material temperature while the compression takes place. During the expansion stroke hot gas is pushed into the hot side of the pulse tube. Thus its mean gas temperature is above the material temperature while the expansion takes place. The situation is illustrated in Fig. 2.4 (a). For compression and expansion, it is assumed that the gas in the pulse tube has a constant temperature slightly below the mean material temperature (compression stroke) and slightly above the mean material temperature (expansion stroke).

(a) Temperature of the pulse tube

(b) Corresponding ideal pV- diagram
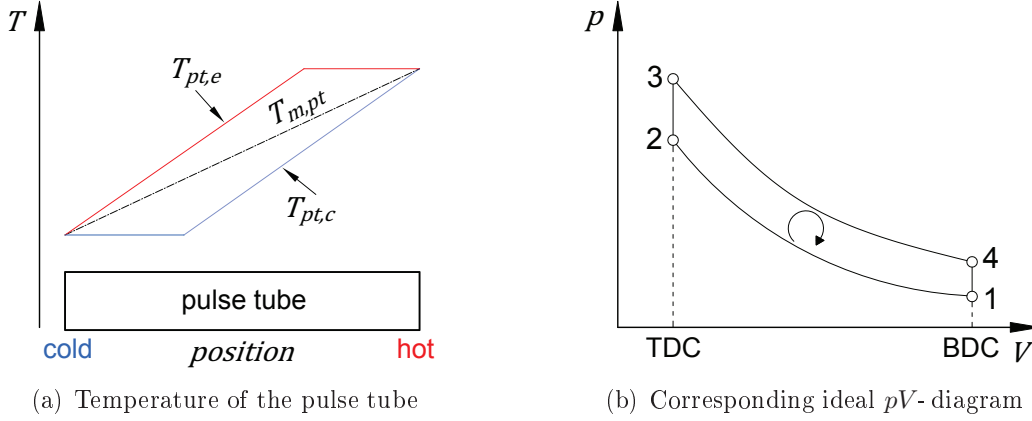
Figure 2.4: (a) Gas and material temperature of the pulse tube during compression and expansion. In the isothermal model the compression gas temperature in the pulse tube $T_{pt,c}$ is assumed to be constant and slightly below the material temperature $T_{m,pt}$, whereas the expansion gas temperature $T_{pt,e}$ is assumed to be constant and slightly above the material temperature; (b) Corresponding idealized pV- diagram, TDC: piston's top dead center, BDC: piston's bottom dead center.

Using this assumption, the pulse tube's gas temperature is set to

$$T_{pt,c} = (1 - \epsilon_c) <T_{m,pt}> = (1 - \epsilon_c) \frac{T_c}{2} (\tau + 1) \qquad (2.31)$$

during the compression stroke, and

$$T_{pt,e} = (1 + \epsilon_e) <T_{m,pt}> = (1 + \epsilon_e) \frac{T_c}{2} (\tau + 1) \qquad (2.32)$$

during the expansion stroke. The parameters ϵ_c and ϵ_e are in the range of $0 < \epsilon_c < 1$ and $0 < \epsilon_e < 1$, respectively.

At TDC the pulse tube's gas temperature undergoes a thermal relaxation [24] from $T_{pt,c}$ to $T_{pt,e}$ and at BDC a thermal relaxation from $T_{pt,e}$ to $T_{pt,c}$. Both relaxation processes occur due to shifting and mixing of the gas in the pulse accompanied by entropy production [64]. Since the relaxations take place at TDC and BDC, the gas volume of the entire engine is constant and the differential equations can be solved analytically [65].

Summarizing, the thermodynamic cycle is split into four phases. According to Fig. 2.4 (b) an isothermal compression at $T_{pt,c}$ occurs between state 1 and state 2. A high pressure thermal relaxation from $T_{pt,c}$ to $T_{pt,e}$ takes place between state 2 and state 3 at constant minimum engine gas volume. An isothermal expansion at $T_{pt,e}$ occurs between state 3 and state 4 and a low pressure thermal relaxation from $T_{pt,e}$ to $T_{pt,c}$ takes place between state 4 and state 1 at constant maximum engine gas volume.

2.3.2   Boundary conditions

Between the engine components, boundary conditions for all transferred quantities need to be assigned.

The gas flowing between the components carries thermal energy and entropy. Both are related to the mass flux and the gas temperature. In Fig. 2.5 the temperatures of the gas crossing the control volume borders are designated. Gas leaving and entering
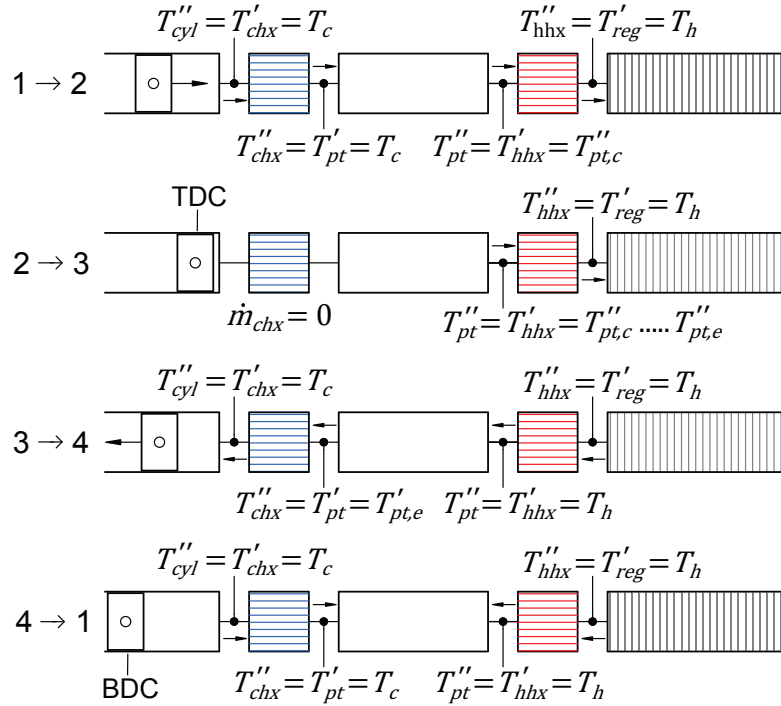
Figure 2.5: Boundary gas temperatures of the engine components during the four phases of the cycle. T''_{cyl}: cylinder, T'_{chx}, T''_{chx}: cold heat exchanger, T'_{pt}, T''_{pt}: pulse tube, T'_{hhx}, T''_{hhx}: hot heat exchanger, T'_{reg}: regenerator. The arrows between the components symbolize the direction of the respective mass fluxes. The mass flux via the cold heat exchanger $\dot{m}_{chx}$ is zero during the high pressure thermal relaxation. The regenerator is closed at its right side.

the cylinder at its right side, respectively leaving and entering the cold heat exchanger at its left side has the temperature $T''_{cyl} = T'_{chx} = T_c$. Gas leaving and entering the hot heat exchanger at its right side, respectively leaving and entering the regenerator at its left side has the temperature $T''_{hhx} = T'_{reg} = T_h$. Gas leaving the cold heat exchanger at its right side, respectively entering the pulse tube at its left side has the temperature $T''_{chx} = T'_{pt} = T_c$. Gas leaving the hot heat exchanger at its left side, respectively entering the pulse tube at its right side has the temperature $T''_{pt} = T'_{hhx} = T_h$. During the compression stroke ($1 \rightarrow 2$) gas is leaving the pulse tube at its right side and entering the hot heat exchanger at its left side with the temperature $T''_{pt} = T'_{hhx} = T''_{pt,c}$,

whereas during the high pressure relaxation $(2 \to 3)$ gas is leaving the pulse tube at its right side and entering the hot heat exchanger at its left side with the temperature $T''_{pt} = T'_{hhx} = T''_{pt,c}...T''_{pt,e}$. During the expansion stroke $(3 \to 4)$ gas is leaving the pulse tube at its left side and entering the cold heat exchanger at its right side with the temperature $T'_{pt} = T''_{chx} = T'_{pt,e}$. During the low pressure relaxation $(4 \to 1)$ gas is entering the pulse tube at both sides.

Since all components except the pulse tube are isothermal throughout the entire cycle, the denotations $'$ and $''$ are only necessary to identify the boundary values at the pulse tube's cold $'$ and hot $''$ side. The respective pulse tube boundary temperatures T' and T'' are assumed to be

$$T' = \lambda' < T_{m,pt} > + (1 - \lambda') T_c \qquad (2.33)$$

at its cold, and

$$T'' = \lambda'' < T_{m,pt} > + (1 - \lambda'') T_h \qquad (2.34)$$

at its hot side.

During the compression stroke, the pulse tube's hot side exit temperature is $T''_{pt,c} = (1 - \epsilon_c) T''$ and during the expansion stroke the pulse tube's cold side exit temperature is $T'_{pt,e} = (1 + \epsilon_e) T'$. The hot side exit temperature during the high pressure thermal relaxation is $T''_{pt,c}...T''_{pt,e} = (1 - \epsilon_c) T''...(1 + \epsilon_e) T''$.

Gas is entering the pulse tube's cold side with the temperature T_c during the compression stroke and the pulse tube's hot side with the temperature T_h during the expansion stroke. Hence, the parameters λ' and λ'' can be deduced from the conditions $T'_{pt,c} = T_c$ and $T''_{pt,e} = T_h$ to

$$\lambda' = \frac{2 \, \epsilon_c}{(1 - \epsilon_c) \, (\tau - 1)} \qquad (2.35)$$

and

$$\lambda'' = \frac{2 \, \tau \, \epsilon_e}{(1 + \epsilon_e) \, (\tau - 1)} \, . \qquad (2.36)$$

It follows

$$T'_{pt,e} = \frac{1 + \epsilon_e}{1 - \epsilon_c} \, T_c \quad \text{and} \quad T''_{pt,c} = \frac{1 - \epsilon_c}{1 + \epsilon_e} \, T_c \, \tau \, . \qquad (2.37)$$

2.3.3   Calculation of the time-dependent pressure

The result of the mass balance, obtained with Eq. (2.3) is used to calculate the pressure throughout the thermodynamic cycle of the pulse tube engine.

For all considerations the mass fluxes via the cold and hot heat exchanger are denoted with $\dot{m}_{chx}$ and $\dot{m}_{hhx}$. The nonconsideration of the heat exchanger gas volumes

leads to $\dot{m}'_{chx} + \dot{m}''_{chx} = 0$ and $\dot{m}'_{hhx} + \dot{m}''_{hhx} = 0$, and thus $\dot{m}'_{chx} = -\dot{m}''_{chx} = \dot{m}_{chx}$ and $\dot{m}'_{hhx} = -\dot{m}''_{hhx} = \dot{m}_{hhx}$, respectively. Left side mass fluxes $\dot{m}'_{chx}$ and $\dot{m}'_{hhx}$ are positive, and right side mass fluxes $\dot{m}''_{chx}$ and $\dot{m}''_{hhx}$ are negative.

With the definitions (2.26) and (2.27), Eq. (2.3) becomes

$$\frac{dp}{dt} = -\frac{R_s\,T_c}{V_{cyl}}\,\dot{m}_{chx} - \frac{p}{V_{cyl}}\frac{dV_{cyl}}{dt} \tag{2.38}$$

for the cylinder,

$$\frac{dp}{dt} = \frac{R_s\,T_{pt}}{V_d}\,r_c\,(r_d + 1)\,(\dot{m}_{chx} - \dot{m}_{hhx}) \tag{2.39}$$

for the pulse tube during the isothermal compression and the isothermal expansion,

$$\frac{dp}{dt} = \frac{R_s\,T_{pt}}{V_d}\,r_c\,(r_d + 1)\,(\dot{m}_{chx} - \dot{m}_{hhx}) + \frac{p}{T_{pt}}\frac{dT_{pt}}{dt} \tag{2.40}$$

for the pulse tube during the thermal relaxations, and

$$\frac{dp}{dt} = \frac{R_s\,T_{reg}}{V_d}\frac{r_c\,(r_d + 1)}{r_d}\,\dot{m}_{hhx} \tag{2.41}$$

for the regenerator.

The cylinder gas volume at BDC is $V_{cyl} = V_d$ and at TDC $V_{cyl} = 0$. The resulting mass fluxes can be calculated from Eq. (2.38) or (2.39) and Eq. (2.41). The mass flux via the cold heat exchanger is during the isothermal <u>c</u>ompression and the isothermal <u>e</u>xpansion

$$\dot{m}_{chx,c/e} = \frac{V_d}{R_s\,r_c\,(r_d + 1)}\left(\frac{r_d}{T_{reg}} + \frac{1}{T_{pt}}\right)\frac{dp}{dt}\,, \tag{2.42}$$

during the <u>h</u>igh <u>p</u>ressure thermal relaxation

$$\dot{m}_{chx,hp} = 0\,, \tag{2.43}$$

and during the <u>l</u>ow <u>p</u>ressure thermal relaxation

$$\dot{m}_{chx,lp} = -\frac{V_d}{R_s\,T_c}\frac{dp}{dt}\,. \tag{2.44}$$

Throughout all phases the mass flux via the hot heat exchanger is given by

$$\dot{m}_{hhx} = \frac{V_d}{R_s\,r_c\,(r_d + 1)}\frac{r_d}{T_{reg}}\frac{dp}{dt}\,. \tag{2.45}$$

The pressure during the four engine phases is calculated as follows:

Isothermal compression from state 1 to state 2

Inserting Eq. (2.42) in Eq. (2.38) delivers

$$\frac{1}{p}\frac{dp}{dt} = -\frac{1}{V_{cyl} + C_c}\frac{dV_{cyl}}{dt}, \tag{2.46}$$

with the abbreviation

$$C_c := \frac{V_d}{r_c\,(r_d + 1)}\left(r_d\,\frac{T_c}{T_{reg}} + \frac{T_c}{T_{pt,c}}\right). \tag{2.47}$$

Integrating Eq. (2.46) with the initial conditions $V_{cyl}(t_1) = V_1 = V_d$ and $p(t_1) = p_1 = p_{min}$ leads to the pressure during the compression stroke

$$p_c(t) = p_1\,\frac{V_d + C_c}{V_{cyl}(t) + C_c}, \tag{2.48}$$

which reaches in state 2

$$p_2 = p_1\,\frac{V_d + C_c}{C_c}. \tag{2.49}$$

Thermal relaxation from state 2 to state 3

Inserting Eq. (2.43) and (2.45) in Eq. (2.40) together with the abbreviation

$$C_{hp} = \frac{r_d}{T_{reg}} \tag{2.50}$$

results in

$$\frac{1}{p}\frac{dp}{dt} = -\frac{1}{T_{pt} + C_{hp}\,T_{pt}^2}\frac{dT_{pt}}{dt}. \tag{2.51}$$

Integrating Eq. (2.51) from state 2 to state 3 leads to the pressure

$$p_3 = p_2\,\frac{(C_{hp}\,T_{pt,c} + 1)\,T_{pt,e}}{(C_{hp}\,T_{pt,e} + 1)\,T_{pt,c}}. \tag{2.52}$$

Isothermal expansion from state 3 to state 4

Inserting Eq. (2.42) in Eq. (2.38) delivers

$$\frac{1}{p}\frac{dp}{dt} = -\frac{1}{V_{cyl} + C_e}\frac{dV_{cyl}}{dt}, \tag{2.53}$$

with the abbreviation

$$C_e := \frac{V_d}{r_c \, (r_d + 1)} \left(r_d \frac{T_c}{T_{reg}} + \frac{T_c}{T_{pt,e}} \right) . \tag{2.54}$$

Integrating Eq. (2.53) with the initial conditions $V_{cyl}(t_3) = V_3 = 0$ and $p(t_3) = p_3 = p_{max}$ leads to the pressure during the expansion stroke

$$p_e(t) = p_3 \frac{C_e}{V_{cyl}(t) + C_e} , \tag{2.55}$$

which reaches in state 4

$$p_4 = p_3 \frac{C_e}{V_d + C_e} . \tag{2.56}$$

Thermal relaxation from state 4 to state 1

Inserting Eq. (2.44) and (2.45) in Eq. (2.40) together with the abbreviation

$$C_{lp} = \frac{r_c \, (r_d + 1)}{T_c} + \frac{r_d}{T_{reg}} \tag{2.57}$$

results in

$$\frac{1}{p} \frac{dp}{dt} = -\frac{1}{T_{pt} + C_{lp} \, T_{pt}^2} \frac{dT_{pt}}{dt} . \tag{2.58}$$

Integrating Eq. (2.58) from state 4 to state 1 leads to the pressure

$$p_1^* = p_4 \frac{(C_{lp} \, T_{pt,e} + 1) \, T_{pt,c}}{(C_{lp} \, T_{pt,c} + 1) \, T_{pt,e}} . \tag{2.59}$$

Closing the cycle through the combination of Eq. (2.59), (2.56), (2.52) and (2.49) demands

$$\frac{p_1^*}{p_1} = \frac{V_d + C_c}{C_c} \frac{(C_{hp} \, T_{pt,c} + 1) \, T_{pt,e}}{(C_{hp} \, T_{pt,e} + 1) \, T_{pt,c}} \frac{C_e}{V_d + C_e} \frac{(C_{lp} \, T_{pt,e} + 1) \, T_{pt,c}}{(C_{lp} \, T_{pt,c} + 1) \, T_{pt,e}} \overset{!}{=} 1 , \tag{2.60}$$

which is fulfilled for all values of ϵ_c and ϵ_e. Without loss of generality the ratio between ϵ_c and ϵ_e is defined as

$$\tau_0 := \frac{\epsilon_c}{\epsilon_e} . \tag{2.61}$$

With $\epsilon := \epsilon_e$ results $\epsilon_c = \tau_0 \epsilon$. The value of ϵ can be obtained from the mean gas temperature in the pulse tube during compression

$$T_{pt,c} = \frac{1}{2} \left(T'_{pt,c} + T''_{pt,c} \right) \tag{2.62}$$

or during expansion

$$T_{pt,e} = \frac{1}{2} \left(T'_{pt,e} + T''_{pt,e} \right) , \tag{2.63}$$

respectively. Eq. (2.62) and (2.63) lead to the same result for

$$\epsilon = \frac{\tau/\tau_0 - 1}{\tau + 1} . \tag{2.64}$$

Summarizing, the main results of this subsection are the pressures throughout the cycle obtained in Eq. (2.48), (2.52) and (2.55) as well as the temperature ratio τ_0 introduced in Eq. (2.61).

2.3.4   Calculation of pV- work, transferred heat and efficiency

In this subsection the pV- work obtained from the pulse tube engine and the amounts of heat transferred per cycle in the engine components are calculated. The results are used to determine the thermal efficiency of the ideal engine cycle.

The pV- **work** W_{pV} is calculated through integration of the isothermal compression power $\dot{W}_c$ and the isothermal expansion power $\dot{W}_e$ according to

$$W_{pV} = \int_1^2 \dot{W}_c \, dt + \int_3^4 \dot{W}_e \, dt = - \int_{V_d}^0 p_c \, dV_{cyl} - \int_0^{V_d} p_e \, dV_{cyl} . \tag{2.65}$$

Eq. (2.65) results with Eq. (2.48) and (2.55) in

$$W_{pV} = p_{min} \left(V_d + C_c \right) ln \left(\frac{V_d}{C_c} + 1 \right) - p_{max} \, C_e \, ln \left(\frac{V_d}{C_e} + 1 \right) , \tag{2.66}$$

and can be expressed trough series expansion around $\epsilon = 0$ as

$$W_{pV} = \sum_{i=0}^{\infty} a_i \, \epsilon^i \overset{a_0=0}{=} \sum_{i=1}^{\infty} a_i \, \epsilon^i . \tag{2.67}$$

In Appendix **T** is shown that the coefficient a_0 is equal to zero. The physical meaning of Eq. (2.67) is that the engine provides a work output or work has to be delivered to the engine, only if $\epsilon \neq 0$. Thus τ_0 in Eq. (2.64) is a temperature ratio above which the engine provides a work output or below which work has to be delivered to the engine. After inserting of Eq. (2.64) in Eq. (2.66), the pV- work can be expressed through series expansion around $\tau - \tau_0 = 0$ as

$$W_{pV} = \sum_{i=1}^{\infty} b_{W_{pV},i} \left(\tau - \tau_0 \right)^i . \tag{2.68}$$

The heat fluxes $\dot{Q}_{cyl}$, $\dot{Q}_{pt}$ and $\dot{Q}_{reg}$ to the gas in the respective components are calculated using Eq. (2.7), which becomes for the cylinder

$$0 = c_v T_c \dot{m}_{chx} + \dot{Q}_{cyl} - p \frac{dV_{cyl}}{dt} - \dot{m}_{chx} c_p T_c, \qquad (2.69)$$

for the pulse tube during compression and expansion

$$0 = c_v T_{pt} (\dot{m}_{hhx} - \dot{m}_{chx}) + \dot{Q}_{pt} + \dot{m}_{chx} c_p T'' - \dot{m}_{hhx} c_p T', \qquad (2.70)$$

for the pulse tube during the thermal relaxations with the definitions (2.26) and (2.27)

$$\frac{c_v \, p \, V_d}{R_s \, r_c \, (r_d + 1)} \frac{dT_{pt}}{dt} = c_v T (\dot{m}_{hhx} - \dot{m}_{chx}) + \dot{Q}_{pt} + \dot{m}_{chx} c_p T'' - \dot{m}_{hhx} c_p T', \quad (2.71)$$

and for the regenerator

$$0 = - c_v T_{reg} \dot{m}_{hhx} + \dot{Q}_{reg} + \dot{m}_{hhx} c_p T_h. \qquad (2.72)$$

Using Eq. (2.7) the heat fluxes in the heat exchangers are calculated for the cold heat exchanger with

$$\dot{Q}_{chx} = \dot{m}_{chx} c_p (T'' - T_c), \qquad (2.73)$$

and for the hot heat exchanger with

$$\dot{Q}_{hhx} = \dot{m}_{hhx} c_p (T_h - T'), \qquad (2.74)$$

respectively.

Solving Eq. (2.69) to (2.74) for the four phases and integrating the heat fluxes over the entire engine cycle leads to the heat transferred to the working gas or removed from the working gas per cycle. Using series expansion for the transferred heat around $\epsilon = 0$ shows that the coefficient of the constant components $(a_0 \, \epsilon^0)$ disappears for the transferred heat. Moreover, for the transferred heat in the pulse tube, the coefficient of the linear component $(a_1 \, \epsilon^1)$ disappears as well. For details see Appendix **T**.

Using Eq. (2.64), the transferred heat can be expressed through series expansion around $\tau - \tau_0 = 0$ as

$$Q_{cyl} = \oint \dot{Q}_{cyl} \, dt = \sum_{i=1}^{\infty} b_{Q_{cyl},i} \, (\tau - \tau_0)^i \qquad (2.75)$$

for the **cylinder**, as

$$Q_{chx} = \oint \dot{Q}_{chx}\, dt = \sum_{i=1}^{\infty} b_{Q_{chx},i} \left(\tau - \tau_0\right)^i \tag{2.76}$$

for the **cold heat exchanger**, as

$$Q_{pt} = \oint \dot{Q}_{pt}\, dt = \sum_{i=2}^{\infty} b_{Q_{pt},i} \left(\tau - \tau_0\right)^i \tag{2.77}$$

for the **pulse tube**, and as

$$Q_{hhx} = \oint \dot{Q}_{hhx}\, dt = \sum_{i=1}^{\infty} b_{Q_{hhx},i} \left(\tau - \tau_0\right)^i \tag{2.78}$$

for the **hot heat exchanger**. The transferred heat is always zero at $\tau = \tau_0$ (see Appendix **T**).

The first derivative of Eq. (2.77) in τ is

$$\frac{dQ_{pt}}{d\tau} = \sum_{i=2}^{\infty} i\, b_{Q_{pt},i} \left(\tau - \tau_0\right)^{i-1} = \sum_{j=1}^{\infty} \left(j+1\right) b_{Q_{pt},i} \left(\tau - \tau_0\right)^j . \tag{2.79}$$

For $\tau = \tau_0$ Eq. (2.79) becomes zero (see Appendix **T**). Thus, the transferred heat in the pulse tube has a local minimum or maximum at $\tau = \tau_0$. This information can be used to calculate τ_0. The first derivative of Q_{pt} in τ at $\tau = \tau_0$ is

$$\left.\frac{dQ_{pt}}{d\tau}\right|_{\tau=\tau_0} = -\frac{\kappa\, p_{min}\, V_d \left(r_d \left(\tau_0 - 1\right) - 1\right)}{\left(\kappa - 1\right)\left(r_d + 1\right)\tau_0} \stackrel{!}{=} 0 . \tag{2.80}$$

For the minimal temperature ratio above which the engine is providing a work output results

$$\tau_0 = \frac{r_d + 1}{r_d} . \tag{2.81}$$

The second derivative of Q_{pt} in τ at $\tau = \tau_0$ is

$$\left.\frac{d^2Q_{pt}}{d\tau^2}\right|_{\tau=\tau_0} = \frac{\kappa\, p_{min}\, V_d\, r_d^2}{r_c \left(\kappa - 1\right)} \frac{4\, r_d^2 \left(r_c - 1\right) + 2\, r_c\, r_d \left(r_c + 2\right) + r_c^2}{\left(r_d + 1\right)^2 \left(r_d \left(2\, r_d + 3\right) + 1\right)\left(2\, r_d \left(r_c + 1\right) + r_c\right)} . \tag{2.82}$$

The sign of Eq. (2.82) is governed by

$$\sigma = 4\, r_d^2 \left(r_c - 1\right) + 2\, r_c\, r_d \left(r_c + 2\right) + r_c^2 .$$

If $r_c < 1$ and

$$r_c < 2\,r_d\,\frac{\sqrt{r_d^2 + 4\,r_d + 2} - (r_d + 1)}{2\,r_d + 1}\,,$$

σ is smaller than zero and thus $d^2 Q_{pt}/d\tau^2|_{\tau=\tau_0} < 0$. In this case, at $\tau = \tau_0$ a local maximum of Q_{pt} is located and integrated over one cycle heat is removed from the working gas in the pulse tube.

If $r_c < 1$ and

$$r_c = 2\,r_d\,\frac{\sqrt{r_d^2 + 4\,r_d + 2} - (r_d + 1)}{2\,r_d + 1}\,,$$

σ is equal to zero and thus $d^2 Q_{pt}/d\tau^2|_{\tau=\tau_0} = 0$. In this case, integrated over the cycle, no heat is exchanged between the working gas and the pulse tube material. In all other cases, integrated over the cycle, heat is added to the working gas in the pulse tube. This situation allows for an addition of heat to the working gas at temperatures lower than T_h, enabling the engine to convert heat energy from sources with decreasing temperature. Only this case is of practical interest.

Finally, the amount of heat transferred per cycle in the **regenerator** is

$$Q_{reg} = \oint \dot{Q}_{reg}\,dt = 0\,. \tag{2.83}$$

The thermal efficiency is calculated with

$$\eta_{th} = \frac{|W_{pV}|}{Q_{in}}\,, \tag{2.84}$$

where Q_{in} represents the heat input. According to Eq. (2.75) to (2.78) and Eq. (2.83) heat is added to the gas in the cylinder at the temperature T_c, in the hot heat exchanger at the temperature T_h, and for $\sigma > 0$ in the pulse tube at temperatures between T_c and T_h. The heat added to the gas in the cylinder, in general, is provided from the surroundings and does not have to be provided by the heat source.

Taking into account only the heat delivered by the hot heat exchanger at the temperature T_h, the thermal efficiency of the pulse tube engine is calculated with

$$\eta_{\overline{th}}^{=} = \frac{|W_{pV}|}{Q_{hhx}}\,. \tag{2.85}$$

Series expansion around $\tau - \tau_0 = 0$ delivers

$$\eta_{\overline{th}}^{=} = \sum_{i=0}^{\infty} b_{\eta_{\overline{th}}^{=},i}\,(\tau - \tau_0)^i\,. \tag{2.86}$$

Considering in the case of $\sigma > 0$ also the heat delivered by the pulse tube at

temperatures between T_c and T_h, the thermal efficiency of the pulse tube engine is calculated with

$$\eta_{th}^{<} = \frac{|W_{pV}|}{Q_{hhx} + Q_{pt}} . \tag{2.87}$$

The usage of series expansion around $\tau - \tau_0 = 0$ leads to

$$\eta_{th}^{<} = \sum_{i=0}^{\infty} b_{\eta_{th}^{<},i} \left(\tau - \tau_0\right)^i . \tag{2.88}$$

In both cases the thermal efficiency has a finite value at $\tau = \tau_0$ of

$$\left.\eta_{th}^{=}\right|_{\tau=\tau_0} = \left.\eta_{th}^{<}\right|_{\tau=\tau_0} = \frac{\kappa - 1}{\kappa\left(r_d + 1\right)} . \tag{2.89}$$

This is only possible if $\tau_0 > 1$.

Together with the pV-work, obtained in Eq. (2.66) or respectively Eq. (2.68), and the amounts of heat transferred per cycle in the components, obtained in Eq. (2.75) to (2.78) and Eq. (2.83), the main results of this subsection are the quantification of the temperature ratio τ_0, above which the engine provides a work output, with Eq. (2.81), and the fact that the pulse tube engine enables an addition of heat along the pulse tube.

2.3.5   Calculation of the entropy production

To get an understanding of power and efficiency limitations of the pulse tube engine, the entropy production rate is calculated using Eq. (2.16).

For the **cylinder** follows

$$
\begin{aligned}
\frac{dS_{irr,cyl}}{dt} &= -\dot{m}_{chx}\left(c_v\left(ln\frac{T_c}{T^0} - 1\right) + R_s\,ln\frac{V_{cyl}}{V^0}\right) - \dot{m}_{chx}\left(c_p\left(1 - ln\frac{T_c}{T^0}\right) + R_s\,ln\frac{p}{p^0}\right) \\
&= \dot{m}_{chx}\,R_s\left(ln\frac{T_c}{T^0} - ln\frac{V_{cyl}}{V^0} - ln\frac{p}{p^0} - 1\right),
\end{aligned}
$$

which together with the thermal state equation of a perfect gas results in

$$\frac{dS_{irr,cyl}}{dt} = \dot{m}_{chx}\,R_s\left(ln\left(\frac{T_c}{p\,V_{cyl}}\frac{p^0\,V^0}{T^0}\right) - 1\right) = -\dot{m}_{chx}\,R_s\left(ln\frac{m_{cyl}}{m^0} + 1\right), \tag{2.90}$$

where m_{cyl} represents the gas mass content of the cylinder and m^0 a constant. Cycle

integration of Eq. (2.90) delivers with $\dot{m}_{chx} = - dm_{cyl}/dt$ and

$$\oint dm = 0 \qquad (2.91)$$

$$S_{irr,cyl} = \oint dS_{irr,cyl} = R_s \oint \left(ln\, \frac{m_{cyl}}{m^0} + 1 \right) dm_{cyl} = 0 \,. \qquad (2.92)$$

The entropy production rate in the **cold heat exchanger** is

$$
\begin{aligned}
\frac{dS_{irr,chx}}{dt} &= \dot{m}_{chx}\, c_p \left(1 - ln\, \frac{T_c}{T^0} \right) - \dot{m}_{chx}\, c_p \left(\frac{T''_{chx}}{T_c} - ln\, \frac{T''_{chx}}{T^0} \right) \qquad (2.93) \\
&= \dot{m}_{chx}\, c_p \left(1 - \frac{T''_{chx}}{T_c} + ln\, \frac{T''_{chx}}{T_c} \right) .
\end{aligned}
$$

Cycle integration delivers with Eq. (2.37), (2.54), (2.56) and (2.61)

$$S_{irr,chx} = \frac{c_p\, p_{max}}{R_s\, T_c} \frac{V_d\, C_e}{V_d + C_e} \left(\frac{(\tau_0 + 1)\,\epsilon}{1 - \tau_0\,\epsilon} - ln\, \frac{1 + \epsilon}{1 - \tau_0\,\epsilon} \right) . \qquad (2.94)$$

Using Eq. (2.64) the entropy production in the cold heat exchanger can be expressed through series expansion around $\tau - \tau_0 = 0$ as

$$S_{irr,chx} = \sum_{i=2}^{\infty} b_{S_{chx},i}\, (\tau - \tau_0)^i \,. \qquad (2.95)$$

The entropy production rate in the **pulse tube** is given trough

$$
\begin{aligned}
\frac{dS_{irr,pt}}{dt} &= (\dot{m}_{chx} - \dot{m}_{hhx}) \left(c_v \left(ln\, \frac{T_{pt}}{T^0} - 1 \right) + R_s\, ln\, \frac{V_{pt}}{V^0} \right) \\
&+ \dot{m}_{chx} \left(c_p \left(\frac{T'_{pt}}{T_{pt}} - ln\, \frac{T'_{pt}}{T^0} \right) + R_s\, ln\, \frac{p}{p^0} \right) - \dot{m}_{hhx} \left(c_p \left(\frac{T''_{pt}}{T_{pt}} - ln\, \frac{T''_{pt}}{T^0} \right) + R_s\, ln\, \frac{p}{p^0} \right) \\
&= (\dot{m}_{chx} - \dot{m}_{hhx}) \left(c_v \left(ln\, \frac{T_{pt}}{T^0} - 1 \right) + R_s \left(ln\, \frac{V_{pt}}{V^0} + ln\, \frac{p}{p^0} \right) \right) \\
&+ \dot{m}_{chx}\, c_p \left(\frac{T'_{pt}}{T_{pt}} - ln\, \frac{T'_{pt}}{T^0} \right) - \dot{m}_{hhx}\, c_p \left(\frac{T''_{pt}}{T_{pt}} - ln\, \frac{T''_{pt}}{T^0} \right) . \qquad (2.96)
\end{aligned}
$$

Eq. (2.96) becomes with $\dot{m}_{chx} - \dot{m}_{hhx} = dm_{pt}/dt$, the thermal state equation of a perfect gas and $R_s = c_p - c_v$

$$
\begin{aligned}
\frac{dS_{irr,pt}}{dt} &= (\dot{m}_{chx} - \dot{m}_{hhx})\, c_p\, ln\, \frac{T_{pt}}{T^0} + \frac{dm_{pt}}{dt} \left(R_s\, ln\, \frac{m_{pt}}{m^0} - c_v \right) \\
&+ \dot{m}_{chx}\, c_p \left(\frac{T'_{pt}}{T_{pt}} - ln\, \frac{T'_{pt}}{T^0} \right) - \dot{m}_{hhx}\, c_p \left(\frac{T''_{pt}}{T_{pt}} - ln\, \frac{T''_{pt}}{T^0} \right) , \qquad (2.97)
\end{aligned}
$$

where the gas mass content of the pulse tube is m_{pt} and m^0 is a constant. The cycle integration of Eq. (2.97) delivers with Eq. (2.91)

$$S_{irr,pt} = c_p \oint \left((\dot{m}_{chx} - \dot{m}_{hhx}) \, ln \, \frac{T_{pt}}{T^0} + \dot{m}_{chx} \left(\frac{T'_{pt}}{T_{pt}} - ln \, \frac{T'_{pt}}{T^0} \right) - \dot{m}_{hhx} \left(\frac{T''_{pt}}{T_{pt}} - ln \, \frac{T''_{pt}}{T^0} \right) \right) dt.$$
$$(2.98)$$

Using series expansion around $\tau - \tau_0 = 0$ the entropy production in the pulse tube can be expressed as

$$S_{irr,pt} = \sum_{i=2}^{\infty} b_{S_{pt},i} \, (\tau - \tau_0)^i. \qquad (2.99)$$

The entropy production rate in the **hot heat exchanger** is

$$\begin{aligned} \frac{dS_{irr,hhx}}{dt} &= \dot{m}_{hhx} \, c_p \left(\frac{T'_{hhx}}{T_h} - ln \, \frac{T'_{hhx}}{T^0} \right) - \dot{m}_{hhx} \, c_p \left(1 - ln \, \frac{T_h}{T^0} \right) \qquad (2.100) \\ &= \dot{m}_{hhx} \, c_p \left(\frac{T'_{hhx}}{T_h} - 1 - ln \, \frac{T'_{hhx}}{T_h} \right). \end{aligned}$$

Cycle integration delivers with Eq. (2.37), (2.47), (2.49) and (2.61)

$$\begin{aligned} S_{irr,hhx} &= \frac{c_p \, p_{min}}{R_s \, T_c} \frac{V_p \, r_d \, (1 - \tau_0 \, \epsilon)}{r_d \, (1 - \tau_0 \, \epsilon) + 1} \left(ln \, \frac{1 + \epsilon}{1 - \tau_0 \, \epsilon} - \frac{(\tau_0 + 1) \, \epsilon}{1 + \epsilon} \right) \\ &\quad + c_p \int_2^3 \dot{m}_{hhx} \left(\frac{T'_{hhx}}{T_h} - 1 - ln \, \frac{T'_{hhx}}{T_h} \right) dt. \qquad (2.101) \end{aligned}$$

Using Eq. (2.64) the entropy production in the hot heat exchanger can be expressed through series expansion around $\tau - \tau_0 = 0$ as

$$S_{irr,hhx} = \sum_{i=2}^{\infty} b_{S_{hhx},i} \, (\tau - \tau_0)^i. \qquad (2.102)$$

For the entropy production rate in the **regenerator** follows

$$\frac{dS_{irr,reg}}{dt} = \dot{m}_{hhx} \left(c_v \left(ln \, \frac{T_{reg}}{T^0} - 1 \right) + R_s \, ln \, \frac{V_{reg}}{V^0} \right) + \dot{m}_{hhx} \left(c_p \left(\frac{T_h}{T_{reg}} - ln \, \frac{T_h}{T^0} \right) + R_s \, ln \, \frac{p}{p^0} \right).$$
$$(2.103)$$

In Eq. (2.103) all terms except of p and $\dot{m}_{hhx}$ are constant. Thus, its cycle integration delivers

$$\begin{aligned} S_{irr,reg} &= \oint dS_{irr,cyl} = \left(c_v \left(ln \, \frac{T_{reg}}{T^0} - 1 \right) + c_v \left(\frac{T_h}{T_{reg}} - ln \, \frac{T_h}{T^0} \right) + R_s \, ln \, \frac{V_{reg}}{V^0} \right) \oint dm_{hhx} \\ &\quad + R_s \oint \dot{m}_{hhx} \, ln \, \frac{p}{p^0} \, dt \stackrel{(2.91)}{=} R_s \oint \dot{m}_{hhx} \, ln \, \frac{p}{p^0} \, dt. \qquad (2.104) \end{aligned}$$

With Eq. (2.45) Eq. (2.104) becomes

$$S_{irr,reg} \; = \; \frac{V_d}{(r_c \, - \, 1) \, (r_d \, + \, 1)} \, \frac{r_d}{T_{reg}} \oint ln \, \frac{p}{p^0} \, dp \; \overset{(2.60)}{=} \; 0 \, . \qquad (2.105)$$

In order to investigate basic loss mechanism, the obtained entropy production in the components can be used as a diagnostic tool. However, the total entropy production of the ideal pulse tube engine is caused by an entropy production in the heat exchangers and in the pulse tube.

2.3.6   Summary of the averaged model equations

The results for the pV-work, the amounts of heat transferred per cycle, the efficiency and the entropy productions are summarized.

The functions for the pV-work and the amounts of heat transferred per cycle, Eq. (2.68) and Eq. (2.75) to (2.78), as well as the functions for the entropy production, Eq. (2.95), (2.99) and (2.102), are expanded into series in $\tau - \tau_0$. The different orders of the series expansions are alternating around the exact solution. If the first order expansion is lower than the exact solution, the second order expansion is higher than the exact solution, the third order expansion is lower than the exact solution etc., see as an example Appendix **T** for the pV-work.

For the sake of simplified relations, applicable for the design of working pulse tube engines, the first and second order solution

$$\Upsilon_1 \approx a_0 \, + \, a_1 \, (\tau \, - \, \tau_0) \qquad (2.106)$$

and

$$\Upsilon_2 \approx a_0 \, + \, a_1 \, (\tau \, - \, \tau_0) \, + \, a_2 \, (\tau \, - \, \tau_0)^2 \, , \qquad (2.107)$$

respectively, are combined to an averaged solution

$$\overline{\Upsilon} \approx \lambda_\Upsilon \, \Upsilon_1 \, + \, (1 \, - \, \lambda_\Upsilon) \, \Upsilon_2 \, , \qquad (2.108)$$

which delivers sufficient results for $\lambda_\Upsilon = \frac{1}{2}$. Thus, Eq. (2.108) results in

$$\overline{\Upsilon} \approx \frac{\Upsilon_1}{2} \, + \, \frac{\Upsilon_2}{2} \; = \; a_0 \, + \, a_1 \, (\tau \, - \, \tau_0) \, + \, \frac{a_2}{2} \, (\tau \, - \, \tau_0)^2 \, . \qquad (2.109)$$

According to subsection 2.3.4 the constant term a_0 of Eq. (2.109) disappears.

The absolute value of the linear component of the pV-work in $\tau - \tau_0$ is

$$W_{pV_l} = p_{min} \, V_d \, \frac{r_d \, (\tau - 1) - 1}{(r_d + 1)^2} \,, \tag{2.110}$$

where Eq. (2.81) is used for τ_0.

With Eq. (2.109), expressed in terms of W_{pV_l}, it follows for the pV-work

$$W_{pV} \approx - W_{pV_l} \, (1 + \chi_{pV}) \,, \tag{2.111}$$

for the amount of heat transferred per cycle in the cylinder

$$Q_{cyl} \approx W_{pV_l} \, (1 + \chi_{cyl}) \,, \tag{2.112}$$

for the amount of heat transferred per cycle in the cold heat exchanger

$$Q_{chx} \approx - W_{pV_l} \, \frac{\kappa \, (r_d + 1)}{\kappa - 1} \, (1 + \chi_{chx}) \,, \tag{2.113}$$

for the amount of heat transferred per cycle in the pulse tube

$$Q_{pt} \approx W_{pV_l} \, \frac{\kappa \, (r_d + 1)}{\kappa - 1} \, \chi_{pt} \,, \tag{2.114}$$

and for the amount of heat transferred per cycle in the hot heat exchanger

$$Q_{hhx} \approx W_{pV_l} \, \frac{\kappa \, (r_d + 1)}{\kappa - 1} \, (1 + \chi_{hhx}) \,. \tag{2.115}$$

For the amount of heat transferred per cycle in the pulse tube, the linear coefficient a_1 disappears as well. The functions χ can be interpreted as linear perturbations of the linear solution [66]. The respective perturbation functions are

$$\chi_{pV} = \chi_{cyl} = - \frac{\left(4 \, r_d^3 \, (r_c + 1) + r_c \, (6 \, r_d^2 + 4 \, r_d + 1)\right) (r_d \, (\tau - 1) - 1)}{4 \, (2 \, r_d + 1) \, (r_d + 1)^2 \, (2 \, r_d \, (r_c + 1) + r_c)} \,, \tag{2.116}$$

$$\chi_{chx} = \frac{r_d \, (r_d \, (\tau - 1) - 1)}{(r_d + 1)^2 \, (2 \, r_d \, (r_c + 1) + r_c)} \,, \tag{2.117}$$

$$\chi_{pt} = \frac{\left(r_c^2 \, (2 \, r_d + 1) + 4 \, r_d \, r_c \, (r_d + 1) - 4 \, r_d^2\right) (r_d \, (\tau - 1) - 1)}{4 \, (r_d + 1)^2 \, \left(r_c^2 \, (2 \, r_d + 1)^2 + 2 \, r_d \, r_c \, (2 \, r_d + 1)\right)} \tag{2.118}$$

and

$$\chi_{hhx} = \frac{(2 \, r_d - r_c) \, (r_d \, (\tau - 1) - 1)}{4 \, (r_d + 1)^2 \, r_c \, (2 \, r_d + 1)} \,. \tag{2.119}$$

The amount of heat transferred per cycle in the regenerator is equal to zero.

For the thermal efficiencies follows

$$\eta_{th}^{\overline{=}} \approx \frac{\kappa - 1}{\kappa\,(r_d + 1)}\,(1 - f_1) \tag{2.120}$$

and

$$\eta_{th}^{<} \approx \frac{\kappa - 1}{\kappa\,(r_d + 1)}\,(1 - f_2)\,, \tag{2.121}$$

where the functions

$$f_1 = \frac{2\,r_d\,(r_d\,(\tau - 1) - 1)\,(2\,r_c\,r_d^2\,(r_c + 1) + r_d\,(3\,r_c^2 + 2\,(r_c + 1)) + r_c^2)}{(8\,r_c\,r_d^3 + r_d^2\,(2\,(\tau - 1) + 20\,r_c) + r_d\,(r_c\,(17 - \tau) - 2) + 5\,r_c)\,(2\,r_d\,(r_c + 1) + r_c)} \tag{2.122}$$

and

$$f_2 = \frac{(r_d\,(\tau - 1) - 1)\,(4\,r_d^3\,(r_c + 1) + r_d^2\,(6\,r_c + 8) + 4\,r_d\,(r_c + 1) + r_c)}{4\,(2r_d + 1)\,(r_d^3\,(2\,r_c + 2) + r_d^2\,(5\,r_c + 3 + \tau) + r_d\,(4\,r_c + 1) + r_c)} \tag{2.123}$$

have the property

$$\lim_{\tau \to \tau_0} f_1 = \lim_{\tau \to \tau_0} f_2 = 0\,.$$

Entropy is produced in the two heat exchangers and in the pulse tube. With Eq. (2.109) follows, expressed in terms of W_{pV_l}, the entropy production in the cold heat exchanger with

$$S_{irr,chx} \approx W_{pV_l}\,\frac{\kappa\,(r_d\,(\tau - 1) - 1)}{4\,T_c\,(\kappa - 1)}\,, \tag{2.124}$$

in the pulse tube with

$$S_{irr,pt} \approx W_{pV_l}\,\frac{\kappa\,r_d\,(2\,r_d^2\,(r_c + 1) + r_c\,(3\,r_d + 1))\,(r_d\,(\tau - 1) - 1)}{2\,r_c\,T_c\,(\kappa - 1)\,(2\,r_d + 1)^2\,(r_d + 1)^2\,(2\,r_d\,(r_c + 1) + r_c)}\,, \tag{2.125}$$

and in the hot heat exchanger with

$$S_{irr,hhx} \approx W_{pV_l}\,\frac{\kappa\,r_d\,(r_d\,(\tau - 1) - 1)}{4\,T_c\,(\kappa - 1)\,(r_d + 1)}\,. \tag{2.126}$$

In the other components the entropy production is zero.

The predictions for the ideal pulse tube engine cycle summarized in this subsection are in combination with Eq. (2.110) the approximation of the pV-work in Eq. (2.111), and the approximations of the amounts of heat transferred per cycle in Eq. (2.112) to (2.115) as well as the approximations of the thermal efficiencies in Eq. (2.120) to (2.123).

Obtained diagnostic tools, in combination with Eq. (2.110), are the approximations of the entropy production in the heat exchangers and the pulse tube obtained in Eq. (2.124) to (2.126).

2.4   Consistency tests and accuracy evaluation

To prove the correctness of the analytical model, the obtained exact results for the time-dependent pressure, the pV-work, the amount of heat transferred per cycle and the entropy production due to irreversibility are used to check the conservation of mass and energy as well as the entropy balance. After this step the accuracy of the approximated solutions introduced in subsection 2.3.6 are compared to the exact solutions.

2.4.1   Consistency tests of the exact model equations

The consistency of the derived analytical model is investigated in two ways. First, the conservation of mass Eq. (2.1) and internal energy Eq. (2.4) as well as the balance equation of the entropy Eq. (2.10) are checked with the calculated results for the pressure, the work output, the transferred amounts of heat and entropy as well as the entropy productions. Only the results are shown. The interested reader will find further details in Appendix **T**. Second, the engine cycle is calculated for $\epsilon = 0$, respectively $\tau = \tau_0$, which leads to an isothermal compression and expansion device having no cycle work output.

The conservation of mass throughout the cycle is already shown in subsection 2.3.3 with Eq. (2.60). The pressure at the end of the cycle p_1^* is equal to the pressure at the beginning of the cycle p_1. Thus, no mass is lost and

$$\oint \frac{dm}{dt}\, dt = \oint \sum_i \dot{m}_i'\, dt + \oint \sum_i \dot{m}_i''\, dt \overset{!}{=} 0$$

is fulfilled.

Energy conversion throughout the entire cycle demands

$$\oint \frac{dU}{dt}\, dt = \oint \dot{W}\, dt + \oint \sum_i \dot{Q}_i\, dt + \oint \sum_i \dot{H}_i'\, dt + \oint \sum_i \dot{H}_i''\, dt$$

$$= \oint \dot{W}\, dt + \sum_i \oint \dot{Q}_i\, dt = W_{pV} + Q_{cyl} + Q_{chx} + Q_{pt} + Q_{hhx} + Q_{reg} \overset{!}{=} 0\,,$$

$$(2.127)$$

where

$$\oint \sum_i \dot{H}'_i \, dt \; + \; \oint \sum_i \dot{H}''_i \, dt \; = \; 0$$

is used for the enthalpy fluxes between the components. The fulfillment of Eq. (2.127) is shown in Appendix **T**.

Closing the cycle also demands

$$
\begin{aligned}
\oint \frac{dS}{dt} \, dt &= \oint \sum_i \frac{\dot{Q}_i}{T_i} \, dt \; + \; \oint \sum_i \dot{S}'_i \, dt \; + \; \oint \sum_i \dot{S}''_i \, dt \; + \; \oint \sum_i \frac{dS_{irr,i}}{dt} \, dt \\
&= \sum_i \oint \frac{\dot{Q}_i}{T_i} \, dt \; + \; \oint \sum_i \frac{dS_{irr,i}}{dt} \, dt \\
&= \sum_i \oint \frac{\dot{Q}_i}{T_i} \, dt \; + \; \sum_i S_{irr,i} \; \overset{!}{=} \; 0 \, ,
\end{aligned}
\tag{2.128}
$$

where

$$\oint \sum_i \dot{S}'_i \, dt \; + \; \oint \sum_i \dot{S}'''_i \, dt \; = \; 0$$

is used for the entropy fluxes between the components. Except for the pulse tube, the temperatures are constant throughout the cycle. Thus, together with $Q_{reg} = 0$, Eq. (2.128) becomes

$$\oint \frac{dS}{dt} \, dt \; = \; \frac{Q_{cyl}}{T_c} \; + \; \frac{Q_{chx}}{T_c} \; + \; \frac{Q_{hhx}}{T_h} \; + \; \oint \frac{\dot{Q}_{pt}}{T_{pt}} \, dt \; + \; S_{irr,t} \; \overset{!}{=} \; 0 \, . \tag{2.129}$$

The fulfillment of Eq. (2.129) is also shown in Appendix **T**.

Going back to the beginning of subsection 2.3.3. The parameter ϵ is set to be $\epsilon = 0$. In this case the abbreviations C_c and C_e become $C_c = C_e = C$. For the pressure after the compression stroke p_2 follows with Eq. (2.49)

$$p_2 \; = \; p_1 \, \frac{V_d + C}{C} \, .$$

Since now $T_{pt,c} = T_{pt,e}$ the pressure p_3 becomes, according to Eq. (2.52), $p_3 = p_2$. For the pressure after the expansion stroke p_4 follows with Eq. (2.56)

$$p_4 \; = \; p_3 \, \frac{C}{V_d + C} \; = \; p_2 \, \frac{C}{V_d + C} \; = \; p_1 \, \frac{V_d + C}{C} \, \frac{C}{V_d + C} \; = \; p_1 \, .$$

Thus, the compression occurs at the same isothermal curve as the expansion, and the engine should not provide a work output. This can be proven with Eq. (2.67) which

becomes

$$W_{pV} \; = \; \sum_{i=1}^{\infty} a_i \, \epsilon^i \; \overset{\epsilon=0}{=} \; 0 \, .$$

Similarly, all amounts of heat transferred per cycle calculated with Eq. (2.75) to (2.78) become

$$Q_{cyl} \; = \; Q_{chx} \; = \; Q_{pt} \; = \; Q_{hhx} \; \overset{\epsilon=0}{=} \; 0 \, .$$

The amount of heat transferred per cycle in the regenerator is naturally zero.

To complete the consistency tests, the calculated entropy production is analyzed. In the cylinder and the regenerator, the entropy production is zero. This result is obvious since in these components the gas temperature is constant throughout the cycle and no gas at a different temperature than the component gas temperature enters the components. In the heat exchangers the temperature is constant throughout the cycle, but gas at a different temperature than the heat exchanger gas temperature flows from the pulse tube into the heat exchangers and causes entropy production due to gas mixing [64]. In the pulse tube, the temperature changes during the thermal relaxations at TDC and BDC, leading to entropy production [57]. Gas entering the pulse tube from the heat exchangers mixes with the remaining gas. Furthermore, during the thermal relaxation from state 2 to state 3 and the thermal relaxation from state 4 to state 1 gas is mixed within the pulse tube, leading to a relaxation of the temperature gradient in the pulse tube [24]. This causes additional entropy production.

In summary, the consistency test demonstrates that the analytical model satisfies the conservation of mass and internal energy as well as the entropy balance. The calculated entropy production in the components is physically reasonable.

2.4.2   Accuracy evaluation of the model equations

To show the accuracy of the used approximation according to Eq. (2.109), the pV-work, the amounts of heat transferred per cycle, the thermal efficiencies and the entropy productions are calculated exactly, with the linear and second order approximation and with the averaging method introduced in subsection 2.3.6.

A virtual engine having the characteristics $r_c = r_d = 1$, $p_{min}V_d = 1\,\mathrm{J}$ and $T_c = 300\,\mathrm{K}$ is simulated. It uses helium, regarded as a perfect gas with $\kappa = 1.66$, as working fluid. The minimum operating temperature ratio of this engine is according to Eq. (2.81) $\tau_0 = 2$ $(T_h = 600\,\mathrm{K})$. The cycle is calculated for temperature ratios between 1 $(T_h = 300\,\mathrm{K})$ and 5 $(T_h = 1500\,\mathrm{K})$.

(a) pV- work

(b) Heat transferred per cycle in the cylinder

(c) Heat transferred per cycle in the chx

(d) Heat transferred per cycle in the pulse tube

(e) Heat transferred per cycle in the hhx

(f) Thermal efficiencies
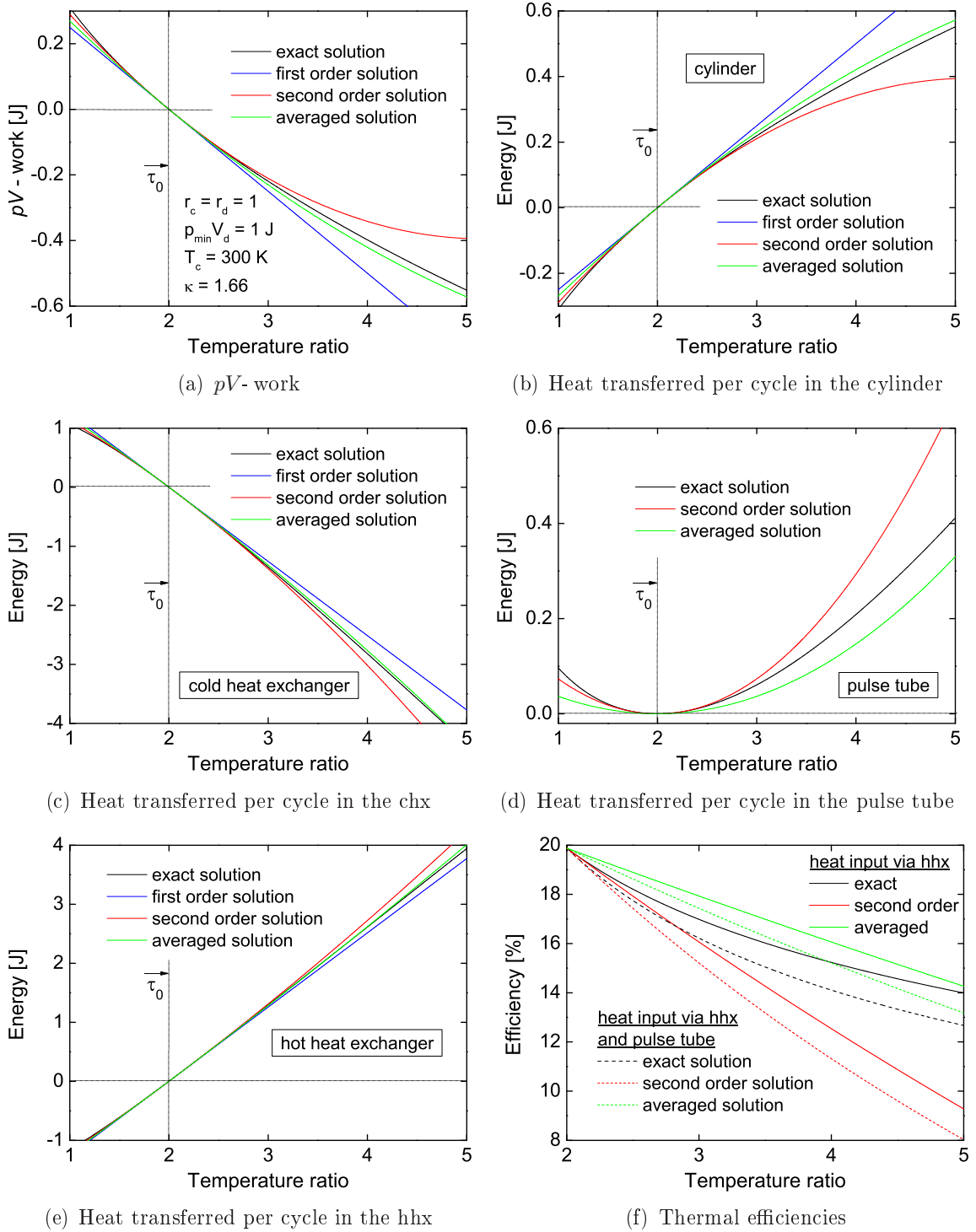
Figure 2.6: Comparison of the exact solution with the linear, second order and averaged solution for the pV- work, the amounts of heat transferred per cycle and the thermal efficiencies as functions of the temperature ratio τ. The exact solution of the pV- work is calculated with Eq. (2.66), of the amounts of heat transferred per cycle with Eq. (2.75) to (2.78), and of the thermal efficiencies with Eq. (2.85) and (2.87). Under consideration of Eq. (2.108) and (2.109), the linear, second order and averaged solutions of the pV- work are calculated with Eq. (2.110) and (2.111), of the amounts of heat transferred per cycle with Eq. (2.110) and Eq. (2.112) to (2.115), and of the thermal efficiencies with Eq. (2.120) to (2.123).

In Fig. 2.6, a comparison of the pV-work, the amounts of heat transferred per cycle and the thermal efficiencies is shown. The averaged solution is a good approximation of the exact solution for the pV-work, and of the exact solutions for the amounts of heat transferred per cycle in the cylinder and in the heat exchangers. The results of the linear and the second order solutions for $\tau < \tau_0$ and $\tau > \tau_0$ spread further from the exact solutions. Since the amount of heat transferred per cycle in the pulse tube has no linear solution, the averaged solution is smaller than the exact solution. The averaged solutions for the thermal efficiencies deliver sufficient results.

All energies are zero at $\tau = \tau_0 = 2$, whereas the thermal efficiency has its maximum at τ_0. For $\tau < \tau_0$ the pV-work is positive, and work has to be delivered to the engine, which is thus not working as a prime mover. In this case heat is added to the working gas in the cold heat exchanger and rejected in the hot heat exchanger. The engine is operating as a heat pump. For $\tau > \tau_0$ the pV-work is negative and the engine is operating as a prime mover. Heat is added to the working gas in the hot heat exchanger and rejected in the cold heat exchanger. Since $r_c = 1$, according to the results of subsection 2.3.4, heat is always added to the working gas in the pulse tube, but the amount of heat transferred per cycle in the pulse tube is much smaller than in the other components.

Fig. 2.7 shows the entropy production per cycle in the two heat exchangers and the pulse tube. The entropy production has no linear solution. The second order solution always exceeds the exact solution, whereas the averaged solution is smaller than the exact solution, except in the hot heat exchanger. There, the averaged solution exceeds the entropy production for higher temperature ratios. Most entropy is produced in the heat exchangers. This is caused by the gas coming from the middle of the pulse tube with a higher respectively lower temperature than the gas temperature of the heat exchanger. Since the mass flow rate

Figure 2.7: Comparison of the exact calculated entropy production with the second order and averaged solution in the heat exchangers and the pulse tube as functions of τ. The exact values are calculated with Eq. (2.94), (2.98) and (2.101). Considering Eq. (2.108) and (2.109), the second order and averaged entropy productions are calculated with Eq. (2.110) and Eq. (2.124) to (2.126).

through the cold heat exchanger is higher than through the hot heat exchanger, the entropy production in the cold heat exchanger is highest. For all $\tau \neq \tau_0$ entropy is produced by the cycle. Thus, the ideal pulse tube engine is always irreversible.

The accuracy evaluation shows that the approximated equations presented in sub-section 2.3.6 are sufficiently accurate in order to predict the performance of the ideal pulse tube engine and to diagnose its entropy production.

## 2.5 Analytical predictions for the pulse tube engine

In this section the thermodynamic cycle of the pulse tube engine is studied analyti-cally. The influence of the parameters temperature ratio τ, compression ratio r_c and distribution ratio r_d on the engine behavior is determined.

The virtual engine introduced in subsection 2.4.2 with the characteristics $p_{min}V_d = 1\,\mathrm{J}$, $T_c = 300\,\mathrm{K}$ and $\kappa = 1.66$ is used. The minimal pressure is $p_{min} = 1\,\mathrm{bar}$ and the displacement volume is $V_d = 10\,\mathrm{cm}^3$. The cycle is calculated for different temperature ratios, distribution ratios and compression ratios.

2.5.1 Influence of the temperature ratio

The influence of the temperature ratio on the thermodynamic cycle is investigated.

In subsection 2.3.3 the time-dependent pressure has been derived. The compression and expansion pressure can be calculated with Eq. (2.48) and (2.55), respectively.
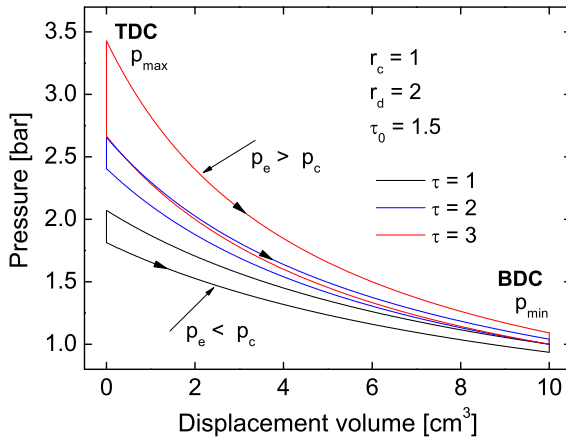
Figure 2.8: pV-diagram of the virtual engine, calculated with Eq. (2.48) and (2.55) for $r_c = 1$, $r_d = 2$ and temperature ratios of 1, 2 and 3.

Fig. 2.8 shows the resulting pV-diagram of the virtual engine for $r_c = 1$, $r_d = 2$ and temperature ratios of 1, 2 and 3. The minimal temperature ra-tio for engine operation is $\tau_0 = 1.5$ ($T_h = 450\,\mathrm{K}$).

The slopes of the isothermal com-pression and expansion increase with an increase of τ. For $\tau = 1$ the expansion stroke is on a lower pressure level than the compression stroke. In this case pV-work has to be delivered to the engine. For $\tau = 2$ and $\tau = 3$ the expansion stroke is on a higher pressure level than the compression stroke and the engine provides a pV-work output. The intensity of the isochoric pressure rise at TDC is highly dependent on τ. In the case of $\tau = 1$, the gas in the pulse tube is cooled at the end of the compression stroke, since its compression end temperature is higher than the pulse tube's material temperature. For higher temper-

ature ratios, the compression end temperature is lower than the pulse tube's material temperature resulting in a heat addition to the gas at TDC. The same happens at BDC, but with an opposite sign of the pulse tube heat flux. If the temperature ratio is too small, the gas expands below the pulse tube's material temperature and takes on heat at BDC. Having higher temperature ratios, the gas temperature in the pulse tube does not fall under the pulse tube's material temperature and heat is rejected at BDC.

2.5.2 Influence of the compression ratio

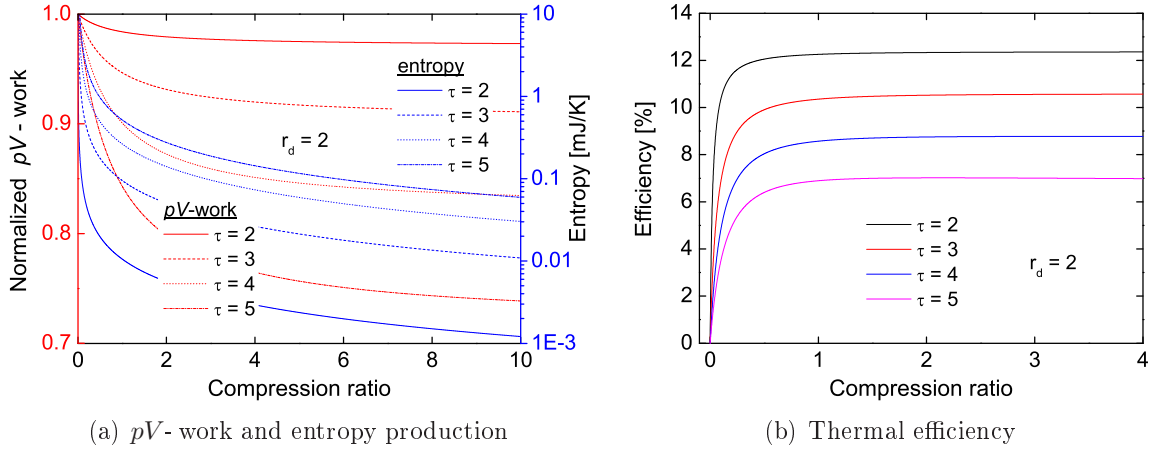The influence of the compression ratio on the engine cycle is analyzed.
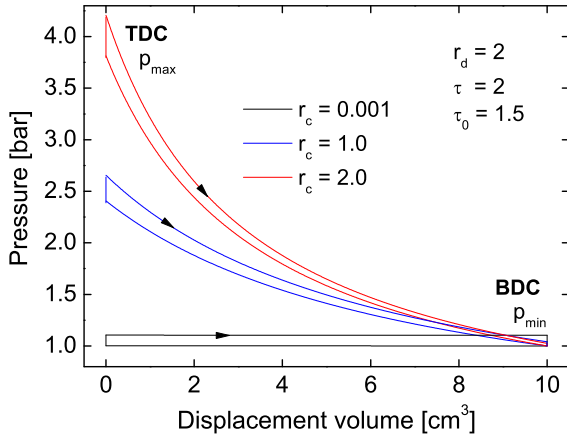
Figure 2.9: pV-diagram of the virtual engine, calculated with Eq. (2.48) and (2.55) for $\tau = 2$, $r_d = 2$ and compression ratios of 0.001, 1 and 2.

In Fig. 2.9 the pV-diagram of the virtual engine for $r_d = 2$, $\tau = 2$ and compression ratios of 0.001, 1 and 2 is shown. As expected from the theory, the pressure rise during compression increases for higher values of r_c. For all compression ratios the isothermal expansion is on a higher pressure level than the isothermal compression. Thus, the engine provides a work output for all values of $r_c > 0$. The surface enclosed by the pV-curve is comparable for all compression ratios. For $r_c \to 0$ the temperature change during compression and expansion becomes zero. According to Eq. (2.125) the entropy production in the pulse tube becomes singular, and thus, the energy dissipation becomes infinite. This hampers an operation of the engine for $r_c \to 0$. The calculated work output for $r_c \to 0$ is only a theoretical potential value for $Q_{in} \to \infty$.

According to Eq. (2.111) in combination with Eq. (2.116) the pV-work is only of second order dependent on r_c. To show this, the pV-work is plotted in Fig. 2.10 (a) as a function of the compression ratio, for $r_d = 2$ and temperature ratios of 2, 3, 4 and 5. The values are normalized to the value for $r_c = 0$.

The dependency of the pV-work on r_c is evident. For small temperature ratios the influence of r_c is insignificant. Nevertheless, an increase of r_c reduces the pV-work of the pulse tube engine slightly. The influence of the compression ratio on the pV-work increases with the temperature ratio. On the other hand, according to Eq. (2.125), an increase of r_c decreases the entropy production in the pulse tube. This is also shown

(a) pV-work and entropy production

(b) Thermal efficiency

Figure 2.10: (a) Normalized pV-work as a function of the compression ratio, calculated with Eq. (2.110), (2.111) and (2.116), as well as the entropy production in the pulse tube as a function of the compression ratio, calculated with Eq. (2.110) and (2.125), of the virtual engine having a distribution ratio of $r_d = 2$ and temperature ratios of 2, 3, 4 and 5; (b) Corresponding thermal efficiency, calculated with Eq. (2.120) and (2.122).

in Fig. 2.10 (a). Thus, the power output of the real pulse tube engine should have an optimal compression ratio at which the power output is best. This peak value should be located in the region of high $dS_{irr,pt}/d\tau$, around $r_c = 1$.

The thermal efficiency, calculated with Eq. (2.120), is shown in Fig. 2.10 (b). With increasing compression ratios up to $r_c = 1$ the thermal efficiency increases rapidly and remains constant for higher compression ratios. This strengthens the assumption of a peak pV-work around $r_c = 1$.

2.5.3 Influence of the distribution ratio

The distribution ratio, discovered in subsection 2.3.4 to be an important characteristic of the pulse tube engine, is studied with respect to its influence on the engine cycle.

Fig. 2.11 shows the pV-diagram of the virtual engine for $r_c = 1$, $\tau = 2$ and distribution ratios of 0.5, 1.2 and 3. For $r_d = 0.5$ the engine does not provide a work output. Increasing the distribution ratio enables the cycle to convert heat into work. An increase of the distribution ratio increases the regenerator volume and decreases the pulse tube volume. This directly influences the thermodynamic asymmetry caused by the arrangement of pulse tube and regenerator. A higher value of r_d increases the mass flux passing the pulse tube and the hot heat exchanger, but decreases the mass content experiencing a thermal relaxation in the pulse tube. Thus, an optimal value of r_d, maximizing the pV-work, exists. This can be shown using the linear component of
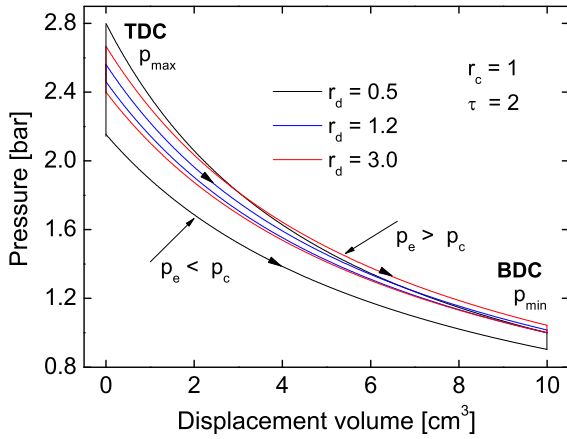
the pV- work. The first derivative of Eq. (2.110) in r_d is

$$\frac{dW_{pV}}{dr_d} \approx p_{min} V_d \frac{r_d (\tau - 1) - (\tau + 1)}{(r_d + 1)^3} , \qquad (2.130)$$

which becomes zero for

$$r_{d,opt} \approx \frac{\tau + 1}{\tau - 1} . \qquad (2.131)$$

For different temperature ratios the pV- work is calculated and shown in Fig. 2.12 (a).

Figure 2.11: pV- diagram of the virtual engine, calculated with Eq. (2.48) and (2.55) for $\tau = 2$, $r_c = 1$ and distribution ratios of 0.5, 1.2 and 3.

The strong dependency of the pV- work on the distribution ratio is evident. The influence of the regenerator on the cycle becomes obvious. The lower the available temperature ratio, the higher the value of r_d and thus the higher the necessary regenerator gas volume to enable a pV- work output. As expected, exceeding the optimal distribution ratio leads to a decrease of the pV- work output. Since according to Eq. (2.131) the peak value is a function of the temperature ratio, a careful design of the pulse tube engine with respect to the distribution ratio is necessary. The found relation in Eq. (2.131) delivers an approximation of the optimal distribution ratio. In contrast, the thermal efficiency, calculated with Eq. (2.120) and (2.122), and shown in Fig. 2.12 (b) does not have a peak value at any distribution ratio. To increase the thermal efficiency the distribution ratio has to be small. According to Eq. (2.81) the minimal temperature ratio τ_0, above which the engine provides a work output is a function of r_d. Thus, the lowest possible value of r_d is limited by the available temperature ratio.

As shown above the analytical model is applicable to predict the influence of the temperature ratio, the compression ratio and the distribution ratio on the engine performance. The analytical model will be verified in section 2.9 with the results of the numerical model.

(a) pV-work   (b) Thermal efficiency

Figure 2.12: (a) pV-work as a function of the distribution ratio, calculated with Eq. (2.110), (2.111) and (2.116), of the virtual engine having a compression ratio of $r_c = 1$ and temperature ratios of 1.5, 2, 2.5, 3 and 3.5; (b) Corresponding thermal efficiency, calculated with Eq. (2.120) and (2.122).

2.6 Summary and conclusions of the analytical model

The basic characteristics of the pulse tube engine which were found are summarized as follows:

1. According to Fig. 2.6 and 2.7, entropy is always produced if heat is converted into pV-work and vice versa. This becomes obvious regarding Eq. (2.124) to (2.126). The entropy production is proportional to the pV-work. Thus, the irreversible nature of the pulse tube engine ($\tau > \tau_0$) and the pulse tube heat pump ($\tau < \tau_0$) is proven.

2. The ideal pulse tube engine starts to operate at a temperature ratio $\tau \geq \tau_0 > 1$, where according to Eq. (2.81), $\tau_0 = (r_d + 1)/r_d$ is determined by the distribution ratio only. The pV-work output is zero for $\tau = \tau_0$ and is increasing monotonously for $\tau > \tau_0$, whereas the thermal efficiency has its maximum at $\tau = \tau_0$ and is decreasing monotonously for $\tau > \tau_0$. This is a result of the strong increase of the entropy production, and an only moderately increasing pV-work output. Thus, the pulse tube engine is preferably suited for low temperature ratios τ, which are bound to the condition $\tau > \tau_0$.

3. For the ideal engine, Eq. (2.111) and (2.112) in combination with Eq. (2.110) and (2.116) disclose that the heat converted into pV-work is added to the working gas in the cylinder only. The entire heat added to the working gas in the hot heat exchanger and the pulse tube is rejected in the cold heat exchanger. This effect enables a pulse tube engine with a non-isothermal cylinder to produce cooling

energy in the cylinder. The pulse tube engine can thus act as a thermal driven refrigerator, absorbing heat in the cylinder. Even if the thermal energy applied in the hot heat exchanger and the pulse is not converted into pV-work it is essential for the engine to operate.

4. Since heat is added to the working gas in the pulse tube, the pulse tube engine is able to use heat sources with variable temperature. It is possible to design a pulse tube engine, which cools down a fluid, beginning at the hot heat exchanger, along the pulse tube to the cold heat exchanger. This allows for the removal of a larger amount of heat from a thermal energy carrying fluid compared to e.g. the Stirling engine, which is only able to use heat at a small temperature range.

5. The isothermal analysis of the pulse tube engine discloses only a second order dependency of the pV-work on the compression ratio. In this analysis, no optimal value of the compression ratio could be found. Since the pV-work and the entropy production in the pulse tube are decreasing for an increase of the compression ratio, the pV-work output of the non-ideal pulse tube engine should have a peak value around $r_c = 1$. The thermal efficiency increases for compression ratios up to $r_c = 1$. For higher compression ratios it remains constant.

6. The pV-work and the efficiency of the pulse tube engine are strongly dependent on the distribution ratio. The pV-work output is maximal for a certain value of r_d, which can be estimated with Eq. (2.131) to $r_{d,opt} \approx (\tau + 1)/(\tau - 1)$. The thermal efficiency decreases monotonously with increasing distribution ratios.

The listed properties of the pulse tube engine give a pathway for its potential applications and engineering challenges.

2.7   Numerical model of the pulse tube engine

In order to get a more precise understanding of the pulse tube engine's underlying energy conversion process and the influence of design parameters on the engine performance a non-isothermal mathematical model on the basis of a control volume analysis is developed and solved numerically [67] using the programming language Modelica. A related prior numerical approach on the pulse tube engine process is shown in [24].

2.7.1 Numerical method

The used numerical schemes to solve the model equations are based on discretization and integration methods of [68, 69].

To all engine components Eq. (2.3) for the pressure, Eq. (2.7) for the gas temperature, Eq. (2.9) for the material temperature and Eq. (2.23) for the temporal change of the mass flux are applied. An entropy balance is not performed in this analysis. Due to the high temperature gradients, the pulse tube and the regenerator are each divided into sub-control volumes. The other components consist of one control volume each (see Fig. 2.1 (b) for the mixed zero/one-dimensional approach). All left side fluxes $\dot{m}'$, $\dot{Q}'_{cg}$, $\dot{Q}'_{cm}$ and $\dot{H}'$ are positive, and all right side fluxes $\dot{m}''$, $\dot{Q}''_{cg}$, $\dot{Q}''_{cm}$ and $\dot{H}''$ are negative. Material temperatures have the index T_m, whereas gas temperatures T have no index.

Cylinder

The cylinder volume and the cylinder heat transfer area vary in time, given by [70]

$$V = V_0 + \frac{V_d}{2}\left(1 + r_{cr} - cos\left(\omega t - \phi\right) - \sqrt{r_{cr}^2 - sin^2\left(\omega t - \phi\right)}\right) \qquad (2.132)$$

and

$$A_{hx} = A_{hx0} + \frac{A_{hx_d}}{2}\left(1 + r_{cr} - cos\left(\omega t - \phi\right) - \sqrt{r_{cr}^2 - sin^2\left(\omega t - \phi\right)}\right), \quad (2.133)$$

where the crank ratio $r_{cr} = 2\,L_r/s$ is the ratio between piston rod length L_r and crank radius $s/2$, which is half of the stroke s. The angular frequency is defined by $\omega = 2\,\pi\,f$ and the starting position of the piston is ϕ, where $\phi = 0$ at TDC. The engine's dead volume and the displacement volume are represented by V_0 and $V_d = \pi\,d^2 s/4$. The entire engine's dead volume V_0 is assigned to the cylinder volume. Thus, the minimal cylinder heat transfer area is calculated with $A_{hx0} = 4\,V_0/d + \pi\,d^2/2$, where d represents the piston diameter, and the dead volume V_0 is regarded as cylindric volume having the diameter d and the cylinder shell surface $4\,V_0/d$. The area of the two cylinder cover surfaces is calculated to $\pi\,d^2/2$. The displacement area is given by $A_{hx_d} = \pi\,d\,s$.

The cylinder pressure is calculated with

$$\frac{dp}{dt} = -\frac{R_s\,T}{V}\,\dot{m}'' - \frac{p}{V}\,\frac{dV}{dt} + \frac{p}{T}\,\frac{dT}{dt}, \qquad (2.134)$$

the gas temperature with

$$\frac{c_v\,p\,V}{R_s\,T}\,\frac{dT}{dt} = c_v\,T\,\dot{m}'' + \dot{Q}_{hx} - \dot{Q}''_{cg} - p\,\frac{dV}{dt} - \dot{m}''c_p\,T'', \qquad (2.135)$$

the material temperature with

$$\rho_m \, V_m \, c_m \, \frac{dT_m}{dt} \; = \; -\,\dot{Q}_{hx} \; - \; \dot{Q}''_{cm} \; + \; \dot{Q}_{ext,cyl} \,, \tag{2.136}$$

and the temporal change of the mass flux $\dot{m}$ with

$$\frac{d\dot{m}}{dt} \; = \; -\,\frac{R_s}{V} \, \frac{\dot{m}''^2 \, T''}{p''} \; + \; \frac{A_f^2}{V} \, (p \, - \, p'') \; - \; \frac{2 \, f_f \, R_s \, T \, \dot{m} \, |\dot{m}|}{p \, A_f \, d_h} \,, \tag{2.137}$$

where the assumption $p' = p$ is used.

Heat exchangers

The heat exchanger pressure is calculated with

$$\frac{dp}{dt} \; = \; \frac{R_s \, T}{V} \, (\dot{m}' \, - \, \dot{m}'') \; + \; \frac{p}{T} \, \frac{dT}{dt} \,, \tag{2.138}$$

the gas temperature with

$$\frac{c_v \, p \, V}{R_s \, T} \, \frac{dT}{dt} \; = \; -\,c_v \, T \, (\dot{m}' \, - \, \dot{m}'') \; + \; \dot{Q}_{hx} \; + \; \dot{Q}'_{cg} \; - \; \dot{Q}''_{cg} \; + \; \dot{m}' \, c_p \, T' \; - \; \dot{m}'' c_p \, T'', \tag{2.139}$$

the material temperature with

$$\rho_m \, V_m \, c_m \, \frac{dT_m}{dt} \; = \; -\,\dot{Q}_{hx} \; + \; \dot{Q}'_{cm} \; - \; \dot{Q}''_{cm} \; + \; \dot{Q}_{ext,chx/hhx} \,, \tag{2.140}$$

and the temporal change of the mass flux $\dot{m}$ with

$$\frac{d\dot{m}}{dt} \; = \; \frac{R_s}{V} \left(\frac{\dot{m}'^2 \, T'}{p'} \, - \, \frac{\dot{m}''^2 \, T''}{p''} \right) \; + \; \frac{A_f^2}{V} \, (p' \, - \, p'') \; - \; \frac{2 \, f_f \, R_s \, T \, \dot{m} \, |\dot{m}|}{p \, A_f \, d_h} \,. \tag{2.141}$$

The second cold heat exchanger chx$_2$, in general, is closed at its right side. In this case $\dot{m}'' = 0$ and the assumption $p'' = p$ is used.

Pulse tube and regenerator

Both components have constant volumes. Since pulse tube and regenerator are located between hot and cold heat exchangers, they have strong axial temperature distributions. To take this characteristic into account, the regenerator and the pulse tube are each divided into n sub-control volumes i with a characteristic temperature T_i.

(a) Discretization of the pulse tube   (b) Discretization of the regenerator
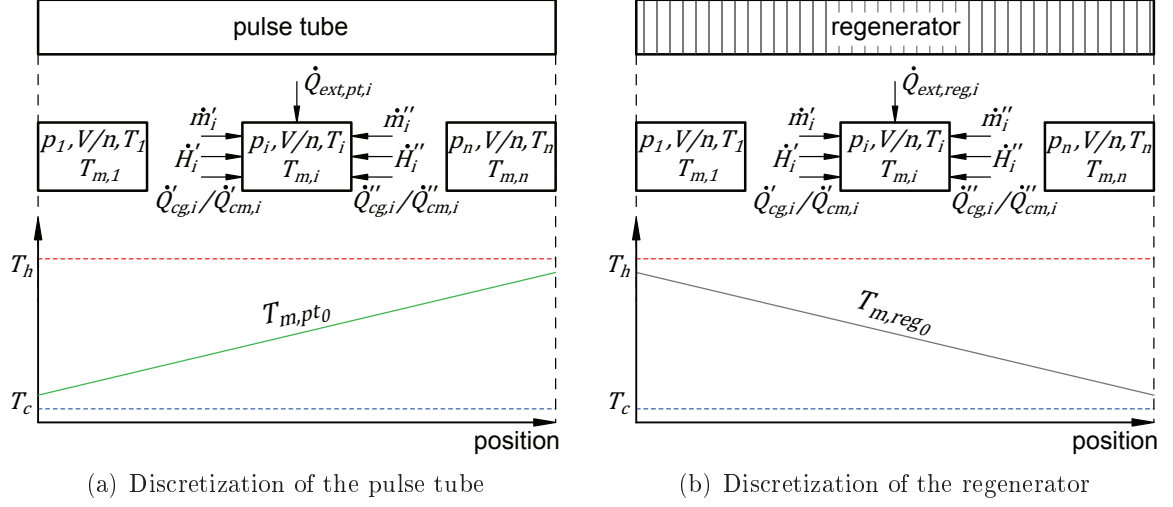
Figure 2.13: Discretization of (a) pulse tube and (b) regenerator. Both components are divided in a number n of sub-control volumes, which can differ for both components. Each sub-control volume i has the pressure p_i, the gas temperature T_i and the material temperature $T_{m,i}$. Between the sub-control volumes mass fluxes $\dot{m}_i'$ and $\dot{m}_i''$, enthalpy fluxes $\dot{H}_i'$ and $\dot{H}_i''$, as well as heat fluxes due to heat conduction $\dot{Q}_{cg,i}'$, $\dot{Q}_{cm,i}'$, $\dot{Q}_{cg,i}''$ and $\dot{Q}_{cm,i}''$ are exchanged. Fluxes at the left respectively right sub-control volume border are denoted with $'$ and $''$. The heat fluxes $\dot{Q}_{ext,pt/reg,i}$ are exchanged between the material of the sub-control volume and the surroundings. The initial material temperature distributions of pulse tube T_{m,pt_0} and regenerator T_{m,reg_0}, calculated with Eq. (2.142) and (2.143), are shown below the components.

The numbers of sub-control volumes n can differ for both components. The situation is shown in Fig. 2.13 (a, b). Each sub-control volume has the initial material temperature $T_{m,i}\big|_{t_0}$, which can be expressed for the pulse tube by

$$T_{m,pt,i}\big|_{t=t_0} = T_c + \frac{i}{n+1}\left(T_h - T_c\right), \qquad (2.142)$$

and for the regenerator by

$$T_{m,reg,i}\big|_{t=t_0} = T_h - \frac{i}{n+1}\left(T_h - T_c\right). \qquad (2.143)$$

The initial temperature distributions are symmetric to the hot heat exchanger.

For each sub-control volume of pulse tube and regenerator the pressure is calculated with

$$\frac{dp_i}{dt} = \frac{R_s\,T_i}{V/n}\left(\dot{m}_i' - \dot{m}_i''\right) + \frac{p_i}{T_i}\frac{dT_i}{dt}\,. \qquad (2.144)$$

In the pulse tube the pressure drop, in general, is negligible. Since the regenerator has got a dense porous structure [71, 72], having the porosity $e = V/(V + V_m)$, the pressure drop is not negligible.

The gas and material temperature of the sub-control volumes are calculated according to

$$\frac{c_v \, p_i \, V/n}{R_s \, T} \frac{dT_i}{dt} = -c_v \, T_i \left(\dot{m}_i' - \dot{m}_i'' \right) + \dot{Q}_{hx,i} + \dot{Q}_{cg,i}' - \dot{Q}_{cg,i}'' + \dot{m}_i' \, c_p \, T_i' - \dot{m}_i'' c_p \, T_i''$$
(2.145)

and

$$\rho_m \, V_m/n \, c_m \frac{dT_{m,i}}{dt} = -\dot{Q}_{hx,i} + \dot{Q}_{cm,i}' - \dot{Q}_{cm,i}'' + \dot{Q}_{ext,pt/reg,i} \, .$$
(2.146)

For both components the temporal change of the respective sub-control volume mass flux $\dot{m}_i$ is calculated with

$$\frac{d\dot{m}_i}{dt} = \frac{R_s}{V/n} \left(\frac{\dot{m}_i'^2 \, T_i'}{p_i'} - \frac{\dot{m}_i''^2 \, T_i''}{p_i''} \right) + \frac{A_f^2}{V/n} \left(p_i' - p_i'' \right) - \frac{2 \, f_f \, R_s \, T_i \, \dot{m}_i \, |\dot{m}_i|}{p_i \, A_f \, d_h} \, .$$
(2.147)

Control volume linkage

Linking two control volumes A and B is achieved by exchanging mass and energy. The situation is illustrated in Fig. 2.14 (a). All fluxes add up to $\dot{m}_A'' + \dot{m}_B' = 0$, $\dot{Q}_{c_A}'' + \dot{Q}_{c_B}' = 0$ and $\dot{H}_A'' + \dot{H}_B' = 0$, while the pressures are processed with the equations for the temporal change of the mass fluxes — Eq. (2.137) for the cylinder, Eq. (2.141) for the heat exchangers, and Eq. (2.147) for the pulse tube and regenerator. In order to determine

(a) Control volume linkage   (b) Smoothing function
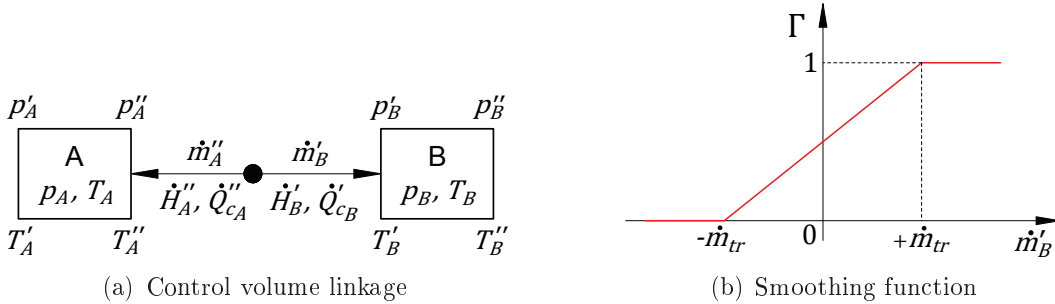
Figure 2.14: (a) Linkage of two control volumes A and B. All fluxes add up while the pressures are processed with the equation for the temporal change of the mass flux for each control volume; (b) Visualization of the smoothing function according to Eq. (2.148) to handle numerical instabilities caused by changes of the enthalpy flux direction.

the magnitude of the enthalpy fluxes $\dot{H}'$ and $\dot{H}''$ the following consideration according to the upwind method [73] is made: When the mass $m_A'' = m_B'$ flows from control volume A to control volume B it carries the enthalpy $H_A'' = m_A'' \, c_p \, T_A'' = m_B' \, c_p \, T_A'' = H_B'$ from control volume A to control volume B and vice versa. Depending on the direction of the mass flux, the temperature to calculate the enthalpy flux has to be altered between the boundary temperatures of control volume A and B.

To handle numerical instabilities resulting from the switching process, the temperature for calculating the enthalpy flux is modified to $T^* = \Gamma \, T_A'' + (1 - \Gamma) \, T_B'$, where the smoothing function according to Fig. 2.14 (b)

$$\Gamma = \begin{cases} 1 \, , & \dot{m}_B' > \dot{m}_{tr} \\ \frac{\dot{m}_B'}{2\,\dot{m}_{tr}} + \frac{1}{2} \, , & -\dot{m}_{tr} \leq \dot{m}_B' \leq \dot{m}_{tr} \\ 0 \, , & \dot{m}_B' < -\dot{m}_{tr} \end{cases} \tag{2.148}$$

with the threshold value $\dot{m}_{tr}$ for the mass flux is introduced. Thus, the enthalpy fluxes are calculated with $\dot{H}_A'' = \dot{m}_A'' \, c_p \, T^* = -\dot{H}_B' = -\dot{m}_B' \, c_p \, T^*$.

Initial conditions

Initially the cylinder and the two cold heat exchangers have a gas and material temperature equal to T_c, whereas the hot heat exchanger has a gas and material temperature equal to T_h. At the beginning, the material temperature distributions of the pulse and the regenerator are given by Eq. (2.142) and (2.143), and the gas temperature distributions are equal to the respective material temperature distribution.

Heat transfer, heat conduction and flow friction

The calculations of the heat fluxes $\dot{Q}_{hx}$ between the working gas and the material, as well as of the conductive heat fluxes $\dot{Q}_{cg}$ and $\dot{Q}_{cm}$ in the gas and the material, and the calculation of the flow friction factor are performed for the specific engine.

The numerical model has two remaining free parameters which have to be quantified. These are the engine's dead volume V_0, which is assigned to the cylinder volume, and the starting position of the piston ϕ in degree of crank angle relative to TDC at which the pressure is equal to the engine filling pressure p_f. Both parameters shall be determined experimentally.

2.7.2 Calculation of the cycle power and transferred heat

In this subsection the techniques finalizing the numerical calculation are presented.

The system of differential equations is implemented within the object-oriented programming language Modelica and solved numerically using the software SimulationX. As a result, the dynamical state variables of the pulse tube engine such as the gas temperatures $\{T_{cyl}(t), T_{chx_1}(t), T_{pt}(x,t), T_{hhx}(t), T_{reg}(x,t), T_{chx_2}(t)\}$ are obtained. The

cycle energy fluxes $\dot{E}_{cyc}$ are calculated by integrating the energy fluxes $\dot{E}$ over one engine cycle and multiplying the results with the operating frequency f. As an example, the cycle heat flux of a component and the net cycle power are calculated with $\dot{Q}_{cyc} = f \oint \dot{Q}\, dt$ and $P_n = f \oint \dot{W}\, dt$. All heat fluxes, calculated for each sub-control volume of the pulse tube or the regenerator, are added to a total heat flux $\dot{Q}_t = \sum_{i=1}^{n} \dot{Q}_i$ of the entire component.

The calculations are performed with minimum and maximum permissible time increments of $\Delta t_{min} = 10^{-8}\,\mathrm{s}$ and $\Delta t_{max} = 10^{-5}\,\mathrm{s}$, respectively. For all calculations a sufficient number of engine cycles is calculated until the changes from cycle to cycle are negligible. The values of $\dot{Q}_{cyc}$ and P_n are averaged over the last ten cycles calculated.

The numerical model predicts the net power output of the engine, which is delivered to the piston. The ideal cycle power output − denoted with gross power output P_g − is the power output of the thermodynamic cycle which does not take into account internal power losses $P_{l,int}$ due to heat transfer, heat conduction and flow friction. The net and the gross power output are related through

$$P_n = P_g + P_{l,int}. \tag{2.149}$$

The numerical model allows to switch off heat conduction and flow friction, but the heat transfer constraints remain. The gross power output can thus only be estimated by the model.

To get the shaft power output P_{sh}, the net power has to be reduced by an amount equaling the power losses $P_{l,ext}$ due to solid body friction in the cylinder, the bearings and the crank mechanism. The shaft power output can then be calculated from

$$P_{sh} = P_n + P_{l,ext}. \tag{2.150}$$

The sign convention is that all power outputs have a negative and all power losses a positive sign.

2.8 Simplified numerical model

In order to find general dependencies and to facilitate the numerical computation, the numerical model derived in section 2.7 is simplified. The simplified model is validated and shall be used to calculate the thermodynamic cycle of the pulse tube engine.

2.8.1 Model simplifications

The following simplifications are made:

1) The pressure is regarded as uniform throughout the entire machine. The equations for the temporal change of the mass fluxes, Eq. (2.137), (2.141) and (2.147), do not have to be solved. The pressure drop due to flow friction is calculated afterwards.

2) All internal power losses $P_{l,int}$ due to heat transfer, heat conduction in the gas and flow friction as well as all external power losses $P_{l,ext}$ due to mechanical friction are calculated separately (see subsection 2.8.2), and are used to calculate the net power output with Eq. (2.149) and the shaft power output with Eq. (2.150). Material heat conduction is not considered, thus $\dot{Q}'_{cm} = \dot{Q}''_{cm} = 0$.

3) The material temperature is time-invariant, and Eq. (2.136), (2.140) and (2.146) simplify to

$$\dot{Q}_{ext} = \dot{Q}_{hx}\,.$$

No material temperature equilibrium has to be achieved and the necessary number of cycles to be calculated is reduced. For all calculations, the number is set to 50.

4) The heat exchangers are ideal, i.e. the working gas takes on the locally prevailing material temperature and exits the heat exchanger with this temperature (ideal isothermal behavior). Hence, Eq. (2.139) simplifies to

$$0 = -c_v\,T\,(\dot{m}' - \dot{m}'') + \dot{Q}_{hx} + \dot{m}'\,c_p\,T' - \dot{m}''\,c_p\,T''\,.$$

5) The thermal contact between the working gas and the material of the regenerator is ideal, so that the gas temperature distribution is the same as that of the regenerator material (ideal isothermal behavior). Thus, for the regenerator Eq. (2.145) simplifies to

$$0 = -c_v\,T_i\,(\dot{m}'_i - \dot{m}''_i) + \dot{Q}_{hx,i} + \dot{m}'_i\,c_p\,T'_i - \dot{m}''_i\,c_p\,T''_i\,.$$

6) For the cylinder and the pulse tube, the heat transfer coefficient α and the heat exchange area A_{hx} are combined to a heat transfer capacity $\gamma := \alpha\,A_{hx}$, which is time- and space-invariant in the pulse tube, but varies sinusoidally with volume in the cylinder.

Since pulse tube and regenerator consist of a number of sub-control volumes n_{pt} and n_{reg}, the dependency of the solution on n_{pt} and n_{reg} is investigated. For all calculations both values are set to $n_{pt} = n_{reg} = n$.

Fig. 2.15 shows the integrated cycle values of the pV-work as well as of the transferred heat in the pulse tube and in the regenerator as functions of the number of sub-control volumes. The calculations are performed for a representative test engine of $100\,\mathrm{cm}^3$ displacement volume, filled with air (pressure: $100\,\mathrm{kPa}$ at BDC), having an operating frequency of $5\,\mathrm{Hz}$ and minimum/maximum temperatures of $T_c = 27\,^\circ\mathrm{C}$ and $T_h = 327\,^\circ\mathrm{C}$. No internal or external power losses occur. The cylinder is regarded as adiabatic ($\gamma_{pt} = 0$) and the heat transfer capacity of the pulse tube is set to $\gamma_{pt} = 0.2\,\mathrm{W/K}$. The maximum order of magnitude of the mass fluxes is $1\,\mathrm{g/s}$. The threshold value in the smoothing function (2.148) is set by two orders of magnitude lower to a value of $\dot{m}_{tr} = 10\,\mathrm{mg/s}$.
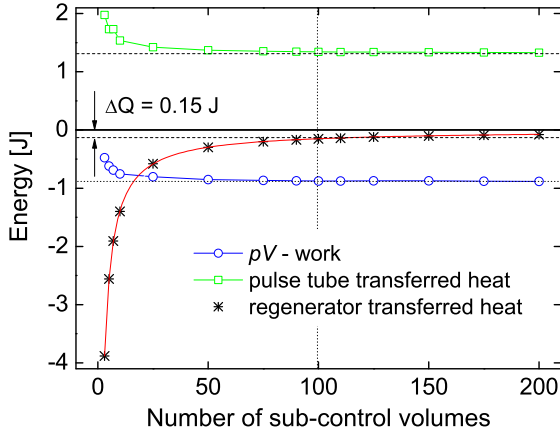
Figure 2.15: Influence of the number of sub-control volumes on the accuracy of the numerical solution. For this investigation, the number of sub-control volumes of the pulse tube n_{pt} and of the regenerator n_{reg} is set to $n_{pt} = n_{reg} = n$.

Therefore, its influence on the solution is small. The dependency of all energy values on the number of sub-control volumes is clearly evident. For high values of n the results converge towards threshold values. The amount of heat transferred per cycle in the regenerator has the highest dependency on n. Its values are adapted with the function $Q_{reg}(n) = (c_h + c_k\,n)^{-1}$, since the amount of heat transferred per cycle of an ideal regenerator (compare Eq. (2.83) in subsection 2.3.4) is equal to zero. From Fig. 2.15 can be concluded, that a preferably large number of sub-control volumes should be selected. This results in a high computational demand. Following standard practice in technology, a compromise between accuracy and effort is chosen. For all calculations the number of sub-control volumes is set to $n = 100$. Choosing this value the inaccuracy of the calculated amount of heat transferred per cycle in the regenerator is $0.15\,\mathrm{J}$ which is about 1% of the regenerator's stored heat of $14.9\,\mathrm{J}$ during compression.

With the defined discretizations of pulse tube and regenerator of $n = 100$ and the maximum permissible time increment of $\Delta t_{max} = 10^{-5}\,\mathrm{s}$ the numerical simulation model enables to calculate a number of 50 engine cycles in about 5 hours on a regular state of the art personal computer. It thus can be used to perform parametric studies of the engine within a reasonable calculation time.

2.8.2 Modeling of power losses

The power output of the engine is reduced by power losses. Simplified approaches used to calculate internal and external power losses are as follows.

In the heat exchangers the transferred heat is calculated using fixed heat exchanger temperatures. Thus, only heat conduction through the gas has an influence on the cycle power. Both, the conductive heat flux through the pulse tube and through the regenerator are globally calculated with $\dot{Q}_{cg} = \lambda_g\, A_f\, (T_h - T_c)/L$, where λ_g is the mean heat conductivity of the working fluid, A_f the free flow area, and L the length of the regarded component. The resulting power loss due to heat conduction via the working gas is obtained by multiplying the conductive heat fluxes by the engine's thermal efficiency η_{th}

$$P_{l,cd} \;=\; \eta_{th}\left(\dot{Q}_{cg,pt} \,+\, \dot{Q}_{cg,reg}\right). \tag{2.151}$$

Imperfect heat transfer in the heat exchangers can be considered using a heat exchanger efficiency $\eta_{hx} = \dot{Q}_{hx,re}/\dot{Q}_{hx,id}$, where $\dot{Q}_{hx,id}$ and $\dot{Q}_{hx,re}$ are the maximal possible (ideal) and the real heat flux, respectively. Typical values for heat exchangers can be found in [74]. Due to their high heat transfer area, in general, regenerators have very high values of $\eta_{hx} > 0.99$ [61, 71]. Thus, the regenerator's heat transfer loss is negligible. To quantify the influence of the heat exchanger efficiency, the global energy balance on the entire engine is used. The gross power of the ideal cycle is given by $P_{b,id} = -\sum_i \dot{Q}_{hx,id,i}$. With the heat exchanger efficiency the gross power of the real cycle is given by $P_{b,re} = -\sum_i \dot{Q}_{hx,re,i} = -\eta_{hx}\sum_i \dot{Q}_{hx,id,i}$. Thus, the power loss due to imperfect heat transfer in the heat exchangers amounts to

$$P_{l,hx} \;=\; |P_{b,id} \,-\, P_{b,re}| \;=\; (1 \,-\, \eta_{hx})\,|P_{b,id}| \,. \tag{2.152}$$

The friction force resulting from the mass fluxes $\dot{m}$ flowing through the heat exchangers and the regenerator leads to the power loss due to gas friction represented by

$$P_{l,fg} \;=\; f \oint \frac{2\,f_f\,|\dot{m}^3|\,L}{\rho^2\,A_f^2\,d_h}\,dt\,. \tag{2.153}$$

The mass flow rate and the gas density are results of the flow-friction-less transient simulation. Since the flow paths in the heat exchangers are tight, the value of the Reynolds number $Re \propto d_h$ is small and the friction factor in the heat exchangers can be expressed by $f_f(Re) = 16/Re$, which is valid for laminar flows. Assuming that the regenerator is made of stacked wire mesh screens with the porosity e, the friction factor $f_f(Re,e)$ can be calculated using experimental data from [58]. The data for $f_f(Re,e)$, given in [58], are obtained from steady-state flow measurements. The induced modeling

error is judged to be of minor importance.

The total internal power loss is calculated with

$$P_{l,int} = P_{l,cd} + P_{l,hx} + P_{l,fg}. \tag{2.154}$$

To get the shaft power, the net power has to be reduced by external power losses (solid body friction) in the cylinder and the crank mechanism. These power losses are calculated from the friction force between the piston and the cylinder F_f^{cyl} as well as the friction momentums M_f^{sh} in the connecting rod and the crank shaft bearings. The resulting power loss due to solid body friction is

$$P_{l,ext} = f \oint \left(|F_f^{cyl} u_p| + \sum_i |M_{f,i}^{sh} \nu_i| \right) dt \,, \tag{2.155}$$

with the piston velocity u_p and the angular velocity ν_i of the respective bearing i.

2.8.3 Model validation

To use the simulation model for numerical investigations of the pulse tube engine its results have to be validated.

The validation is done using the measured performance of an atmospheric pulse tube engine with air as working fluid. The experimental results of this "Reference engine" are reported in [23]. For all investigations the parameters given in Table 2.1 according to the pulse tube engine reported in [23], page 6 to 11, are used.

The threshold value in the smoothing function, Eq. (2.148), is set to $\dot{m}_{tr} = 10\,\mathrm{mg/s}$. The working fluid is air, which is regarded as a perfect gas. The temperature T_{m,chx_1} was obtained directly from the author of [23]. The temperatures T_{m,chx_2} and $T_{m,hhx}$ are taken from [23], page 10, Fig. 14, measured at an operating frequency of 2.5 Hz. Nevertheless, these temperatures are used for all frequencies. The heat transfer capacities of pulse tube and cylinder are estimated using heat transfer correlations from [75]. The mean heat conductivity of the working fluid air is $0.035\,\mathrm{W/(m\,K)}$.

Since the hot heat exchanger is part of the regenerator and chx$_2$ is a solid block of aluminum, their dead volumes are zero. In contrast to that, the remaining dead volumes of the cylinder and chx$_1$ are unknown and need to be determined. To do so, the dead volume V_0 is assigned completely to the cylinder while the dead volume of chx$_1$ is considered to be zero. The error of this approach is small, because the time-averaged temperatures in both components have similar values. For an operating frequency of 5 Hz the dead volume V_0 and the filling pressure p_f at BDC are varied to meet the measured minimal pressure of $p_{min} = 87.1\,\mathrm{kPa}$ and the measured pressure amplitude

Table 2.1: Operating conditions and design parameters of the Reference engine [23]

Parameter	Symbol	Value
Material temperature hhx	$T_{m,hhx}$	332 °C
Material temperature chx$_1$	T_{m,chx_1}	35 °C
Material temperature chx$_2$	T_{m,chx_2}	51 °C
Ambient pressure	p_a	101.325 kPa
Filling pressure at BDC	p_f	88.4 kPa
Minimum pressure	p_{min}	87.1 kPa
Pressure amplitude	$\hat{p}$	28.4 kPa
Cylinder bore	b	27.6 mm
Piston stroke	s	60.0 mm
Crank ratio	r_{cr}	2
Pulse tube diameter	d_{pt}	27.2 mm
Pulse tube length	L_{pt}	73.5 mm
Regenerator diameter	d_{reg}	27.2 mm
Regenerator length	L_{reg}	91.0 mm
Mesh number	n_m	50
Wire diameter	d_w	193 μm
Porosity	e	0.762
Displacement volume	V_d	35.90 cm^3
Dead volume	V_0	48.00 cm^3
Pulse tube volume	V_{pt}	42.71 cm^3
Regenerator volume	V_{reg}	40.29 cm^3
Heat transf. cap. cylinder	γ_{cyl}	0.16 W/K
Heat transf. cap. pulse tube	γ_{pt}	0.19 W/K

of $\Delta p = 28.4$ kPa according to [23], page 10, Fig. 13. The results are $V_0 = 48$ cm^3 and $p_f = 88.4$ kPa, respectively. The found high value of the dead volume could be a result of leakage occurring in the engine, which lowers the pressure swing intensity. In this case V_0 represents a combination of the real unknown dead volume and virtual dead volume due to leakage.

Excluding the dead volume, the compression ratio of the Reference engine is $r_c = 0.43$ and the distribution ratio is $r_d = 0.94$. The mean diameter of all bearings is assumed to be $d_b = 5$ mm and the solid body friction factor (steel–steel, lubricated) is $f_s = 0.01$.

In Fig. 2.16 the calculated pressure and the cylinder volume displacement for one engine cycle at an operating frequency of 5 Hz are shown. The ambient pressure of $p_a = 101.325$ kPa (standard conditions at sea level) is reached at about 75 deg before TDC. Initializing the engine process with ambient pressure at about 85 deg before TDC leads to similar results. Thus, in the experiment, the engine was started around this position of the piston. The phase difference between TDC and maximum pressure is 1.96 deg. The measured value given in [23], page 10, is 2.28 deg. The mismatch is 14%.
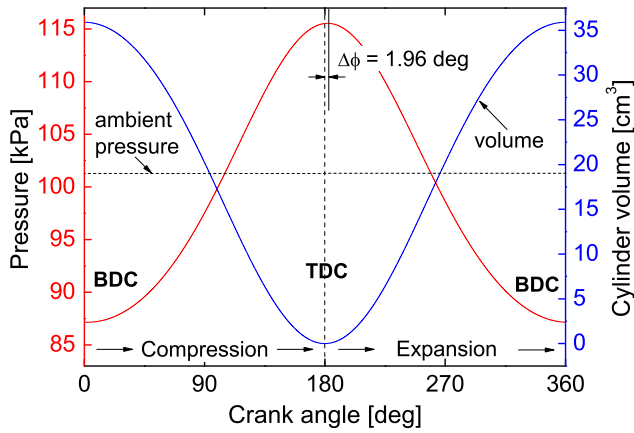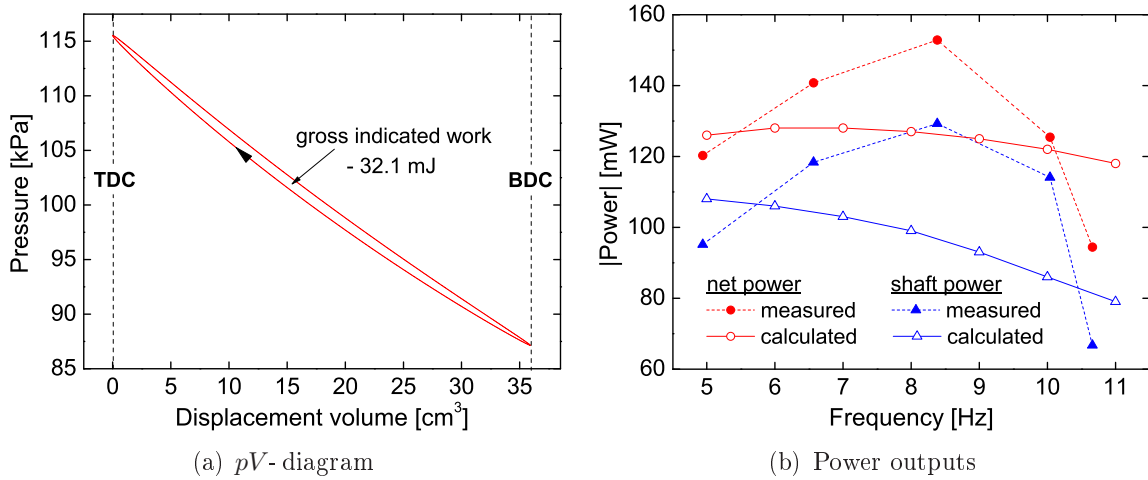
Figure 2.16: Calculated pressure and cylinder volume displacement of the Reference engine according to [23] as functions of the crank angle.

Fig. 2.17 (a) shows the resulting pV-diagram of the engine. It differs in the piston's dead points strongly from the assumed thermal relaxation at constant volume, shown for instance in Fig. 2.8. Thus, the thermal relaxation is not bound to the dead points. In reality it is occurring in all phases of the cycle with emphasis around BDC and TDC. The enclosed area in Fig. 2.17 (a) represents the gross indicated work (pV-work), which amounts to -32.1 mJ. This value can only be reached under ideal conditions. In the real engine the shape of the pressure curve is significantly influenced by loss mechanisms such as heat conduction, heat transfer losses and pressure drop (see subsection 2.8.2). The last one mainly occurs in the regenerator. Taking the mentioned energy dissipations of about 6.8 mJ into account, the net indicated work amounts to -25.2 mJ. The measured value in [23], page 8, is -24.4 mJ. The difference amounts to 3.5%. The estimated work dissipation due to solid body friction in the cylinder and the crank mechanism is 2.6 mJ. The resulting shaft work is -21.6 mJ. In [23], page 10, Fig. 11, a measured value of -19 mJ is reported. The mismatch of about 14%, compared to the good match of the net indicated work is due to the high uncertainly of the calculated solid body friction loss.

In Fig. 2.17 (b) the frequency dependencies of the absolute values of the calculated net indicated power P_n and the calculated shaft power P_{sh} are compared with the measured values of [23], page 10, Fig. 11. The order of magnitude of both calculated power outputs is in good agreement with the measurements. The property of a maximum value for a certain frequency is clearly evident for measurement and calculation. Compared to the calculated values, the measured power outputs have a much stronger dependency on the operating frequency. This is caused by several factors. The strong increase of the measured power outputs for an increasing operating frequency between 5 Hz and 8 Hz could be a result of lower leakage due to higher gap flow friction of the gas leaking through the gap between piston and cylinder. Therefore, for higher frequencies, the engine probably gets sealed better. The heat exchanger temperatures, the minimum pressure and the pressure amplitude are taken from measurements at low operating frequencies and used for the calculations at higher frequencies. Thus, the

(a) pV-diagram   (b) Power outputs

Figure 2.17: (a) Calculated pV-diagram of the Reference engine according to [23]; (b) Comparison of the calculated and measured net and shaft power outputs of the Reference engine according to [23].

real pressure curve and the transferred heat for higher operating frequencies can not be clearly reproduced by the model. Moreover, the loss mechanisms — in reality — interact. A pressure drop in the regenerator reduces the mass flux and thus, reduces the transferred heat per time. This reduces the power output stronger than calculated.

2.9 Results of the simplified numerical model

After the successful validation, the numerical simulation model can now be applied to calculate the engine cycle under variation of design parameters and operating conditions, and to study the engine performance predicted by the analytical model in section 2.5 in more detail. It will be used to investigate the engine behavior under variation of the heat input temperature, the compression ratio, the distribution ratio and the heat transfer conditions in the pulse tube. The results will help to find optimal design parameters for maximum power output and efficiency.

2.9.1 The pulse tube engine process

The previously validated simulation model is used to calculate the pulse tube engine process at an operating frequency of 5 Hz. At this frequency the modeling error is smaller than 15%. Referring to Fig. 2.16 two results are evident. First, the working gas pressure falls during the second phase of the expansion below ambient pressure. Thus, the surrounding air is able to carry out work on the system due to the resulting pressure force on the piston. This slows down the second phase of the expansion while assisting

the first phase of the compression, which provides for a free piston operation of the engine [76]. Second, the positive phase delay of 1.96 deg between maximum pressure and TDC results in a slightly higher expansion pressure than compression pressure and is therefore responsible for a release of work.
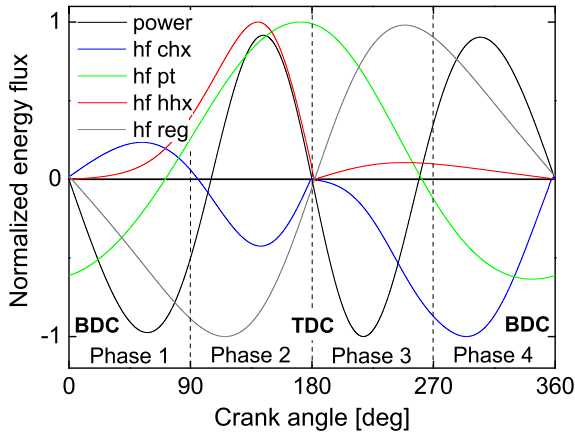
Figure 2.18: Calculated energy fluxes of the Reference engine [23] components as functions of the crank angle. The values are normalized to their respective maxima. power: compression/exp. power difference, hf chx: heat flux in chx_1, hf pt: heat flux in the pulse tube, hf hhx: heat flux in hhx, hf reg: heat flux in the regenerator.

Fig. 2.18 shows the total energy fluxes (see subsection 2.7.2 for their definition) occurring in the components of the engine as well as the compression/expansion power difference, which is calculated from the pressure difference between the engine pressure and the ambient pressure (piston's rear side) during each phase of the cycle. The shaft power is proportional to the calculated compression/expansion power difference. The operating conditions are the same as in Fig. 2.16. The energy fluxes are normalized to their absolute maxima. A positive sign means that the energy flux is added to the working gas. In phase 1 and 2 the piston moves from BDC to TDC, resulting in a compression of the working gas. During phase 3 and 4 the piston moves from TDC to BDC, which results in an expansion of the working gas. Therefore the engine cycle can be described as follows:

Phase 1: Compression

Since the ambient pressure is higher than the engine pressure, the ambient air pushes the piston in the direction of TDC, which is associated with a shaft power output provided by the ambient air. The working gas is compressed. Simultaneously, it receives heat from the cold heat exchanger 1 (hf chx), located between the cylinder and the pulse tube. Therefore it must have gone below T_{m,chx_1} during the previous expansion process. A heat input by the hot heat exchanger (hf hhx) starts at about mid-phase. Within the pulse tube the direction of the heat flux (hf pt) changes from heat output to heat input. The regenerator material absorbs heat (hf reg).

Phase 2: Compression

At the beginning of this phase the ambient air is still providing a shaft power output. At about 100 deg after BDC the engine pressure exceeds the ambient pressure and compression power has to be delivered to the shaft in order to further compress the working gas. Within this phase, the direction of the heat flux in the cold heat exchanger 1 reverses and the compressed gas is cooled on its way to the pulse tube. In the pulse tube and the hot heat exchanger, an enforced addition of heat to the working gas takes place. The regenerator material still absorbs heat.

Phase 3: Expansion

For the majority of this phase the engine pressure is higher than the ambient pressure. The working gas is expanding and pushes the piston in the direction of BDC, accompanied by a shaft power output provided by the working gas. At about 80 deg after TDC the engine pressure falls below the ambient pressure and expansion power has to be delivered to the shaft in order to continue the expansion of the working gas. The regenerator material gives off heat. The heat flux in the hot heat exchanger comes to an almost complete standstill since the small temperature difference between the working gas — coming from the regenerator — and the heat exchanger material allows for almost no heat to be supplied to the gas. Within the pulse tube the direction of the heat flux changes from heat input to heat output. The cold heat exchanger withdraws heat from the working gas on its way to the cylinder.

Phase 4: Expansion

To further expand the working gas, expansion power has to be delivered to the shaft. The regenerator material still gives off heat and the heat flux in the hot heat exchanger is still almost zero. In the pulse tube heat emission takes place and the cold heat exchanger keeps withdrawing heat from the gas.

If the absolute amount of energy added to the shaft is smaller than the absolute amount of energy released from the shaft, the engine acts as a prime mover. For the compression of the working gas in Phase 2 and the expansion of the working gas in Phase 4 energy has to be stored in a flywheel or any other mechanism. In the case of a free piston engine, this can be the kinetic energy of the piston.

2.9.2   Influence of the compression ratio

In this subsection the influence of the compression ratio on the pulse tube engine performance is studied numerically and compared to the predictions of the analytical model.

(a) Influence of the compression ratio   (b) Influence of the distribution ratio
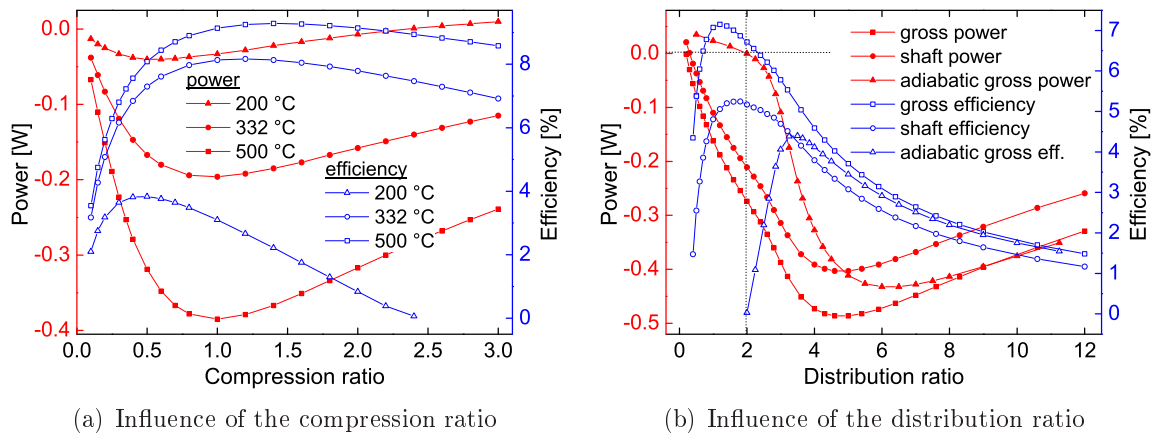
Figure 2.19: (a) Gross power output and efficiency as functions of the compression ratio of the modified Reference engine [23] for heat input temperatures of $200\,°C$, $332\,°C$ and $500\,°C$; (b) Gross and shaft power output and efficiency as functions of the distribution ratio of the modified Reference engine [23]. The cycle is also calculated for an adiabatic pulse tube.

The displacement volume and the dead volume are fixed at the values given in Table 2.1. The distribution ratio is kept at $r_d = 0.94$, whereas the sum of pulse tube and regenerator volume is varied. The engine is filled with ambient air ($p_a = 101.325\,\text{kPa}$) at $85\,\text{deg}$ before TDC and runs at an operating frequency of $5\,\text{Hz}$. In Fig. 2.19 (a) the calculated relationships between the compression ratio and the gross power as well as between the compression ratio and gross efficiency are shown. The engine process is calculated for three temperatures of the hot heat exchanger, which are $T_h = 332\,°C$ from Table 2.1 as well as $T_h = 200\,°C$ and $T_h = 500\,°C$. It can be seen, that the performance of the engine strongly depends on the compression ratio. Optimal values exist for the gross power and the gross efficiency. With increasing hot heat exchanger temperatures the absolute peak values of the gross power and efficiency are higher at higher compression ratios. Turning this result around leads to the conclusion that for a free piston engine − having a variable stroke − the amplitude of the piston oscillation increases with an increase of the hot heat exchanger temperature.

The engine provides a gross power output even for $T_h = 200\,°C$, which indeed is too small to provide a significant shaft power output. Together with the distribution ratio of the Reference engine ($r_d = 0.94$), the minimum necessary hot heat exchanger temperature, predicted by the analytical model with Eq. (2.81), results in $363\,°C$, which is not observed in this numerical study. The reason could be the insufficient information about the exact design of the Reference engine.

The highest gross efficiency is reached at higher compression ratios than the highest gross power. The difference between both peaks increases with an increase of the temperature. For $T_h = 200\,°C$ the difference is nearly zero, for $T_h = 332\,°C$ it amounts

to 0.2 and for $T_h = 500\,°\mathrm{C}$ to 0.4. In the case of $T_h = 332\,°\mathrm{C}$, the highest gross power output of about $-0.2\,\mathrm{W}$ is reached at a compression ratio of $r_c = 0.9$ and the highest gross efficiency of about 8.2% is reached at a compression ratio of $r_c = 1.1$. Hence, the supposed existence of a peak value around $r_c = 1$ in section 2.6 is proven. Moreover, according to Fig. 2.19 (a) the gross power becomes zero for $r_c = 0$ and positive for $r_c \to \infty$. The relation for the gross power Eq. (2.111) in combination with Eq. (2.110) and (2.116), derived with the analytical model, does not show this behavior.

To introduce the numerically observed dependency on r_c, the linear component of the pV- work Eq. (2.110) is multiplied with a function $F(r_c)$ having the properties

$$
\begin{array}{llll}
1. & F|_{r_c=0} & = & 0\,, \\[2mm]
2. & \lim\limits_{r_c \to \infty} F & < & 0\,, \\[2mm]
3. & \left.\dfrac{dF}{dr_c}\right|_{r_{c,opt}} & = & 0 \quad \text{and} \\[2mm]
4. & \left.\dfrac{d^2 F}{dr_c^2}\right|_{r_{c,opt}} & < & 0\,.
\end{array}
\tag{2.156}
$$

Thus, the linear component of the pV- work becomes

$$
W_{pV_l}^* = F(r_c)\, p_{min}\, V_d\, \frac{r_d\,(\tau - 1) - 1}{(r_d + 1)^2}\,,
\tag{2.157}
$$

and the averaged pV- work of Eq. (2.111) results in

$$
W_{pV}^* \approx - F(r_c)\, p_{min}\, V_d\, \frac{r_d\,(\tau - 1) - 1}{(r_d + 1)^2}\,(1 + \chi_{pV})\,.
\tag{2.158}
$$

The slight dependency of the compression ratio, which maximizes the pV- power, on the temperature ratio − also visible in Fig. 2.19 (a) − is due to the dependency of χ_{pV} on the temperature ratio.

Since the linear component of the pV- work is modified with the function $F(r_c)$, all quantities, presented in subsection 2.3.6, for the amount of heat transferred per cycle and the entropy production have to be calculated with Eq. (2.157) instead of Eq. (2.110).

The physical meaning of the function $F(r_c)$ is that at very low compression ratios the engine does not provide a significant power output, because the pressure difference between compression and expansion is too small. In Fig. 2.19 (a), the observed increase of the engine performance up to the optimal compression ratio results from an increasing mass flux passing the heat exchangers. The transferred heat and thus the converted thermal energy into expansion work increases. On the other hand, the slope of the

transferred heat decreases. This is caused by the stronger temperature rise during compression, which lowers the temperature difference between the hot heat exchanger and the working gas. For this reason, the optimal compression ratio increases for higher temperatures of the hot heat exchanger.

At higher compression ratios, the pressure rises stronger and heat is added to the working gas at a higher pressure. Additionally, for lower temperature differences, the entropy production due to heat transfer decreases. This increases the efficiency and is responsible for the higher value of the compression ratio, which maximizes the efficiency compared to the value of the compression ratio at maximum power output. The highest efficiency is reached when the compression end temperature equals the heat input temperature. Due to the resulting lower amount of transferred heat, the power decreases already at lower compression ratios.

At very high compression ratios the temperature rise during compression is too strong, which leads to a lower amount of heat transferred to the working gas passing the hot heat exchanger. Hence, the energy converted into expansion work decreases and leads to a not-functioning engine.

2.9.3   Influence of the distribution ratio

The importance of the distribution ratio became already obvious through the predictions of the analytical model. Its influence on the engine performance is now studied numerically.

To explore the effect of the distribution ratio, the sum of the pulse tube and regenerator volume is kept at the constant value $V_{pt} + V_{reg} = 83\,\mathrm{cm}^3$. The distribution ratio is varied between 0.2 and 12 while fixing the lengths and varying the diameters of pulse tube and regenerator. All other dimensions and operating conditions are kept at the values given in Table 2.1. The operating frequency is $5\,\mathrm{Hz}$.

Fig. 2.19 (b) shows the gross and shaft power as well as the gross and shaft efficiency of the engine depending on the distribution ratio. All values have a strong dependency on the distribution ratio and come to zero for $r_d \to \infty$. For very small distribution ratios the engine does not provide a power output. The efficiency has its maximum between $r_d = 1.2$ (gross power) and $r_d = 1.7$ (shaft power). The maximum gross and shaft power are both obtained at $r_d = 4.7$, which can be regarded as a limit of optimal operation. The value of $r_d = 0.94$ used in [23] is therefore far from the optimal value for maximum power output. The analytical model predicts with Eq. (2.131) a value, maximizing the pV- work, of $r_{d,opt} = 3.1$.

In [31], page 1268 to 1270, a pulse tube engine is presented which has the same regenerator volume as the one presented in [23], but a 22% lower pulse tube volume.

The distribution ratio is $r_d = 1.21$ and thus, according to Fig. 2.19 (b), in the range of the highest efficiency. The measured shaft power is about 50% higher than the shaft power of the engine presented in [23]. Changing the distribution ratio from $r_d = 0.94$ to $r_d = 1.21$, the numerical model predicts a shaft power improvement of only 36%. The mismatch compared to the experimental observation is due to the increased compression ratio of the engine in [31], which was increased from $r_c = 0.43$ to $r_c = 0.47$. This results according to Fig. 2.19 (a) in an additional increase of the power output of about 12%.

Moreover, in [31], page 1272 to 1275, is reported, that additional heat storage material (stacked wire mesh screens: 5 mesh/inch, 36 mm in length), placed at the hot side of the pulse tube, increases the power output of the engine dramatically at about 2.7 times compared to the version without the additional heat storage material. The created additional heat storage gas volume amounts to about $18 \, \mathrm{cm}^3$. Regarding this additional heat storage gas volume as part of the regenerator, the distribution ratio is increased from $r_d = 1.21$ to $r_d = 4.5$. The numerically calculated ideal value is $r_d = 4.7$! Using the results of Fig. 2.19 (b), the model predicts an increase of the shaft power of about 2.9 times, which is 7.4% higher than the experimentally observed value. The difference is mainly due to the neglected opposite temperature distribution in the heat storage material placed at the hot side of the pulse tube.

The found dependency of the engine performance on the distribution ratio is caused by the working principle of the pulse tube engine, which is based on a broken thermodynamic symmetry between pulse tube and regenerator. Thermodynamic asymmetry is achieved by the set temperature distribution and the opposed heat transfer conditions in both components (compare to Fig. 1.2). At low distribution ratios the nearly adiabatic space (pulse tube) is large compared to the nearly isothermal space (regenerator). At high distribution ratios the inverse situation is present. In both cases the thermodynamic symmetry is only slightly broken. For the found distribution ratio at maximum gross efficiency, the thermodynamic asymmetry is below its maximum value due to the influence of the heat transfer in the pulse tube. The maximum gross power is reached for a three times larger regenerator space, which should have exceeded the maximum value of thermodynamic asymmetry. In this case the mass flux crossing the hot heat exchanger is higher, which increases the amount of heat transferred to the working gas and thus the heat converted into expansion work.

To find the distribution ratio which maximizes the thermodynamic asymmetry, the pulse tube is regarded as ideal adiabatic and the calculation of the process is repeated for distribution ratios between 0.2 and 12. The adiabatic gross power as well as the adiabatic gross efficiency are also shown in Fig. 2.19 (b). For values of $r_d < 2$, the adiabatic gross power is positive and the engine does not function. For values of $r_d > 2$,

the thermodynamic asymmetry is high enough that a sufficient amount of heat energy is converted into expansion work providing a power output. The maximum adiabatic gross efficiency is reached at $r_d = 3.4$. This value can be regarded as the distribution ratio which maximizes the thermodynamic asymmetry of the engine. For smaller distribution ratios the adiabatic gross efficiency comes to zero and converges for higher distribution ratios to the gross efficiency of the non-adiabatic case. The same happens with the adiabatic gross power, which has its maximum at $r_d = 6$ and converges for higher values to the gross power of the non-adiabatic case. The reason of this behavior is the decreasing amount of heat transferred in the pulse tube.

2.9.4   Heat transfer conditions in the pulse tube

In a last step the thermal interaction of the working gas and the pulse tube material is investigated with emphasis on the determination of the pulse tube engine's underlying thermodynamic working principle.

As discussed in Fig. 2.18, in a non-adiabatic pulse tube, heat is added to the working gas at the end of the compression stroke and is released from it at the end of the expansion stroke. This phenomena is called "thermal lag effect" [24, 26, 27, 28].
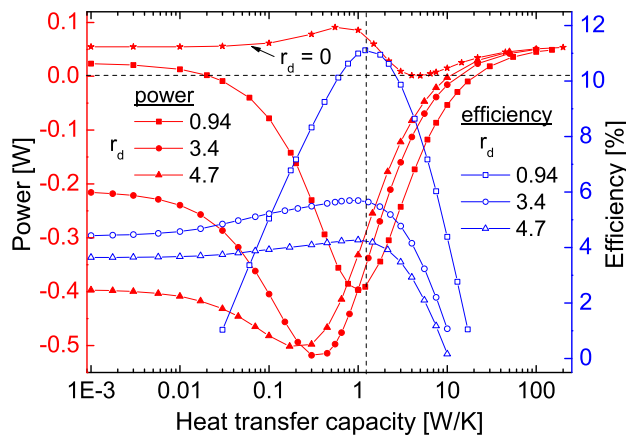
Figure 2.20: Gross power output and efficiency as functions of the heat transfer capacity $\gamma = \alpha\,A_{hx}$ of the pulse tube of the Reference engine [23]. The cycle is calculated for a pulse tube only ($r_d = 0$), for the distribution ratio of the unmodified Reference engine ($r_d = 0.94$), for a distribution ratio of $r_d = 3.4$ and for a distribution ratio of $r_d = 4.7$.

To study the influence of the thermal lag effect, the heat transfer capacity of the pulse tube is varied between adiabatic ($\gamma_{pt} = 1e^{-3}\,\mathrm{W/K}$) and isothermal ($\gamma_{pt} = 200\,\mathrm{W/K}$) conditions. The calculations are performed for the case of a pulse tube only ($r_d = 0$), which is equal to perfect thermodynamic symmetry, for the distribution ratio of [23] ($r_d = 0.94$), for a distribution ratio of $r_d = 3.4$, which is regarded as the configuration of maximum thermodynamic asymmetry and for a distribution ratio of $r_d = 4.7$.

Fig. 2.20 shows the calculated gross power outputs and gross efficiencies for all four cases. The engine does not produce any power output for a pulse tube only ($r_d = 0$, no regenerator). In contrast to the regenerator of the Stirling engine,

the regenerator of the pulse tube engine is essential for its functioning. This observation is in accordance with the predictions of the analytical model. As shown in Fig. 2.12 (a) — depending on the temperature ratio — a minimum value of $r_d > 0$ is necessary for engine operation. In the three other cases, the pulse tube engine provides power outputs, which have maximum values at specific heat transfer capacities. For higher distribution ratios, the heat transfer capacities, which maximize the gross power, decrease. The highest gross power output of about $-0.5\,\mathrm{W}$ is achieved for the conditions of maximum thermodynamic asymmetry ($r_d = 3.4$) at a heat transfer capacity of about $0.3\,\mathrm{W/K}$. For the gross efficiency the heat flux in the pulse tube plays an important role. The maximum gross efficiency decreases for higher distribution ratios while the optimal heat transfer capacity for maximum gross efficiency remains almost constant. The highest gross efficiency of about 11% is achieved for the conditions of [23] ($r_d = 0.94$) at a heat transfer capacity of about $1.21\,\mathrm{W/K}$. Thus, the pulse tube material is acting as a regenerator, which takes on heat from the gas at the end of the expansion stroke and gives off heat to the gas at the end of the compression stroke. In contrast to the regenerator of the Stirling engine, a well designed pulse tube enables the exchange of a specific, optimal amount of heat between the pulse tube material and the working gas. At poor heat transfer conditions the pulse tube loses its regenerative property and at good heat transfer conditions the thermodynamic asymmetry decreases. Therefore, the thermal lag effect increases the efficiency of the pulse tube engine, but is not responsible for its operation. The underlying working principle is based on a broken thermodynamic symmetry.

The numerical model was applied successfully to describe the pulse tube engine cycle in detail, to confirm and enhance the predictions of the analytical model and to clarify the working principle of the engine.

2.10   Summary and conclusions of the numerical model

The most important results of the numerical analysis are summarized as follows:

1. Heat supply from the hot heat exchanger material to the working gas mostly occurs during the second half of the compression. During the expansion almost no heat is delivered to the gas by the hot heat exchanger.

2. During the compression the regenerator material absorbs compression heat and the heat added by the hot heat exchanger to the working gas. During the expansion the regenerator material completely releases the entire heat back to the working gas.

3. In the pulse tube, heat input to the working gas occurs towards the end of the compression stroke and heat output occurs towards the end of the expansion stroke.

4. Except for the pulse tube, all energy fluxes come to a standstill at the turning points of the piston.

5. In a cylinder with poor heat transfer conditions the working gas is expanded below the cold heat exchanger temperature, thus making the cold heat exchanger regenerative as well.

6. During the expansion stroke heat is released from the working gas by the cold heat exchanger. Thus, the pressure drops below the piston's rear side pressure, which decelerates the second phase of the expansion and accelerates the first phase of the compression due to the resulting pressure force on the piston. This enables a free piston operation of the engine.

7. The compression ratio influences the performance of the engine significantly. In subsection 2.9.2 the function $F(r_c)$, having the properties of Eq. (2.156), is introduced to correct the results obtained from the analytical model. Depending on the temperature of the hot heat exchanger, the compression ratio has optimal values for power output and efficiency. The optimal compression ratio of maximum efficiency is slightly higher than the optimal compression ratio of maximum power output.

8. The underlying working principle of the pulse tube engine is a broken thermodynamic symmetry. Thermodynamic asymmetry results from the fluidic linkage of an adiabatic space (pulse tube) with an isothermal space (regenerator) having the temperature distribution depicted in Fig. 1.2. An engine with a perfect adiabatic pulse tube can provide a power output. In contrast to the Stirling engine, the regenerator is essential for the functioning of the pulse tube engine.

9. The thermodynamic asymmetry can be maximized by the correct ratio between pulse tube volume and regenerator volume. The maximum power output is reached for more regenerator volume and the maximum efficiency for more pulse tube volume.

10. The thermal lag effect in the pulse tube supports the process and increases the efficiency of the engine. Maximum efficiency is achieved for a specific amount of heat transferred between the pulse tube material and the working gas. The

pulse tube has thus a regenerative property, which is bound to well adjusted heat transfer conditions.

With the developed numerical simulation model, a deep understanding of the pulse tube engine process was acquired and optimal design features for a working engine were found. The calculation time of the model is short enough to enable its usage for the design of working pulse tube engines.

Chapter 3

Development of a working engine

The results of chapter 2 are used to design and build a laboratory-scale test engine. In contrast to prior works like [23, 31, 40], the experiment focuses on the design of a pressurized pulse tube engine having a power output of several watts. This will allow for obtaining reliable experimental results from the test rig. As will be detailed below, this approach has the virtue that all design parameters such as heat transfer areas, diameters, porosity, dead volumes etc. are well known and available for the parametrization of the simulation models. The experimental test engine is equipped with a high number of temperature and pressure sensors, equipment for the measurement of the heat power input and the mechanical power output as well as frequency and crank angle measurement techniques. Furthermore, to identify power losses and get access to the power delivered to the piston rod, which is calculated by the numerical simulation model, the test set-up is designed to perform difference power measurements. The measured data, such as the time-dependent pressure, the temperature distribution and the power outputs, shall be used to quantify the accuracy of the developed simulation models and to systematically compare the performance of this engine with the theoretical predictions.

3.1 Design of the experimental pulse tube engine

Engine power output and efficiency have strong dependencies on the engine design and its operating conditions, such as the compression ratio, the distribution ratio, the temperature ratio, the operating frequency and the filling pressure. The experimental set-up is designed to study the engine performance within a wide range of design parameters and operating conditions.

3.1.1 General engine design and components

A CAD visualization of the test engine is shown in Fig. 3.1 (a). It consists of a cylinder
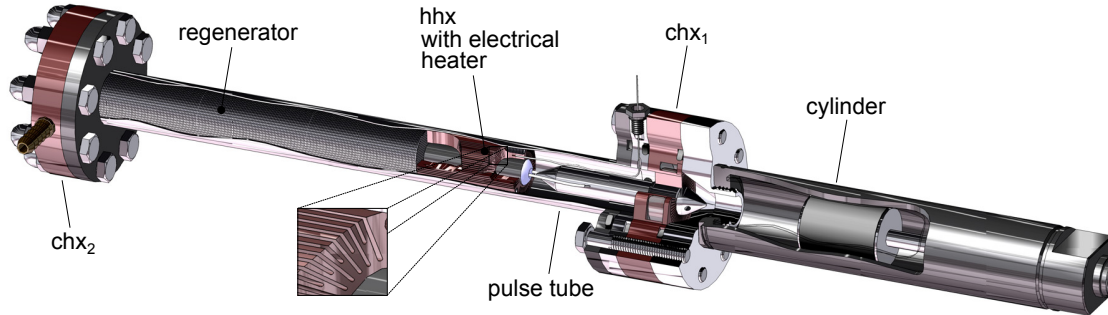
(a) CAD visualization
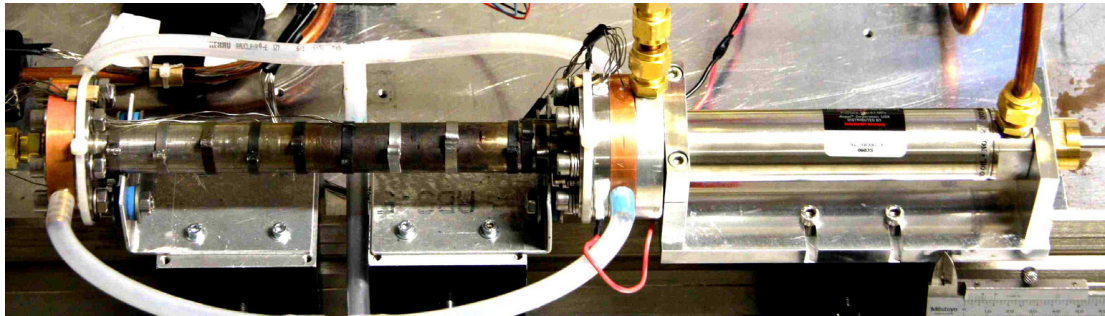
(b) Photograph

Figure 3.1: (a) CAD visualization of the pulse tube engine; (b) Photograph of the built laboratory-scale pulse tube engine.

with a bore of 24 mm and a variable stroke, adjustable between 20 mm and 100 mm. The cylinder is an AIRPEL Anti-Stiction air cylinder from the company Airpot. The front side of the cylinder is connected to a water cooled heat exchanger chx_1. The pulse tube, the hot heat exchanger (hhx) and the regenerator are placed in a stainless steel tube with an inner diameter of 20 mm and a total length of 230 mm. A photograph of the built laboratory-scale pulse tube engine is shown in Fig. 3.1 (b).

An electrical resistance heater is placed inside hhx. A water cooled copper body chx_2 with a connected copper tube of 4 mm in diameter and 143 mm in length is located at the regenerator's cold side. The structures of chx_1 and hhx are manufactured using electro-discharge machining. The heat transfer area of the hot heat exchanger has no theoretical limitation and is designed to be as large as possible. In contrast to that, the cold heat exchanger chx_1 needs a certain heat transfer area to allow optimal engine operation. To get the optimal heat transfer area the simulation model is used. The calculated optimal heat transfer area is 56 cm^2, which is thus used in the experiment. See Appendix **E** for details ($L_{chx} = 10$ mm corresponds to $A_{hx} \approx 50$ cm^2).

The regenerator is made of stacked stainless steel wire mesh screens with a mesh number of $n_m = 50$ and a wire diameter of $d_w = 200\,\mu$m. Its porosity is calculated with

$$e = \frac{V}{V + V_m} = 1 - \frac{\pi}{4}\frac{1000\,n_m\,d_w}{25.4}\sqrt{1 + \left(\frac{1000\,n_m\,d_w}{25.4}\right)^2} \tag{3.1}$$

to $e = 0.67$. The total wire mesh mass amounts to $200\,$g. Photographs of the regenerator material, the hhx with the electrical heater and the chx$_1$ are shown in Fig. 3.2. The

(a) Regenerator material

(b) Hot heat exchanger and electric resistance heater

(c) Cold heat exchanger
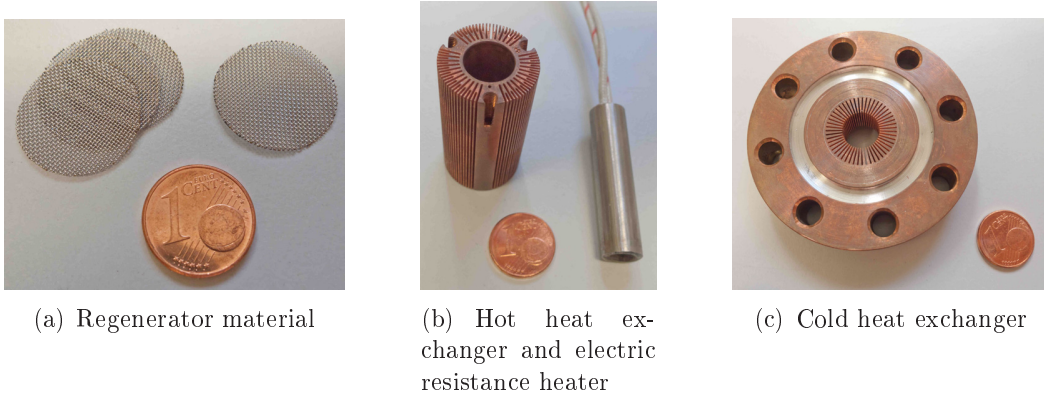
Figure 3.2: (a) Photograph of the regenerator material; (b) Photograph of the hot heat exchanger and the electric resistance heater, placed inside the hot heat exchanger; (c) Photograph of the cold heat exchanger.

pulse tube has a toroidal cross-section with inner and outer diameters of $10\,$mm and $20\,$mm, respectively.

The geometrical parameters of the components as well as the resulting values of the gas and material volume V and V_m, the free flow area A_f, the material's cross-section area A_m and the heat transfer area A_{hx} are listed in Table 3.1.

Table 3.1: Geometrical parameters of the engine components

Parameter	Unit	chx$_2$	regenerator	hhx	pulse tube	chx$_1$	cylinder
L	mm	143	122	40	68	11	40[*]
d_h	mm	4	0.4	0.6	10	0.6	24
V	cm^3	1.8	25.6	2.8	16.9	0.8	21...39[**]
V_m	cm^3	–	20.8	2.4	4.5	1.8	–
A_f	cm^2	0.1	2.1	0.7	2.4	0.8	4.5
A_m	cm^2	–	1.7	2.4	0.7	1.6	–
A_{hx}	cm^2	18	1700	187	43	56	44...74[**]

[*] stroke used in the experiment
[**] oscillating

For a stroke of $40\,$mm the displacement volume of the cylinder becomes $V_d = 18\,$cm^3.

The maximum and minimum gas volume are given by

$$V_{max} = V_d + V_0 + V_{pt} + V_{reg} + V_{hx} \qquad (3.2)$$

and

$$V_{min} = V_0 + V_{pt} + V_{reg} + V_{hx}, \qquad (3.3)$$

where V_0 represents the sum of the dead volume of the cylinder, and of the connected tubes and valves. The dead volume V_0 is located at low temperature and can entirely be regarded as cylinder dead volume. It is split into a known (measurable) dead volume V_0^a and an unknown dead volume V_0^b. The measured known dead volume is $V_0^a = 7.5\,\text{cm}^3$ and the free parameter V_0 is replaced by the free parameter V_0^b. Its value will be calculated from pressure measurements after building the engine. According to the results of subsection 2.8.3 it partly represents virtual dead volume due to leakage between piston and cylinder liner.

Adding the non-zero volume of chx$_1$ to the pulse tube volume and the non-zero volumes of hhx and chx$_2$ to the regenerator volume the distribution ratio of the engine results in $r_d = 1.71$. Without consideration of the dead volume and applying a stroke of 40 mm the compression ratio of the engine results in $r_c = 0.38$.

3.1.2　Experimental set-up and operating conditions

An experimental environment is necessary to enable an operation of the engine.

The structure of the experimental set-up is shown in Fig. 3.3. The rear side of the cylinder is connected to an external gas volume simulating a pressurized environment. The engine is filled with pressurized helium up to a filling pressure of $p_f = 12\,\text{bar}$. The piston front and rear side have a connecting tube, which can be opened and closed using valve V$_1$. This bypass tube allows to motor the engine without any pressure swing and almost no gas passing chx$_1$. The cold heat exchanger chx$_2$ can be opened and closed to the gas volume using valve V$_2$. This allows filling the engine with pressurized gas without opening V$_1$. The whole system is connected to a vacuum pump via valve V$_3$ and a compressed gas cylinder via valve V$_4$. It can be unpressurized by opening valve V$_5$ to the ambient air. The filling pressure is measured with a mechanical pressure gauge.
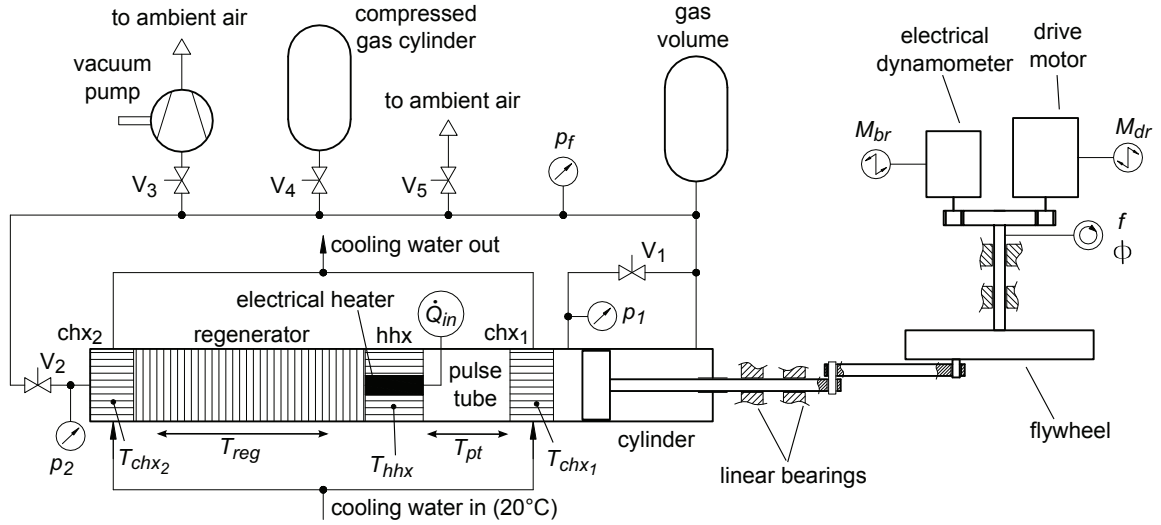
Figure 3.3: Structure of the experimental set-up. $V_1...V_5$: valves, $\dot{Q}_{in}$: thermal power input, p_f: mechanical pressure gauge, p_1 and p_2: piezoresistive pressure sensors, T_{chx_1}, T_{hhx}, T_{chx_2}, T_{pt}, T_{reg}: thermocouples, f: operating frequency, ϕ: crank angle, M_{br}: brake momentum, M_{dr}: drive momentum. The maximum permissible filling pressure of the engine is 12 bar.

The piston rod is guided by linear bearings. The linear movement is transformed into rotation via a crankshaft mechanism. The connected flywheel serves as rotational energy storage. Two electrical motors are connected to the flywheel. One is used as an electrical dynamometer to apply a brake momentum on the engine. The resulting electrical current is measured and used to calculate the brake momentum M_{br}. The second electrical motor serves as a drive to motor the engine. The electrical current of the drive motor is also measured to calculate the drive momentum M_{dr}.

The electrical heater, placed inside hhx, has a maximum permissible temperature of 700 °C and a maximum thermal power output of 160 W. The heater temperature is measured and controlled using a two-level controller. It can be fixed between 40 °C and 650 °C. The cold heat exchangers are water cooled with a cooling water inlet temperature of 20 °C.

A photograph of the experimental set-up is shown in Fig. 3.4. The corresponding process flow diagram is given in Fig. 3.5.

The engine can be run in two modes. In the first mode, the engine is operated purely through heating. In this mode the electrical dynamometer shown in Fig. 3.6 (a) is used to apply a brake momentum on the engine. In the second mode, the engine is motored or braked using the drive motor shown in Fig. 3.6 (b). In both cases the current of the electrical dynamometer or of the drive motor is measured and correlated to the respective dynamometer or drive motor momentum. The first mode is more accurate in measuring the provided shaft power output.
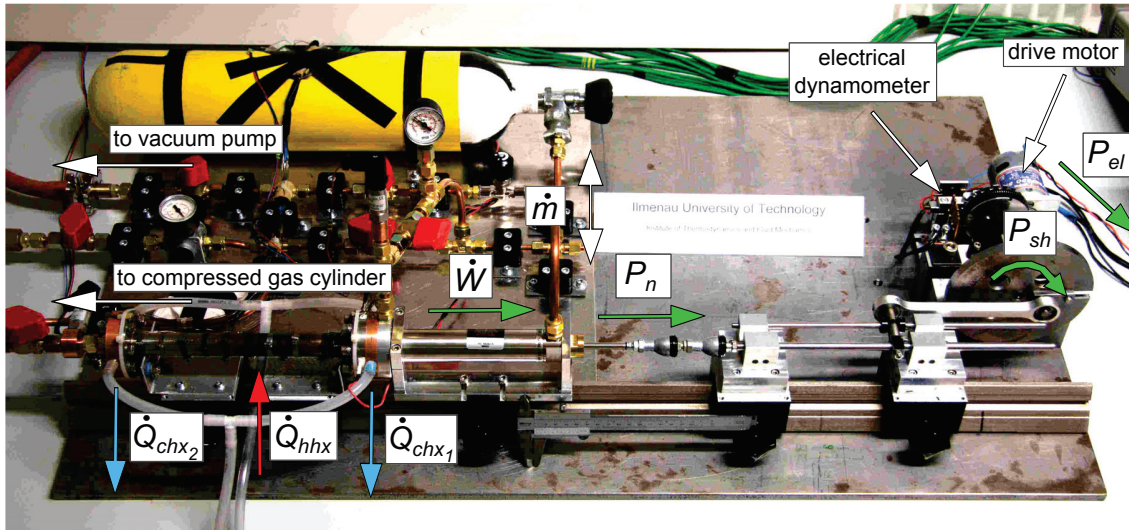
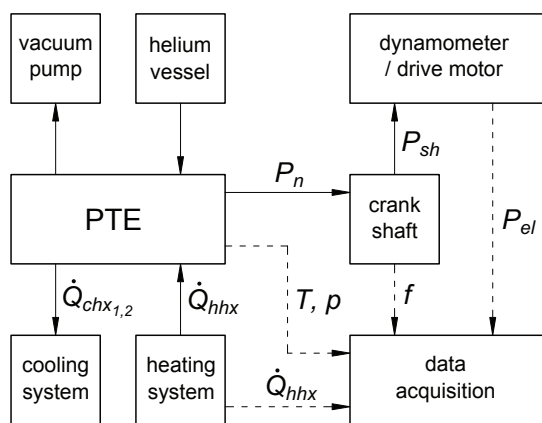**Figure 3.4:** Photograph of the pulse tube engine in its experimental environment.


Figure 3.5: Corresponding process flow diagram of the experimental set-up. PTE: $\underline{P}$ulse $\underline{T}$ube $\underline{E}$ngine; fluxes: $\dot{Q}_{hhx}$ ($= \dot{Q}_{in}$): heat power input, $\dot{Q}_{chx1,2}$: heat power outputs, $\dot{W}$: compression/expansion power, P_n: net power, P_{sh}: shaft power, P_{el}: generated electrical power, $\dot{m}$: mass flux between the piston rear side and the gas storage volume; measured quantities: T: temperature, p: pressure, f: operating frequency, P_{el}: electrical power input (motored engine) or electrical power output (braked engine).
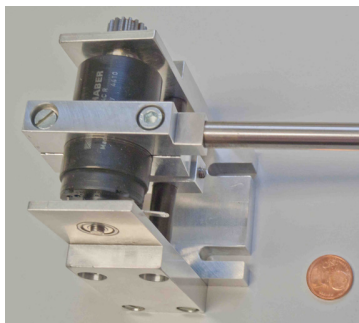

(a) Electrical dynamometer
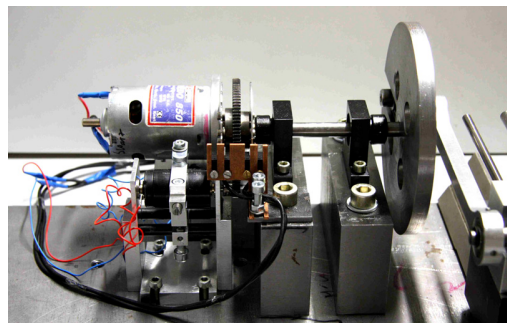
(b) Crank gear mechanism with electrical dynamometer, drive motor and light barriers

Figure 3.6: (a) Photograph of the electrical dynamometer; (b) Photograph of the crank mechanism with the used electrical dynamometer, drive motor and light barriers.

3.2   Measurement techniques

In order to characterize the pulse tube engine in operation, the signals of various sensors and measuring devices are monitored. Details of the used measurement techniques, developed in [77], are given in this section.

The main measured quantities are temperatures T, the supplied thermal power $\dot{Q}_{in}$, brake and drive torques M_{br} and M_{dr}, the working gas pressure p, the operating frequency f and the crank angle of the flywheel ϕ. The measured temperatures are in particular the material temperatures of the heat exchangers T_{chx_1}, T_{chx_2} and T_{hhx}, as well as the material temperature profiles of the pulse tube T_{pt} and of the regenerator T_{reg}. A scheme of the measurement is shown in Fig. 3.7.
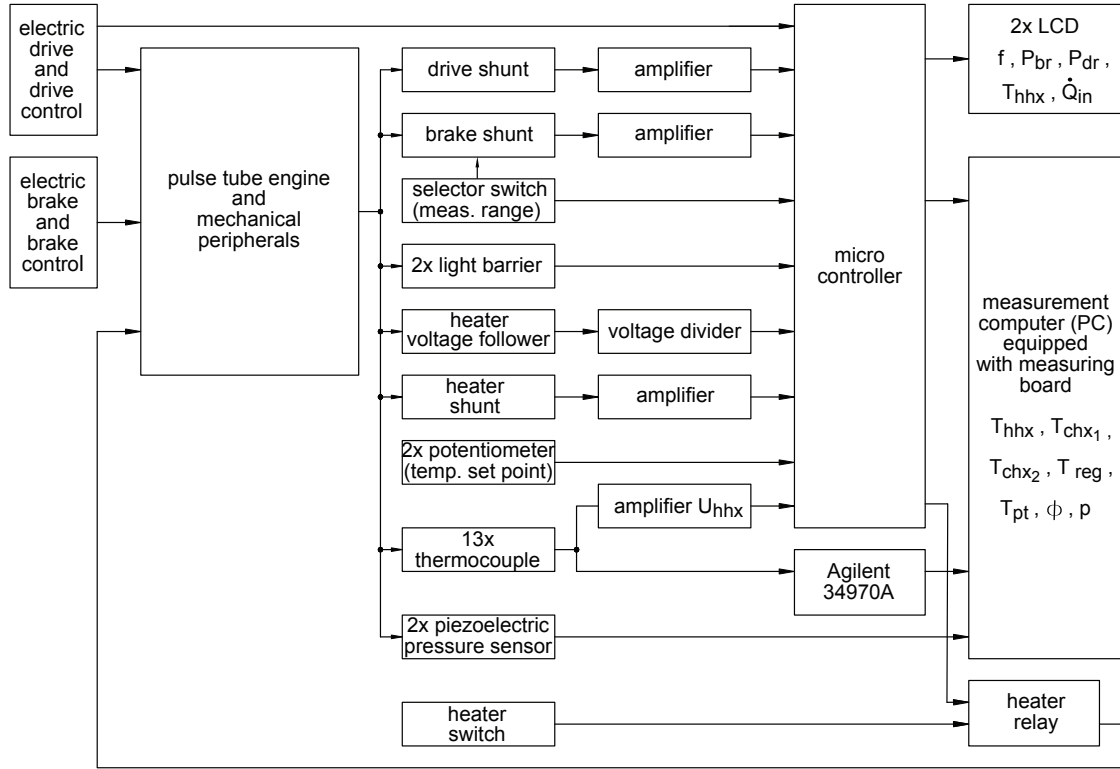
Figure 3.7: Structure of the data acquisition system. The operating frequency f, the brake power P_{br} or the drive power P_{dr}, the thermal power input $\dot{Q}_{in}$ and the temperature of the hot heat exchanger T_{hhx} are visualized on two Liquid Crystal Displays (LCD). The signals of the pressure sensors are transmitted to a personal computer (PC). All other measured quantities are processed by the micro controller or the Agilent 34970A and transmitted to a PC.

The supplied thermal power $\dot{Q}_{in}$ is calculated from the measured voltage and current of the heater power supply. Heat losses are quantified experimentally in subsection 3.4.2. The torques of the two electrical motors M_{br} and M_{dr} are calculated from its electrical currents, which are correlated to measured voltages of shunts. The current of the brake motor is smaller than the current of the drive motor. To increase the

accuracy of the brake motor current measurement, three switchable shunts are used. The measured voltages are amplified and processed by a micro controller. To ensure the highest possible precision, the amplification circuits were checked for their linearity prior to the measurements. The conversion factors between the measured voltages and the quantities to be identified were determined by calibrations. The values are stored in the micro controller's Flash-EEPROM. The measured brake and drive momentums are used to calculate the brake power P_{br} and the drive power P_{dr}.

The working gas pressure is recorded using piezoresistive pressure sensors p_1 and p_2 between chx$_1$ and cylinder as well as at chx$_2$. The sampling rate is $4\,\mathrm{kHz}$. The voltage signals are logged by a data acquisition system and monitored with a personal computer. Operating frequency f and crank angle ϕ are measured by two light barriers (see Fig. 3.6 (b)) at the interrupt input of the micro controller. The first light barrier is interrupted 20 times per revolution of the motor shaft, thus permitting a frequency measurement with an accuracy of $0.05\,\mathrm{Hz}$. The determination of the crank angle is made possible by the second light barrier which is interrupted only once per revolution and thereby setting the zero position of the crank angle. Each other interruption of the light beam of the first barrier increases the value of the crank angle by $18\,\mathrm{deg}$. The crank angle is converted into a voltage between zero and five volts via pulse width modulation and then forwarded to the data acquisition system and the personal computer. With this data the pV-diagram of the engine can be monitored.

The temperatures are measured with K-type thermocouples. The thermoelectric voltages are converted into temperatures by an AGILENT 34970A transducer with built-in reference junction. The data are transmitted via the RS232 interface every two seconds to the personal computer. The thermoelectric voltage of the thermocouple placed at the hot heat exchanger is also amplified externally and fed to the micro controller. The signal is used to control the heater temperature with a two-level controller.

3.3   Preparation of the numerical simulation model

The numerical model developed in section 2.7 is used to predict the measured engine performance. The following section aims to prepare the numerical model for realistic calculations of the working engine. To do so, relations for the heat transfer and for the internal and external power losses, which are applicable to a real pulse tube engine, are introduced. Necessary computation parameters are set and the remaining free parameters of the model, the unknown dead volume V_0^b and the starting position of the piston ϕ, are identified. Furthermore, the simulation model is used to study the heat fluxes occurring in the components of the developed engine.

3.3.1   Calculation of heat transfer and power losses

In the working pulse tube engine, the heat transferred from the solid material to the working gas is limited. The power output is reduced by power losses due to heat conduction and flow friction. The relations to calculate these mechanisms are presented below.

Heat transfer

The heat flux $\dot{Q}_{hx}$ between the working gas and the material is calculated with the heat transfer area A_{hx} using

$$\dot{Q}_{hx} = \alpha \, A_{hx} \, (T_m - T) \,, \tag{3.4}$$

where the heat transfer coefficient is calculated using $\alpha = Nu\lambda_g/d_h$, with the Nusselt number Nu, the gas heat conductivity λ_g and the hydraulic diameter d_h. The Nusselt number is obtained from experimental correlations depending on the flow field [74].

The relation between inertial and viscous forces is characterized by the Reynolds number Re, calculated with $Re = \dot{m}\,d_h/\mu/A_f$, where μ represents the dynamical viscosity of the fluid. The relation between viscous and thermal diffusion is characterized by the Prandtl number calculated with $Pr = \mu\,c_p/\lambda_g$.

For the cylinder, the heat exchangers and the pulse tube, the heat transfer coefficient α is obtained from correlations given in [75]. With $\zeta = RePr\,d_h/L$ the Nusselt number for a tube flow is calculated from

$$Nu_t = \left(49.371 + \left(1.615\,\zeta^{\frac{1}{3}} - 0.7\right)^3 + \sqrt{\frac{2}{1 + 22\,Pr}\,\zeta^{\frac{3}{2}}}\,\right)^{\frac{1}{3}}, \tag{3.5}$$

where the hydraulic diameter is calculated with the tube diameter d to $d_h = d$. For a rectangular duct flow the Nusselt number is calculated using

$$Nu_d = \left(428.832 + 6.24\,\zeta + \sqrt{\frac{2}{1 + 22\,Pr}\,\zeta^{\frac{3}{2}}}\,\right)^{\frac{1}{3}}, \tag{3.6}$$

where the hydraulic diameter is calculated with the duct width w to $d_h = 2\,w$.

Since the porous structure of the regenerator is made of stacked wire mesh screens, experimental correlations for α from [58, 78] are used. The heat transfer area A_{hx} in the regenerator with the length L and the diameter d is given by

$$A_{hx} = e\,(1 - e)\,\frac{\pi\,d^2\,L}{d_w}\,. \tag{3.7}$$

The heat transfer coefficient is obtained from [58] to be

$$\alpha = \psi \, \frac{c_p \, \mu}{d_h} \frac{Re}{Pr^{2/3}} \,, \tag{3.8}$$

where the heat transfer module ψ is calculated with [78]

$$\psi = \left(2.128 - 8.591 \, e + 9.6878 \, e^2\right) Re^{-0.113 - 0.475 \, e} \,. \tag{3.9}$$

Internal power losses

Axial heat fluxes due to heat conduction in the gas and the material are only important for the pulse tube and the regenerator. For each sub-control volume the heat flux due to heat conduction is calculated at its left side with

$$\dot{Q}'_{cg/m,i} = \frac{\lambda_{g/m} \, A_{f/m}}{L} \left(T_{g/m,i-1} - T_{g/m,i}\right) \,, \tag{3.10}$$

and at its right side with

$$\dot{Q}''_{cg/m,i} = \frac{\lambda_{g/m} \, A_{f/m}}{L} \left(T_{g/m,i+1} - T_{g/m,i}\right) \,, \tag{3.11}$$

where $\lambda_{g/m}$ represents the heat conductivity of the gas (g) or of the material (m). The free flow area is A_f and the material cross-section area is A_m. For the pulse tube, in the case of $i = 1$ the temperature $T_{g/m,i-1}$ equals T_c and in the case of $i = n$ the temperature $T_{g/m,i+1}$ equals T_h. For the regenerator, in the case of $i = 1$ the temperature $T_{g/m,i-1}$ equals T_h and in the case of $i = n$ the temperature $T_{g/m,i+1}$ equals T_c. In the other components no heat conduction is considered.

The gas flow in the cylinder, the heat exchangers and the pulse tube has low Reynolds numbers ($Re < 1000$), so that the friction factor relation $f_f = 16/Re$ for laminar flow [79] is applicable. In the regenerator even lower Reynolds numbers ($Re < 100$) are present. According to [80, 81] the flow field in porous media can be turbulent at low Reynolds numbers, too. To calculate the friction force in the regenerator an experimental friction factor correlation from [78]

$$f_f = \frac{718.7 - 1958 \, e + 1415.9 \, e^2}{Re} + \frac{1.348/e - 0.854}{Re^{0.15}} \tag{3.12}$$

is used.

As mentioned in chapter 2 the experimental correlations for $f_f(Re, e)$ and $\psi(Re, e)$, given in [58, 78], are valid for fully developed stationary flows, but also used for the

present transient analysis. The induced modeling error resulting from this is judged to have minor importance compared to the error induced by the one-dimensional modeling.

External power losses

The friction force in the cylinder is proportional to the constant gravity force of the piston and piston rod. For the crank mechanism the friction force in the linear and rotating bearings is a superposition of the constant gravity force of the rod and the shear force caused by the crank mechanism. The shear force is proportional to the oscillating mass force, which is proportional to the square of the operating frequency f^2. Thus, the total friction power loss $P_{l,ext}$ in the cylinder and the crank shaft can be modeled according to

$$P_{l,ext}(f) = A\,f + B\,f^3\,,\tag{3.13}$$

where the influence of the filling pressure variation is neglected and A and B are constant fitting parameters obtained from the experiment.

3.3.2 Computation parameters

To perform comparable numerical calculations within the available time frame, reasonable values for the number of pulse tube and regenerator sub-control volumes as well as for the size of the time step have to be specified. Both values are set as follows:

After achieving an equilibrium material temperature Eq. (2.9) becomes

$$0 = -\dot{Q}_{hx} + \dot{Q}'_{cm} + \dot{Q}''_{cm} + \dot{Q}_{ext}\,.\tag{3.14}$$

The total amount of heat exchanged per cycle between the material of the respective engine component and the surroundings (heat source, cooling water etc.) is calculated with $\dot{Q}_{ext,cyc} = f \oint \dot{Q}_{ext}\,dt$, where $\dot{Q}_{ext}$ is obtained from Eq. (3.14). The necessary amount of cycles to achieve an equilibrium in the material temperature is about 300. This value is used for all simulations. In order to reduce computation time the number of sub-control volumes for pulse tube and regenerator is reduced to $n_{pt/reg} = L_{pt/reg}/2$, where L is the length of the pulse tube or of the regenerator measured in millimeters.

The threshold value in the smoothing function (2.148) is set to $\dot{m}_{tr} = 10\,\mathrm{mg/s}$. All calculations are performed with minimum and maximum permissible time increments of $\Delta t_{min} = 10^{-8}\,\mathrm{s}$ and $\Delta t_{max} = 10^{-5}\,\mathrm{s}$, respectively, leading to a total calculation time of about 20 hours for 300 cycles on a regular state of the art personal computer. The numerical model can thus be used to predict the engine performance within a reasonable calculation time.

3.3.3   Model calibration

According to section 3.1 the remaining free parameters which need to be quantified are the unknown dead volume V_0^b and the starting position of the piston ϕ. Both are obtained from the measured pressure swing of the motored engine at ambient temperature ($20\,°\mathrm{C}$). To do so the engine is calculated for filling pressures between $6\,\mathrm{bar}$ and $10\,\mathrm{bar}$ at a fixed operating frequency of $8\,\mathrm{Hz}$.
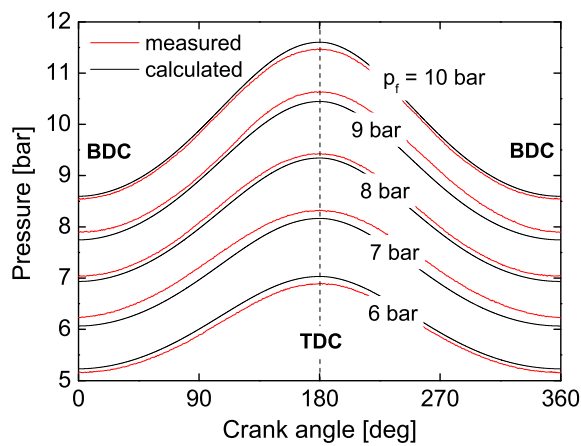

Figure 3.8: Comparison of the calculated and measured pressure as functions of the crank angle. The engine is motored at ambient temperature ($T_h = T_c = 20\,°\mathrm{C}$) for filling pressures between $6\,\mathrm{bar}$ and $10\,\mathrm{bar}$ at an operating frequency of $8\,\mathrm{Hz}$.

In the simulation, the parameters V_0^b and ϕ are varied until the difference between the calculated and measured minimum engine pressure and the calculated and measured pressure amplitude becomes minimal. The results of this procedure are $\phi = 76\,\mathrm{deg}$ and $V_0^b = 13.5\,\mathrm{cm}^3$. Thus, the total additional dead volume of the engine is $V_0 = V_0^a + V_0^b = 21\,\mathrm{cm}^3$. A comparison of the calculated and measured pressure swing is shown in Fig. 3.8. The obtained relative differences between the calculated and measured minimum pressures and the pressure amplitudes are smaller than 2.5% and 3.2%, respectively.

3.3.4   Calculation of the heat fluxes in the components

The numerical model is used to investigate the heat fluxes occurring in the engine components.

In Fig. 3.9 the calculated total heat fluxes between gas and material (see subsection 2.7.2) for pulse tube, hhx and regenerator are shown over one engine cycle. A positive sign means that heat is added to the gas. In the hhx the calculated amount of heat added to the gas at the end of the compression is much higher than during expansion. The regenerator material is absorbing heat from the gas during compression. The assumption that the working gas takes on heat during compression is satisfied for this engine. The absorbed heat is stored in the regenerator material and given back to the gas during expansion.
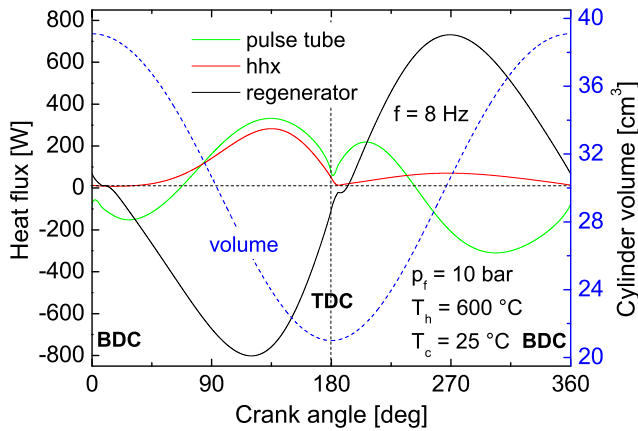
Figure 3.9: Calculated and measured heat fluxes over one engine cycle; BDC: bottom dead center, TDC: top dead center. Compression stroke: 0 deg to 180 deg, Expansion stroke: 180 deg to 360 deg.

The heat flux progression between working gas and pulse tube material discloses that the pulse tube material is regenerative as well. In the pulse tube, heat is added to the gas around TDC and removed from the gas around BDC. This thermal lag effect [27] was discovered by Tailer [26]. The pulse tube engine is an extension of Tailer's thermal lag machine. It is able to run with an ideal adiabatic pulse tube suppressing a thermal lag. The arrangement of pulse tube, hhx and regenerator makes this possible.

Moreover, as predicted in the subsections 2.3.4 and 2.9.1, in the pulse tube, heat is added to the working gas throughout the cycle, enabling the pulse tube engine to use heat at the temperature of the pulse tube, which has the distribution shown, for instance, in Fig. 1.2 of subsection 1.2.1 or Fig. 3.10 of the following section.
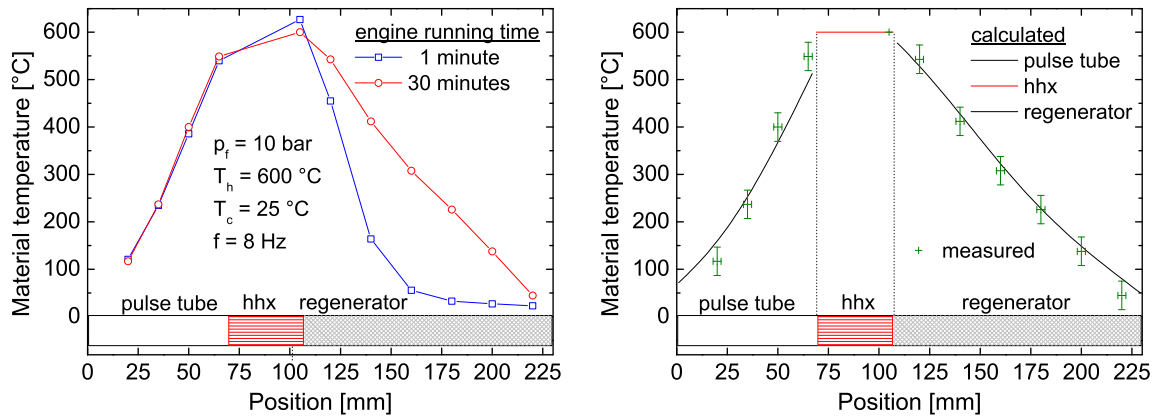
3.4 Characterization of the experimental set-up

To characterize the experimental set-up and to quantify the measured power output, the temperature distributions, the thermal power loss of the electrical heater and the power dissipation in the cylinder and crank mechanism are investigated in this section.

3.4.1 Measured and calculated temperature distribution

The material temperature distributions along pulse tube and regenerator are calculated with the numerical model and compared to the measured material temperature distributions.

The measured material temperature profiles along pulse tube and regenerator after the first minute and after half an hour of operation are shown in Fig. 3.10 (a). It can be seen that the regenerator needs a certain operational time to reach an equilibrium temperature. A comparison of the calculated equilibrium material temperature distribution with the measured values is shown in Fig. 3.10 (b). The thermocouples are set with a positioning accuracy of 2 mm. They are fixed using metal stripes. The error in the temperature measurement due to unknown thermal contact between thermocouple

(a) Measured material temperature distribution of pulse tube and regenerator

(b) Comparison of the calculated and measured material temperature distribution

Figure 3.10: (a) Measured material temperature distribution along pulse tube and regenerator after the first minute of engine operation and after half an hour of engine operation; (b) Comparison of the calculated and measured material temperature distribution along pulse tube and regenerator. The temperatures are $T_c = 25\,°C$ and $T_h = 600\,°C$.

and material is estimated to be $30\,K$. On a qualitative basis and within the existent error ranges for the positions and the temperatures, the results of the calculation and observation match well. The model predicts the bent profile of the pulse tube's material temperature and the more linear profile of the regenerator's material temperature. The higher axial heat flux in the regenerator material leads to a linearization of its temperature distribution compared to the pulse tube. The lower material temperature profile of the pulse tube is a result of the incoming cold gas from chx_1 during the compression stroke and the conversion of supplied heat power from hhx into expansion power during the expansion stroke. In Fig. 3.10 (a), the monotonous temperature rise between the highest pulse tube and the highest regenerator temperature does not represent the hhx temperature distribution. Both values are just jointed by a straight line in the plot. For calculation and measurement, the gradient of the pulse tube's hot end temperature is much higher than the gradient of the regenerator's hot end temperature. Thus, a gas parcel traveling during compression from the pulse tube through the hot heat exchanger is heated more than a gas parcel traveling during expansion from the regenerator through the hot heat exchanger.

3.4.2 Measured versus calculated thermal power input

The measured thermal power input is now compared to the numerical predictions.

The engine operates at $T_h = 600\,°C$, $T_c = 25\,°C$ and filling pressures between $6\,bar$ and $10\,bar$. The electrical dynamometer is used to apply a brake momentum on the shaft and the respective thermal power input is measured and calculated. The measured

thermal power is obtained from the electrical power consumption of the heater placed inside the hot heat exchanger. A comparison of the measured and calculated thermal
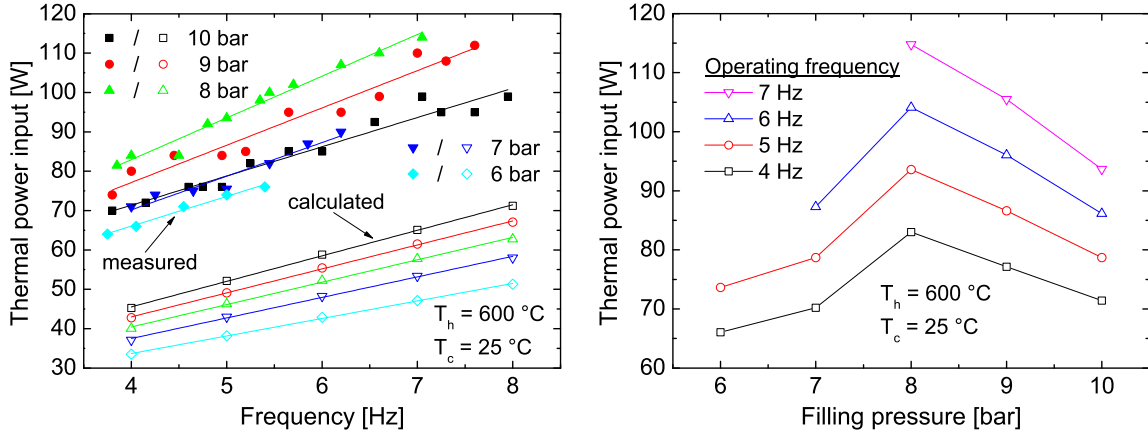
(a) Comparison of the calculated and measured thermal power input

(b) Correlation between the thermal power input and the filling pressure

Figure 3.11: (a) Comparison of the calculated and measured thermal power input as functions of the operating frequency for filling pressures between 6 bar and 10 bar; (b) Non-linear correlation between the measured thermal power input and the filling pressure. The cooling temperature is 25 °C and the heater temperature is 600 °C.

power input is given in Fig. 3.11 (a). The measured thermal power input is about 40% (10 bar, 8 Hz) to 95% (6 bar, 4 Hz) higher than the calculated thermal power input. The reason is that not all the electrical power converted into heat power is transferred to the working gas. A high portion is lost to the surroundings. This loss can be avoided using heat radiation insulation, which was not applied to the present experimental set-up. However, calculated and measured heat power input increase linearly with the operating frequency at an average slope of about 7.2 W/Hz.

The calculation predicts a monotonic increase of the thermal power input with the filling pressure. According to Fig. 3.11 (b), in the experiment, the thermal power input increases only between 6 bar and 8 bar of filling pressure. For higher filling pressures the thermal power input decreases. Two reasons could be responsible for this behavior. First, an increased heat transfer in the pulse tube, which acts according to subsection 2.9.4 as a regenerator, increases the engine efficiency. Second, a smaller temperature difference between the working gas and the heat exchanger material associated with a lower entropy production during the heat transfer process decreases the heat transfer power loss.

3.4.3 Friction power loss in the cylinder and crank shaft

To quantify the external friction power loss experimentally the engine is motored using the drive motor while valve V_1 is open. Thus, no compression occurs in the cylinder.

In this mode the power consumption of the drive motor equals the friction power loss in the cylinder and the crank mechanism. The experiment is done for filling pressures between 6 bar and 10 bar and frequencies between 4 Hz and 12 Hz. The result is shown in Fig. 3.12.
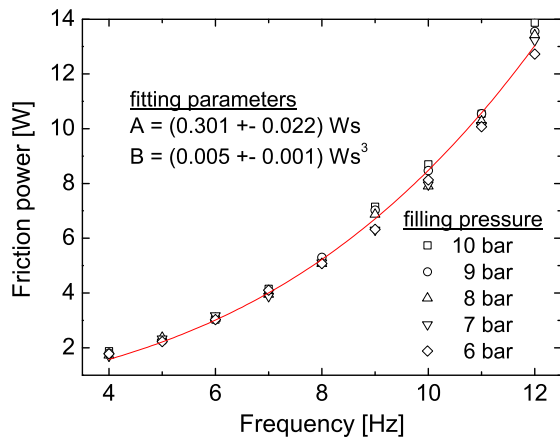
Figure 3.12: Fit of the measured power consumption due to mechanical friction in the cylinder, the linear bearings and the crank shaft as a function of the operating frequency. The filling pressure is varied between 6 bar and 10 bar, and the resulting shaft power consumptions are averaged at each frequency.

The observed influence of the filling pressure on the friction power loss is small. According to subsection 3.3.1, at each frequency the friction power is averaged over all filling pressures, and the averaged friction power is fitted with Eq. (3.13).

The resulting fitting parameters are $A = (0.301 \pm 0.022)\,\mathrm{W\,s}$ and $B = (0.005 \pm 0.001)\,\mathrm{W\,s}^3$.

In order to simplify the graphical visualizations in the following sections 3.5 and 3.6 all heat power inputs, mechanical power outputs and power losses have a positive sign. Mechanical power input by the drive motor is given a negative sign.

3.5 Measured and calculated engine performance

In this section the thermal power inputs, the mechanical power outputs and the engine efficiency are measured and shall be compared to the theoretical predictions using the numerical and the analytical model.

To do so, the performance of the developed pulse tube engine is measured for different filling pressures, heater temperatures and operating frequencies, and the observations are compared with the corresponding calculated predictions. To allow the quantification of power loss all measurements are done for opened and closed valve V_1.

3.5.1 Measured shaft power and efficiency

The shaft power can be measured directly. The respective measured performance results of the engine are presented in this subsection.

The operating conditions of the engine are the same as in subsection 3.4.2. For $T_h = 600\,°C$ and filling pressures between $6\,bar$ and $10\,bar$ the measured shaft power P_{sh} and shaft efficiency η_{sh} are shown in Fig. 3.13 (a, b). The efficiency is calculated

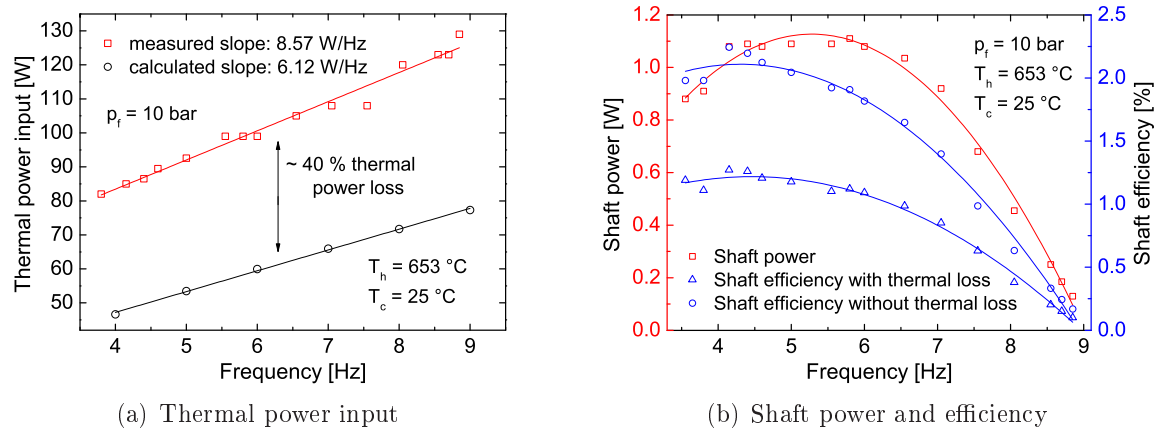(a) Shaft power   (b) Shaft efficiency
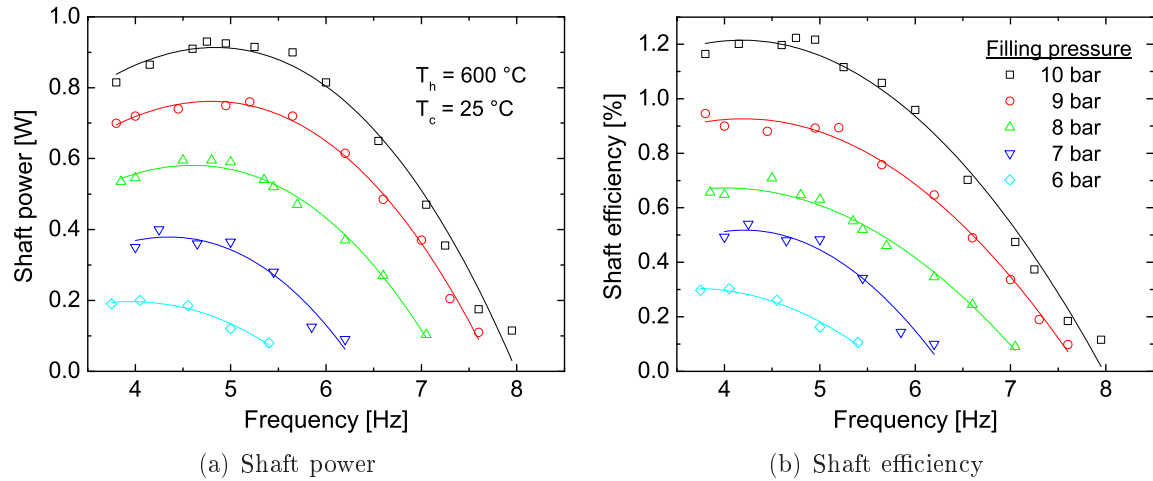
Figure 3.13: (a) Measured shaft power output as a function of the operating frequency; (b) Measured shaft efficiency as a function of the operating frequency. The filling pressure is varied between $6\,bar$ and $10\,bar$. The temperatures are $T_c = 25\,°C$ and $T_h = 600\,°C$.

with $\eta_{sh} = P_{sh}/\dot{Q}_{in}$, where $\dot{Q}_{in}$ is the measured electrical power consumption of the heater. As shown in subsection 3.4.2 the calculated thermal power input is about 40% to 95% lower than the measured value. Thus, the thermal power delivered to the working gas is smaller leading to a lower efficiency than what is predicted. However, power and efficiency increase with higher filling pressures. For a given filling pressure the peak frequency of the power is slightly higher than the peak frequency of the efficiency. Both values increase with higher filling pressures. Having a filling pressure of $10\,bar$, the highest shaft power of about $0.9\,W$ with an efficiency of about 1.2% is provided at a frequency of $5\,Hz$. According to subsection 3.4.3 the friction power loss at this frequency is $2.2\,W$.

3.5.2 Engine performance capabilities

To evaluate the maximum performance of the present experimental pulse tube engine, its shaft power output capabilities at maximum operating conditions are investigated. The maximum permissible filling pressure is limited by the burst strength of the stainless steel tube. Due to the high heater temperature a filling pressure of $10\,bar$ is used.

For a heat input temperature of 653 °C and a cooling temperature of 25 °C the measured and calculated thermal power inputs for operating frequencies between 4 Hz and 9 Hz are shown in Fig. 3.14 (a). As discussed in subsection 3.4.2, it increases linearly with the operating frequency. The calculated and measured thermal power inputs for $T_h = 653$ °C have a comparable slope of 6.12 W/Hz and 8.57 W/Hz, respectively. The calculated power inputs are about 40% lower than the measured ones. The reason is a loss of supplied thermal energy to the surroundings as discussed in subsection 3.4.2. The model does not take this loss mechanism into account.

(a) Thermal power input   (b) Shaft power and efficiency

Figure 3.14: (a) Comparison of the calculated and measured thermal power input as functions of the operating frequency at maximum operating conditions; (b) Shaft power and efficiency as functions of the operating frequency at maximum operating conditions. The cooling temperature is 25 °C and the heater temperature is 653 °C. The filling pressure is 10 bar.

The measured shaft power output and the shaft efficiency are shown in Fig. 3.14 (b). The brake momentum is applied with the electrical dynamometer. The efficiency is calculated with the measured and the calculated thermal power input from Fig. 3.14 (a). It is evident that shaft power and efficiency have clear maximal values for specific operating frequencies. The optimal frequency for the shaft efficiency is about 1 Hz smaller than the optimal frequency for the shaft power. This behavior is a general characteristic of heat engines, and is due to the fact that the shaft momentum reaches its peak value at a lower frequency than the shaft power. After the peak shaft momentum has been reached, the shaft power still increases, but the slope is lower than that of the thermal power input. The peak shaft efficiency occurs at about the same frequency as the peak shaft momentum.

The power output and efficiency capabilities of the built pulse tube engine are low, but within the projected range of several watts. This is sufficient to obtain reliable experimental results from the test rig and allows a comparison with the theoretical predictions.
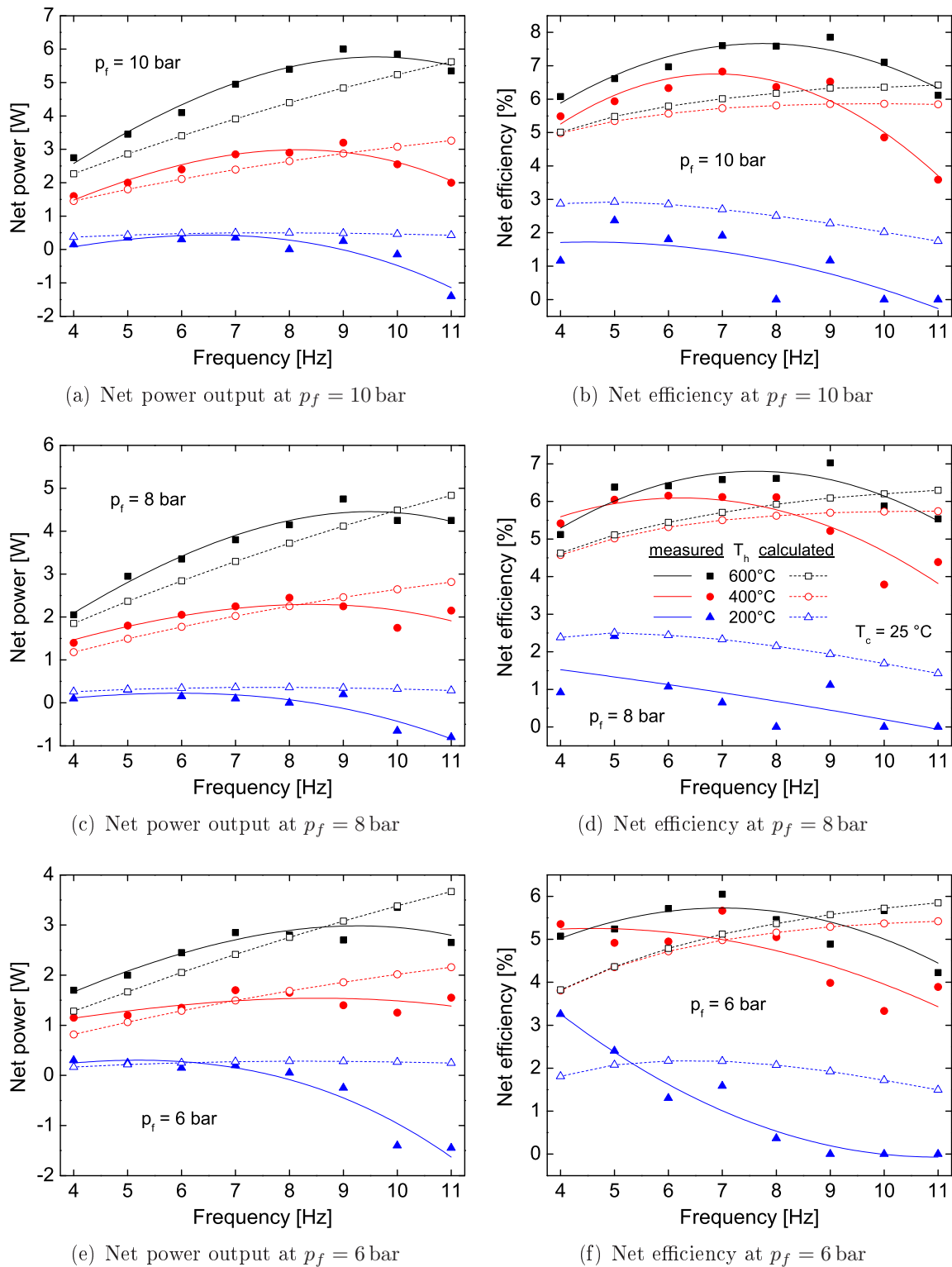
3.5.3 Measured versus calculated net power and efficiency

The net power of the pulse tube engine is obtained experimentally from the difference between the measured power consumption of the motored uncompressed engine (V_1 opened) and the motored compressed engine (V_1 closed). In this subsection the gained experimental results for the net power and efficiency are compared to the predictions of the numerical model.

In the uncompressed case, the drive motor has to deliver power P_{sh} to the shaft, which equals the power loss $P_{l,ext}$ due to mechanical friction in the crank shaft and the cylinder. In the compressed case, the amount of power delivered by the drive motor is reduced by the net power output P_n produced by the pulse tube engine. The net power is calculated from $P_n = P_{sh} + P_{l,ext}$ and the net efficiency is calculated with $\eta_n = P_n/\dot{Q}_{in}$, where P_n is the measured net power and $\dot{Q}_{in}$ the heat power input to the gas obtained from the numerical simulation. Measurements and calculations are performed for heat input temperatures of 200 °C, 400 °C and 600 °C as well as filling pressures of 6 bar, 8 bar and 10 bar. A comparison of the measured and calculated power outputs and efficiencies is given in Fig. 3.15. The filled symbols represent the measured and the unfilled symbols the calculated net power outputs and efficiencies. Within the restricted accuracy of the one-dimensional model, the calculated power outputs match the experimental results well. At all filling pressures the relative difference in the calculated and measured net power outputs for $T_h = 400$ °C and $T_h = 600$ °C is smaller than 40%. At a heat input temperature of $T_h = 200$ °C the relative difference is very high. A maximum error of 465% occurs at $T_h = 200$ °C, $p_f = 6$ bar and $f = 8$ Hz. Due to its low absolute value, the uncertainty of the calculated net efficiency is quite high.

The modeling error is estimated to be about 20%. The relative uncertainty of the measurement procedure is in the range of 30% and at least of 0.4 W. The total relative difference of the net power between calculation and experiment is thus about 50%. For $T_h = 400$ °C and $T_h = 600$ °C the error of the net power output is in the range of this uncertainty. Since the net power output for $T_h = 200$ °C is smaller than 0.4 W, the obtained relative error can be very high, but is still within the range of the measurement uncertainty. With increasing frequencies, the measured net power increases more strongly than the calculated net power. This could be caused by an increasing heat transfer rate, which is not reproduced sufficiently by the simulation model.

The engine provides a net power output for all heat input temperatures and filling pressures. The measured net power output for $T_h = 200$ °C is not reliable since the values are smaller than the measurement uncertainty of 0.4 W. It is possible, that

(a) Net power output at $p_f = 10$ bar

(b) Net efficiency at $p_f = 10$ bar

(c) Net power output at $p_f = 8$ bar

(d) Net efficiency at $p_f = 8$ bar

(e) Net power output at $p_f = 6$ bar

(f) Net efficiency at $p_f = 6$ bar

Figure 3.15: Comparison of the calculated and measured net power output and net efficiency as functions of the operating frequency for $T_c = 25\,°C$ and heat input temperatures of $600\,°C$, $400\,°C$ and $200\,°C$ at filling pressures of 10 bar (a, b), 8 bar (c, d) and 6 bar (e, f).

the engine does not provide a net power output for $T_h = 200\,°\text{C}$. However, the net power increases with temperature and pressure. The increase rate slows down strongly for higher temperatures, such that the temperature has no significant influence on the efficiency anymore. This result implies that with increasing temperature difference, more heat energy is dumped due to an enthalpy flow from the hot to the cold side of the pulse tube, which is in accordance with the predictions of the analytical model in section 2.6. For $T_h = 600\,°\text{C}$, $p_f = 6\,\text{bar}$ and $9\,\text{Hz}$ the engine has a maximum net efficiency of about 8%. The peak of the net power is always at a higher frequency than the peak of the net efficiency. Compared to the shaft power and efficiency, the peak values of the net power and efficiency are about $5\,\text{Hz}$ higher, which is a result of the power dissipation in the cylinder and crank mechanism discussed in subsection 3.4.3.

3.5.4 Internal power losses, gross power and efficiency

The functional principle of the pulse tube engine is based on an intrinsically irreversible thermodynamic cycle [46]. Gross power is produced due to an irreversible thermal relaxation in the pulse tube. The results of the analytical model gained in subsection 2.3.6 shall be compared to the measured engine performance.
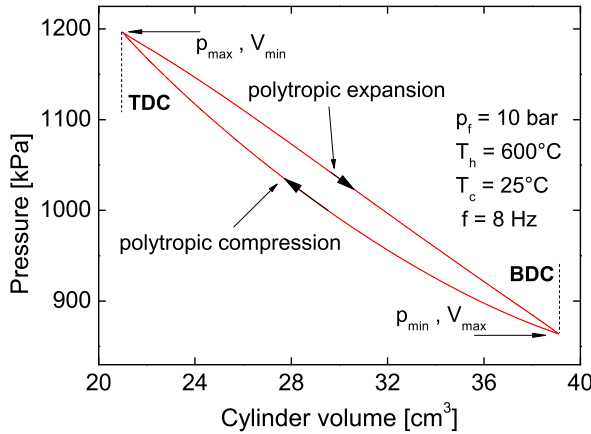
Figure 3.16: Calculated pV-diagram of the built pulse tube engine with a filling pressure of $10\,\text{bar}$, a heat input temperature of $600\,°\text{C}$, a cooling temperature of $25\,°\text{C}$, and a frequency of $8\,\text{Hz}$.

Fig. 3.16 shows the pV-diagram of the working pulse tube engine, calculated with the numerical model for $p_f = 10\,\text{bar}$, $f = 8\,\text{Hz}$, $T_h = 600\,°\text{C}$ and $T_c = 25\,°\text{C}$. The engine operates between minimum pressure p_{min} and maximum pressure p_{max}. In contrast to the assumption of an isochoric thermal relaxation at TDC and BDC made in the analytical model, the working pulse tube engine does not show this property. However, the basic characteristics of the engine disclosed in chapter 2 remain.

Applying a global polytropic model [57] to the entire engine, a polytropic compression stroke from BDC to TDC occurs with the polytropic exponent $n_p^c(V)$ and a polytropic expansion stroke from TDC to BDC occurs with the polytropic exponent $n_p^e(V)$. If the function $n_p^c(V)$ differs from the function $n_p^e(V)$ the engine is able to provide a gross power output.

With the ratio of the maximum to the minimum engine gas volume $V_{max}/V_{min} = 1.26$ and the experimentally observed pressure ratio of $\Pi = 1.34$, the mean polytropic exponent n_p can be obtained from

$$\Pi = \left(\frac{V_{max}}{V_{min}}\right)^{n_p} \tag{3.15}$$

to be $n_p = 1.27$. The used working gas helium has a mean adiabatic exponent of $\kappa = 1.67$. Thus, the global compression and expansion processes tend to be close to isothermal behavior ($n_p = 1$). This backs the used isothermal compression and expansion for the analytical model in section 2.3.

A result of the analytical model in subsection 2.3.6 is an approximation of the pV-work. Furthermore, in subsection 2.9.2 the function $F(r_c)$ was defined to introduce the numerically observed dependency of the pV-work on the compression ratio. The gross power P_g is related to the pV-work through $P_g = f\, W_{pV}$. Using Eq. (2.158) its absolute value can be approximated by

$$P_g \approx f\, F(r_c)\, p_{min}\, V_d\, \frac{r_d\,(\tau - 1) - 1}{(r_d + 1)^2}\,(1 + \chi_{pV}), \tag{3.16}$$

with

$$\chi_{pV} = -\frac{\left(4\, r_d^3\,(r_c + 1) + r_c\,(6\, r_d^2 + 4\, r_d + 1)\right)(r_d\,(\tau - 1) - 1)}{4\,(2\, r_d + 1)\,(r_d + 1)^2\,(2\, r_d\,(r_c + 1) + r_c)}\,.$$

The net power output of the engine is $P_n = P_g - P_{l,int}$, where the total internal power loss $P_{l,int}$, in general, is a function of at least f, p_f, T, geometry parameters such as r_c, r_d and V_d as well as working gas properties. The geometry of the engine ($r_c = 0.38$, $r_d = 1.71$ and $V_d = 18\,\mathrm{cm}^3$) is fixed. Thus, the internal power loss is reduced to being a function of f, p_f, T and the working gas properties. The main influence of the temperature on the internal power loss is due to the temperature dependency of the working gas properties. Assuming a perfect gas and neglecting the remaining secondary dependency of the internal power loss on the temperature, the internal power loss is only a function of the frequency f and the filling pressure p_f.

Since r_c is fix, the function $F(r_c)$ becomes a constant factor. The net power can thus be expressed trough

$$P_n \approx F\, f\, p_{min}\, V_d\, \frac{r_d\,(\tau - 1) - 1}{(r_d + 1)^2}\,(1 + \chi_{pV})\, -\, P_{l,int}(f, p_f). \tag{3.17}$$

For a fixed frequency and filling pressure, the factor F and the total internal power loss $P_{l,int}$ can be obtained from the experiment. To do so, the net power output is measured for filling pressures of $6\,\mathrm{bar}$, $8\,\mathrm{bar}$ and $10\,\mathrm{bar}$ and frequencies from $4\,\mathrm{Hz}$ to $12\,\mathrm{Hz}$. For

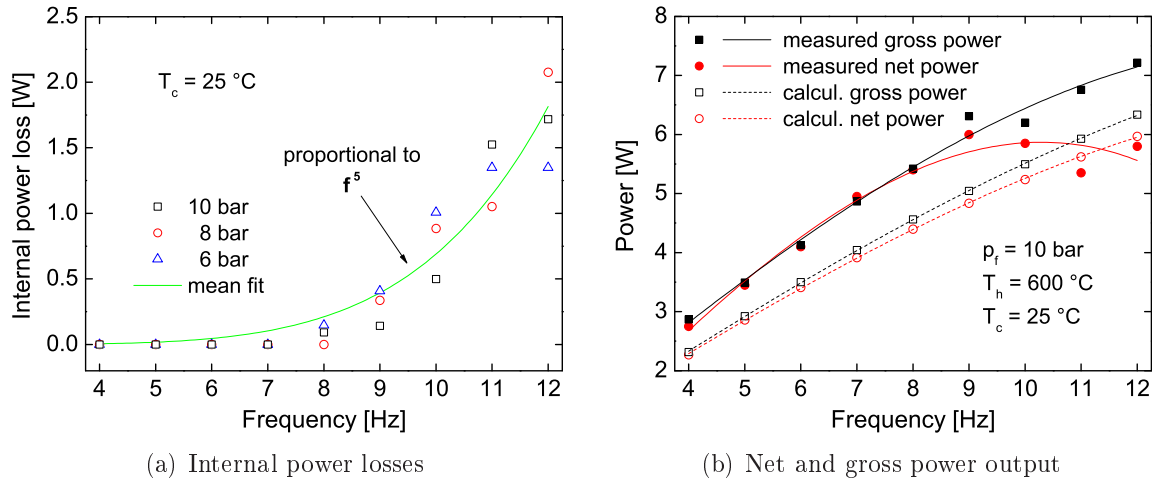(a) Measured net power output   (b) Fitted factor F
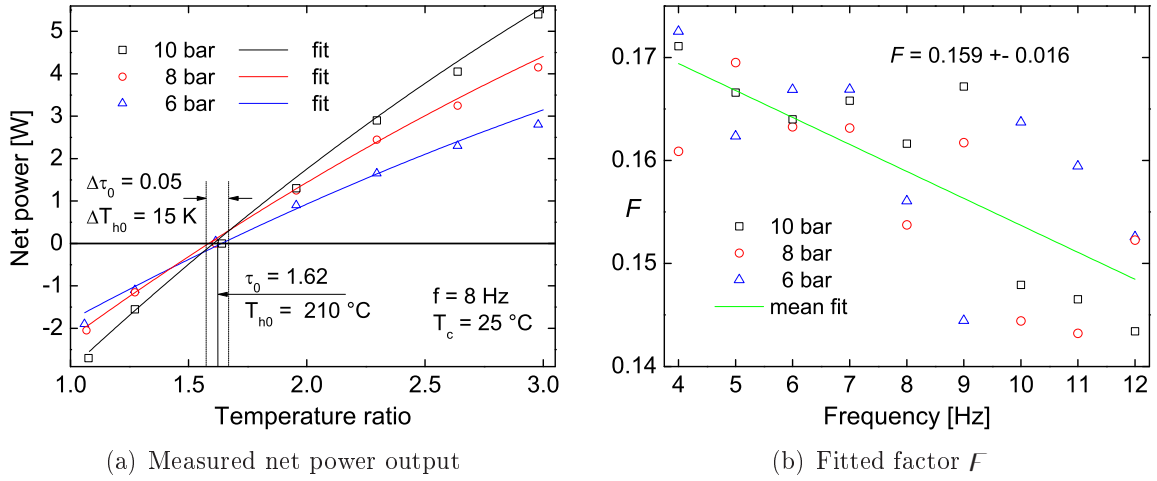
Figure 3.17: (a) Fits of the measured net power outputs as functions of the temperature ratio for filling pressures of 6 bar, 8 bar and 10 bar, an operating frequency of 8 Hz, and $T_c = 25\,°C$; (b) Factor F obtained from the fit as a function of the operating frequency.

each pair of (f, p_f) the engine is motored at heat input temperatures between $40\,°C$ and $600\,°C$. The minimum pressure is considered to be independent of the temperature distribution. In reality, due to the thermal relaxation, the temperature distribution slightly influences the minimum pressure and the pressure amplitude. From Fig. 3.8, the experimentally observed minimum pressures are $p_{min} = 5.15$ bar for a filling pressure of 6 bar, $p_{min} = 7.00$ bar for a filling pressure of 8 bar and $p_{min} = 8.55$ bar for a filling pressure of 10 bar.

The measured net power P_n is plotted versus the temperature ratio $\tau = T_h/T_c$ and adapted with Eq. (3.17). The fitting parameters are F and $P_{l,int}$. For $f = 8$ Hz the result is shown in Fig. 3.17 (a). For all filling pressures the net power becomes zero at $\tau = 1.62 \pm 0.05$. The respective minimal heat input temperature above which the engine is working is $T_h = 210\,°C \pm 15$ K. A relation for the minimal temperature ratio above which the engine provides a gross power output was found in subsection 2.3.4, Eq. (2.81) with

$$\tau_0 = \frac{r_d + 1}{r_d}.$$

The distribution ratio of the engine is $r_d = 1.71$ and thus $\tau_0 = 1.59$. This value is within the range of the experimentally observed value and differs from the measured mean value about 2%! The result is highly interesting, since simplifications such as isothermal compression and expansion were made for the analytical approach. It seems that the property of the pulse tube engine to have the calculated and measured minimal temperature ratio τ_0 is a fundamental characteristic of the engine. The analytical model is robust enough to detect this property exactly. Furthermore, the model predicts that the minimal temperature ratio is only a function of the distribution ratio. At least for

(a) Internal power losses

(b) Net and gross power output

Figure 3.18: (a) Internal power losses as functions of the operating frequency for filling pressures of 6 bar, 8 bar and 10 bar. The internal power loss is obtained from the fit of the measured net power in Fig. 3.17 (a) with Eq. (3.17); (b) Comparison of the measured net and gross power outputs with the numerically calculated net power output and the numerically calculated flow-frictionless power output as functions of the operating frequency for a filling pressures of 10 bar, a heat input temperature of 600 °C, and a cooling temperature of 25 °C.

a variable filling pressure, the experiment confirms this result.

For all investigated filling pressures and frequencies, the fitted factor F is shown in Fig. 3.17 (b). It seems to be slightly dependent on the operating frequency. The function $F(r_c)$ is assumed to be only a function of r_c. Thus, the observed slight dependency on the operating frequency has to be taken into account or is just a systematic error of the experiment. Its mean value is $< F > = 0.159$ and its absolute and relative errors are $\Delta F = 0.016$ and $\Delta F / F = 10\%$, respectively.

The results disclose that the engine's gross power output is quite equal to its net power output. To show this, the internal power loss, also obtained from the fitting procedure, is plotted in Fig. 3.18 (a). Up to an operating frequency of about 8 Hz the internal power loss is very low (< 0.5 W). After exceeding this frequency it is increasing heavily. Fitting the internal power loss with the function $P_{l,int} = c_l\,f^l$ delivers an exponent of $l \approx 5$. Mechanical power loss due to deformation of the regenerator mesh is proportional to f and flow friction power loss is proportional to f^3. Thus, the observed internal power loss does not have its origin in mechanical or flow friction. The thermodynamic situation in the engine seems to change for higher frequencies, leading to the observed strong increase of the internal power loss.

For a heat input temperature of $T_h = 600$ °C and a filling pressure of 10 bar the measured net and gross power outputs are compared with the numerical calculated net and gross power outputs. In order to calculate the gross power output with the numerical model, the flow friction is switched off in the simulation. The results, fitted

with the function $P_g = c_0 + c_1\,f + c_3\,f^3$, are shown in Fig. 3.18 (b). The measured power outputs are slightly higher than the calculated. The difference between the gross and net power output is for calculation and experiment up to a frequency of 8 Hz small. Thus, the internal power loss is small for calculation and experiment. At higher frequencies, the difference between gross and net power output in the experiment is more distinct. The numerical simulation model does not reproduce the internal power loss sufficiently for higher frequencies.

(a) Gross power output for $p_f = 10\,\mathrm{bar}$ (b) Gross power output for $T_h = 600\,^{\circ}\mathrm{C}$
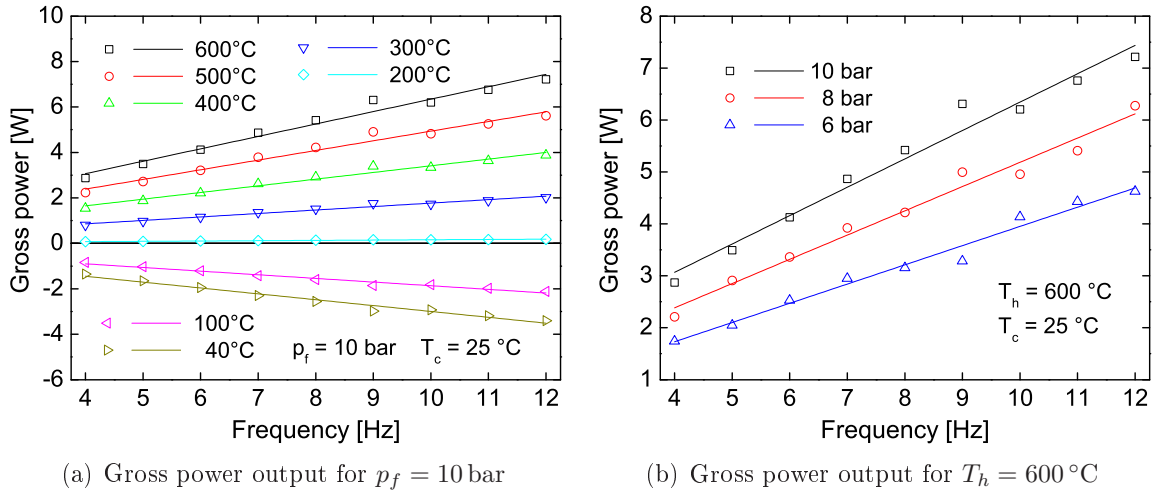
Figure 3.19: (a) Measured gross power outputs as functions of the operating frequency at a filling pressure of 10 bar and heat input temperatures between 40 °C and 600 °C; (b) Measured gross power outputs as functions of the operating frequency at a heat input temperature of 600 °C and filling pressures of 6 bar, 8 bar and 10 bar. The cooling temperature is 25 °C.

In Fig. 3.19, the measured gross power output is shown as a function of the operating frequency, for (a) a fixed filling pressure of 10 bar and heat input temperatures between 40 °C and 600 °C, and for (b) a fixed heat input temperature of 600 °C and filling pressures of 6 bar, 8 bar and 10 bar. In all cases, the observed gross power output increases ($T_h > 200\,^{\circ}\mathrm{C}$), respectively decreases ($T_h < 200\,^{\circ}\mathrm{C}$), linearly with the operating frequency. This is in accordance with the theory. As can be seen in Fig. 3.19 (a), the engine starts to operate for a heat input temperature above 200 °C, which happens at the theoretically predicted value of $\tau_0 = 1.59$. For lower heat input temperatures the engine does not function. In this case heat is just transported from the hot to the cold heat exchanger without any cycle energy conversion, respectively without any pV-work output. As predicted by the theory, the gross power increases with the heat input temperature.

Referring to Fig. 3.19 (b), it is evident that − within the range of the measurement uncertainty − the gross power output increases linearly with the filling pressure. The analytical model predicts a linear dependency of the gross power output on the minimum

engine pressure, and hence, a linear dependency of the gross power output on the filling pressure.

In order to analyze the gross efficiency of the pulse tube engine the numerical simulation model is used to calculate the thermal power input of the engine for a filling pressure of 10 bar, frequencies between 4 Hz and 12 Hz and heat input temperatures of 200 °C, 300 °C, 400 °C, 500 °C and 600 °C. The results are used to calculate the gross efficiency of the pulse tube engine from the ratio of the measured gross power of Fig. 3.19 (a) to the respective numerically calculated thermal power input.
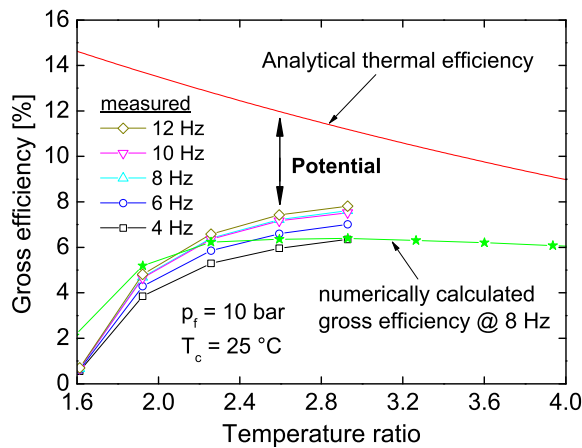
Figure 3.20: Comparison of the measured gross efficiency for frequencies between 4 Hz and 12 Hz with the analytical thermal efficiency, calculated with Eq. (2.120) and (2.122), and the gross efficiency, calculated with the numerical model, as functions of the temperature ratio τ. The measured efficiencies are available up to a heat input temperature of 600 °C. To show the existence of a peak efficiency in τ, the efficiency is calculated numerically up to a heat input temperature of 1000 °C. The filling pressure is 10 bar and the cooling temperature is 25 °C.

The results and also the efficiency potential of the pulse tube engine are shown in Fig. 3.20. The analytical thermal efficiency, calculated in subsection 2.3.6 with Eq. (2.120) and (2.122), is an upper limit of the efficiency of the pulse tube engine. It is highest for $\tau = \tau_0$ and decreases linearly with an increase of τ. The measured gross efficiency of the working pulse tube engine does not show this behavior. It is zero for $\tau = \tau_0$ and increases with an increase of τ. Since the gross efficiency cannot exceed the analytical (ideal) thermal efficiency it has to decrease above a certain temperature ratio τ_{opt}, which is too high for an experimental investigation. To show the existence of τ_{opt} the numerical simulation model is used. The pulse tube engine is simulated for heat input temperatures up to 1000 °C ($\tau = 4.27$) and the gross efficiency is calculated numerically. The result is also shown in Fig. 3.20. The numerically calculated gross efficiency reaches its peak value at about $\tau_{opt} \approx 3$. For higher temperature ratios, the gross efficiency decreases slowly. Further numerical calculations for higher temperature ratios show that the numerically calculated gross efficiency does never reach the value of the analytical thermal efficiency. For a heat input temperature of 1500 °C ($\tau = 5.95$) the numerically calculated gross efficiency is with 5.5% smaller than the analytical thermal efficiency of 5.8%. At $\tau = \tau_0$ the numerically calculated gross efficiency is 2%. This

indicates the existence of a finite efficiency at $\tau = \tau_0$ as predicted by the analytical model. The power output of the working engine for $\tau \to \tau_0$ is too small to allow an experimental determination of the respective efficiency.

For the working engine the gross efficiency increases with higher operating frequencies. The reason is the increase of the phase delay between pressure swing and heat flux in the pulse tube (thermal lag). For higher frequencies the time at which heat is added to the gas and removed from the gas in the pulse tube gets closer to TDC and BDC, respectively. The amount of heat transferred due to thermal relaxation in the pulse tube increases and the cycle gets closer to the theoretical cycle described in section 2.3.

## 3.6 Experimental design parameter studies

Section 2.5 and 2.9 show theoretically that the engine performance strongly depends on the compression ratio and the distribution ratio. The theoretical predictions are now investigated experimentally and compared to the results of the analytical and the numerical model. Moreover, as claimed in subsection 3.1.1, the cold heat exchanger chx_1 needs a certain heat transfer area to allow optimal engine operation. To proof this experimentally the influence of the heat transfer area of chx_1 on the engine performance is studied.

For all considerations the model calibration (see subsection 3.3.3) is kept at the values of the engine geometry investigated in section 3.4 and 3.5. Thus, the calculated values will differ quantitatively from the experimental observations. Nevertheless, the tendency of the performance by changing the engine geometry can be reproduced by the model as well.

3.6.1 Influence of the compression ratio

The influence of the compression ratio on the engine performance is investigated experimentally and compared to the theoretical predictions.

To do so the engine is motored at piston strokes between 20 mm and 60 mm. Fig. 3.21 (a) shows the resulting measured net power outputs for operating frequencies between 4 Hz and 12 Hz at a heat input temperature of 600 °C and a filling pressure of 12 bar. The highest values are observed for a stroke of 60 mm. With the experimental set-up, power outputs at higher strokes can not be measured reliably. A comparison of the measured and numerically calculated net power outputs depending on the compression ratio is shown in Fig. 3.21 (b). In this case the operating frequency of the engine is 8 Hz, which is slightly lower than the peak frequency of the net power output. Observation and calculation show an increasing net power for higher compression ratios. Thus,

(a) Measured net power output

(b) Calculated and measured net power output
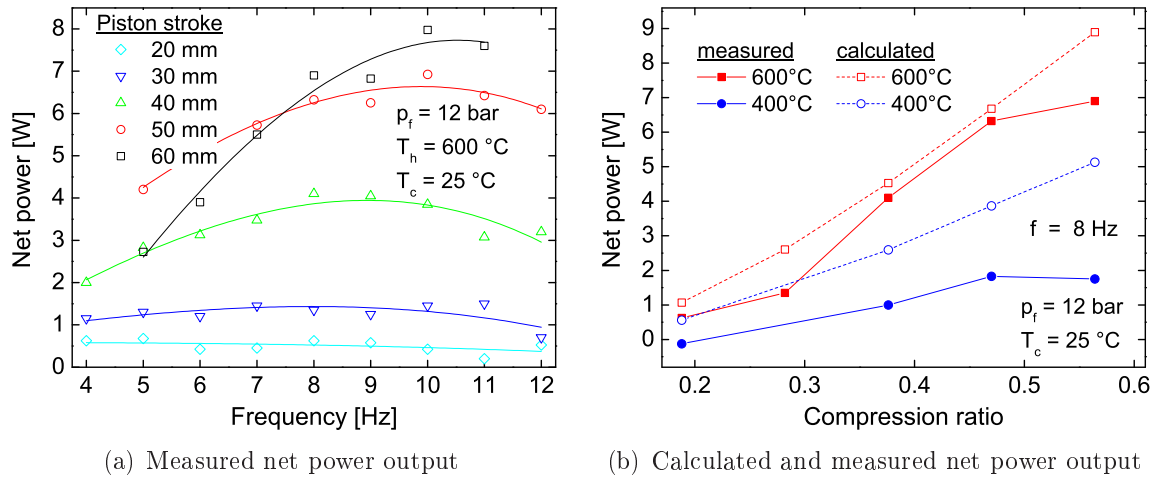
Figure 3.21: (a) Measured net power output as a function of the operating frequency for piston strokes between 20 mm and 60 mm at a heat input temperature of 600 °C and a filling pressure of 12 bar; (b) Comparison of the calculated and measured net power outputs as functions of the compression ratio for heat input temperatures of 400 °C and 600 °C, and a filling pressure of 12 bar. The cooling temperature is 25 °C.

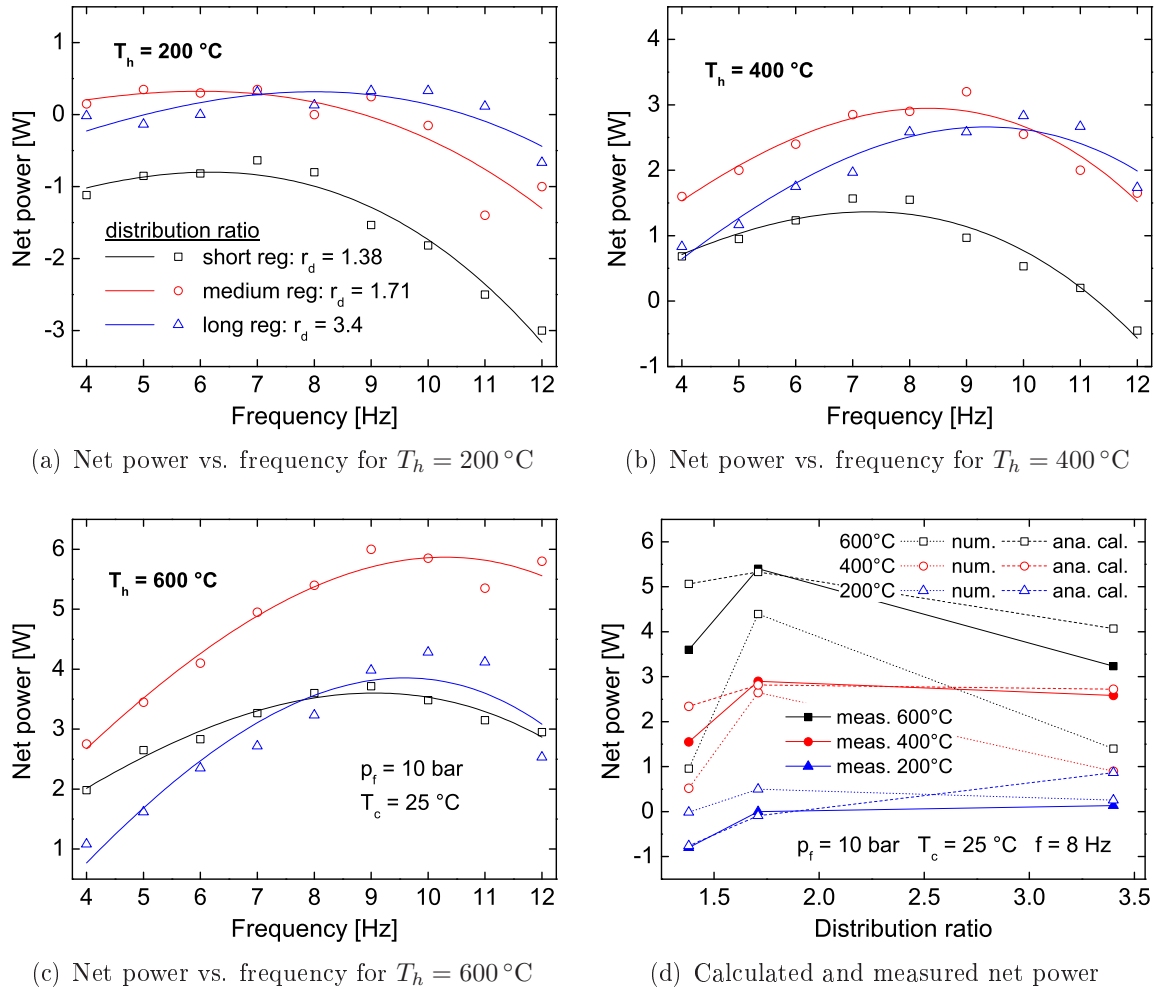on a qualitative basis, the numerical model reproduces the observed engine behavior well. For $T_h = 400$ °C the mismatch between calculation and observation is higher due to lower power outputs and thus a stronger influence of the modeling error. The experiment shows an optimal compression ratio of 0.47 (50 mm stroke) for $T_h = 400$ °C and an optimal compression ratio of 0.56 (60 mm stroke) for $T_h = 600$ °C. This observation is in accordance with the theoretical prediction, which claims that higher heat input temperatures enable higher compression ratios and higher power outputs.

3.6.2   Influence of the distribution ratio

The analytical and the numerical model disclose that the distribution ratio strongly influences the engine performance. Its influence on the engine's net power output is investigated experimentally and compared to the analytically and numerically calculated power outputs.

To study the influence of the distribution ratio experimentally three regenerators with lengths of 111 mm, 122 mm and 143 mm are manufactured and placed into the 230 mm long stainless steel tube. The resulting lengths of the pulse tube are 76 mm, 68 mm and 44 mm. The version with the 122 mm long regenerator has a 3 mm longer chx$_1$, compared to the two other regenerator versions. The extension just increases the pulse tube length for about 3 mm. With these dimensions of pulse tube and regenerator the distribution ratios are $r_d = 1.38$ (short regenerator), $r_d = 1.71$ (medium regenerator) and $r_d = 3.4$ (long regenerator). The volume of chx$_1$ is added to the pulse tube volume

and the volumes of hhx and chx_2 are added to the regenerator volume. For the motored engine the measured net power outputs at heat input temperatures of $200\,°C$, $400\,°C$ and $600\,°C$ are shown in Fig. 3.22 (a-c). For all temperatures the short regenerator always

(a) Net power vs. frequency for $T_h = 200\,°C$

(b) Net power vs. frequency for $T_h = 400\,°C$

(c) Net power vs. frequency for $T_h = 600\,°C$

(d) Calculated and measured net power

Figure 3.22: (a-c) Measured net power outputs as functions of the operating frequency for distribution ratios of 1.38, 1.71 and 3.4, heat input temperatures of $200\,°C$, $400\,°C$ and $600\,°C$, and a filling pressure of $10\,bar$; (d) Comparison of the numerically and analytically calculated net power output with the measured net power output as functions of the distribution ratio for heat input temperatures of $200\,°C$, $400\,°C$ and $600\,°C$, a filling pressure of $10\,bar$, and a frequency of $8\,Hz$. The cooling temperature is $25\,°C$.

leads to the lowest power outputs. At $T_h = 400\,°C$ the medium and the long regenerator show comparable power outputs. For lower temperatures the long regenerator becomes advantageous and for higher temperatures the medium regenerator is favored. An ideal engine having a high value of r_d (long regenerator) has a high thermodynamic asymmetry and is according to subsection 2.9.2 operating best. In the real engine the long regenerator is accompanied by a short pulse tube. Thus, the hot heat exchanger

is closer to the cold heat exchanger. A higher portion of the applied thermal power flows directly to chx_1 and is released unused. This power loss increases for higher heat input temperatures and leads to the observed better engine performance with a medium regenerator length.

In Fig. 3.22 (d), the measured net power outputs depending on the distribution ratio for an operating frequency of 8 Hz are compared to the calculated predictions of the numerical and the analytical model. According to subsection 3.5.4, at this frequency, the difference between the gross and net power output is small, and the results of the analytical model can be compared to the results of the numerical model and the experiment. For all temperatures the numerical calculations predict a stronger dependency of the net power on the distribution ratio than the experiment, whereas the analytical calculations predict a lower dependency of the net power on the distribution ratio than the experiment. The best match is reached for the medium size regenerator. The models were calibrated for this case. Nevertheless, the existence of an optimal distribution ratio is evident from measurement and calculations. Both models can thus be used to design a working pulse tube engine.

3.6.3   Heat transfer rate of the cold heat exchanger

As found by numerical calculations, the heat transfer rate in the cold heat exchanger chx_1 influences the performance of the engine in the way that an optimal heat transfer rate exists at which the engine is operating best. Details are given in Appendix **E**. To confirm this experimentally, the heat transfer area of chx_1 is modified in the experiment and the performance of the engine is measured. Three cold heat exchangers are manufactured with heat transfer areas of $56\,cm^2$, $112\,cm^2$ and $163\,cm^2$. For $T_h = 400\,°C$ the measured net power output as well as the measured net efficiency are shown in Fig. 3.23 (a, b).

At frequencies lower than 8 Hz the influence of the heat transfer area of chx_1 on the engine performance is small. At higher operating frequencies the heat exchanger with an area of $112\,cm^2$ delivers best performance results.

The observation shows the importance of a careful design of the cold heat exchanger. In contrast to Stirling engines a maximized heat transfer capability does not lead to the highest performance of the pulse tube engine.

(a) Net power output
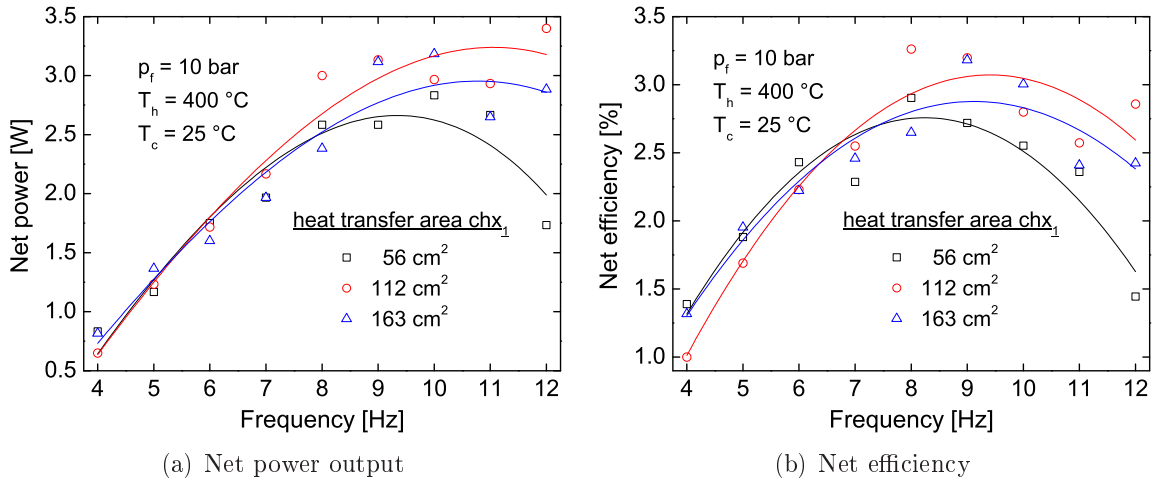
(b) Net efficiency

Figure 3.23: (a) Measured net power output; and (b) net efficiency as functions of the operating frequency for heat transfer areas of chx_1 of $56\,cm^2$, $112\,cm^2$ and $163\,cm^2$ at a filling pressure of $10\,bar$, a heat input temperature of $400\,°C$, and a cooling temperature of $25\,°C$.

Summarizing, a working pulse tube engine was successfully designed, manufactured and built at a laboratory scale. Its performance is in the projected range of several watts. Power output, efficiency and loss mechanisms were quantified and compared to the theoretical predictions leading to a profound understanding of the pulse tube engine and practical criteria for its design. The experimental set-up can be used for further engine component tests.

3.7 Summary and conclusions of the experiments

The results of the experimentally investigated engine performance compared with the theoretical predictions are summarized as follows:

1. A pressurized working pulse tube engine using helium as working fluid is built successfully. The measured and calculated time-dependent pressure and material temperatures are compared. The power loss of the thermal power input to the surroundings and the mechanical friction power loss in the cylinder and the crank mechanism are quantified. For the working engine it is shown that the heat flux in the pulse tube is out of phase with all other heat fluxes.

2. The shaft, net and gross power output as well as the shaft, net and gross efficiency of the engine are measured under variation of the engine filling pressure, the heat input temperature and the operating frequency. The influence of these operating conditions on the engine performance is investigated experimentally, and compared to the calculations using the numerical and the analytical model

developed in chapter 2. The accuracy of the calculated net power output of the numerical model is quantified to about 40%. The minimum error of the measured power output is 0.4 W.

3. At a filling pressure of 10 bar, a heat input temperature of 600 °C and a cooling temperature of 25 °C the working pulse tube engine has a measured maximum gross power output of 7.2 W at an operating frequency of 12 Hz and an efficiency of about 8%, as well as a measured maximum net power output of 6 W at an operating frequency of 9 Hz and an efficiency of about 7.8%. The measured maximum shaft power output of the engine is due to high friction in the crank mechanism used, 1.1 W at an operating frequency of 5.5 Hz and an efficiency of about 2%. The accuracy of all power outputs is 40%.

4. The internal power loss is quantified. Up to an operating frequency of 8 Hz, its value is very small (< 0.5 W). Exceeding this frequency, it is increasing heavily with $P_{l,int} \propto f^5$. The difference between net and gross power output up to a frequency of 8 Hz is only marginal. The inefficient nature of the pulse tube engine can probably be compensated for by its practical efficiency caused by low internal power losses at low operating frequencies and a simple timing mechanism.

5. The theoretically found minimum temperature ratio τ_0 above which the engine is working is confirmed experimentally. The measured value is pressure-independent and amounts to $\tau_0 = 1.62$ ($T_h = 210$ °C), with an absolute error of $\Delta \tau = 0.05$ ($\Delta T_h = 15$ K). The value calculated with Eq. (2.81) amounts to $\tau_0 = 1.59$ ($T_h = 201$ °C) and is thus within the error range of the measured value. The relative difference between calculation and experiment is very small at 2%. Since Eq. (2.81) is obtained from an ideal analysis of the pulse tube engine and the measurement delivers the same result, the minimal temperature ratio τ_0 seems to be a basic property of the pulse tube engine and the developed analytical model is robust enough to determine this basic engine property.

6. The gross power output of the engine is measured for different heat input temperatures and filling pressures. Its dependency on these operating conditions corresponds to the found dependencies of the pV-work in Eq. (2.157) and (2.158). The function $F(r_c)$, introduced in subsection 2.9.2 − being a constant in the investigations in section 3.5 − is quantified to $F = 0.16$. Using this value for F the gross power output can be calculated with Eq. (3.16).

7. An upper limit for the efficiency of the pulse tube engine is found in Eq. (2.120) together with Eq. (2.122). The measured and numerical calculated gross efficiency

never exceeds this limit, which is highest for $\tau = \tau_0$, and decreasing monotonously for $\tau > \tau_0$. The gross efficiency of the working engine is zero for $\tau = \tau_0$. It increases up to a certain temperature ratio τ_{opt}, which is found to be about $\tau_{opt} \approx 3$, and decreases for higher temperature ratios.

8. The dependency of the engine performance on the compression ratio is studied experimentally. With the analytical model, it is not possible to calculate the engine performance depending on the compression ratio. The numerical simulation model allows for this investigation. Under variation of the compression ratio, the numerically calculated engine performance corresponds — within the accuracy of the one-dimensional model — to the measured engine performance.

9. The dependency of the engine performance on the distribution ratio is studied experimentally. Both, the analytical and the numerical model can be used to investigate the engine performance under variation of the distribution ratio. The calculated performances are comparable to the measurements, whereas the numerical model predicts a stronger dependency of the net power on the distribution ratio than the experiment, and the analytical model predicts a lower dependency of the net power on the distribution ratio than the experiment.

10. It is shown experimentally that the heat transfer rate in the cold heat exchanger chx_1 has an optimum at which the engine is operating best. This behavior was also found by numerical simulations.

As has been shown above, the developed working pulse tube engine, in combination with the simulation models, provides a powerful tool to study the performance of the pulse tube engine for various design parameters and operating conditions.

Chapter 4

Summary and further development

In this chapter the results of the present thesis are summarized, discussed and compared to the objectives formulated in chapter 1. As a practical achievement of this work, the concept of an advanced powerful prototype-like pulse tube engine, which is currently under development, is derived.

4.1 Achieved state of knowledge

The pulse tube engine has been investigated theoretically and experimentally with respect to its usage for low temperature waste heat recovery, e.g. of internal combustion engines. In this section the results are discussed and compared to the goals formulated in subsection 1.2.2. Afterwards, conclusions of the gained results with emphasis on a further development of the pulse tube engine are conducted.

4.1.1 Results of this thesis

The state of knowledge from the beginning of this thesis has been increased by a detailed theoretical disclosure of the pulse tube engine's underlying thermodynamic process, by the formulation of mathematical relations for its power output and efficiency as well as by the definition and determination of important design features resulting in a successful realization of a working engine.

Two mathematical models were formulated and their results compared to the measured characteristics of the working pulse tube engine. The first, an idealized analytical model, presented in section 2.3 was aimed to discover fundamental characteristics of the pulse tube engine and to derive mathematical relations for its power output and efficiency. The aim of the second, numerical model, presented in section 2.7, was to get a more precise understanding of the pulse tube engine's underlying energy conversion process and the influence of design features on the engine performance.

The results of the theoretical analysis of the engine in chapter 2 were used in chapter 3 to design and build a pressurized working engine at a laboratory scale having several watts of power output. The experimental test engine, equipped with a high number of temperature and pressure sensors as well as measurement techniques for heat power input and mechanical power output, was used to quantify the accuracy of the developed simulation models and to systematically compare the performance of this engine with the theoretical predictions. Furthermore, design parameter studies were performed experimentally to support the development of an advanced powerful pulse tube engine.

Using the analytical model, it was proven mathematically in subsection 2.4.2 that the pulse tube engine is intrinsically irreversible. This supposition was formulated in [40], since the pulse tube engine process is similar to the thermoacoustic standing wave engine, which is intrinsically irreversible as well [46]. Moreover, the intrinsically irreversible nature of the pulse tube engine leads to a minimal temperature ratio $\tau_0 > 1$, derived in subsection 2.3.4, above which the engine starts to operate as a prime mover. Its value was derived from the analytical model to be $\tau_0 = (r_d + 1)/r_d$ — only dependent on the distribution ratio, defined in section 2.2. The theoretically predicted value of τ_0 was experimentally confirmed in subsection 3.5.4 with an accuracy of 2%.

With the analytical model relations for the ideal power output and the ideal thermal efficiency were derived in subsection 2.3.6. The resulting equations of the analytical model were enhanced in subsection 2.9.2 by the numerically found strong influence of the compression ratio on the engine performance. The accuracy of the formulated analytical relations for the power output and efficiency were investigated experimentally in subsection 3.5.4. It was found theoretically in subsection 2.4.2 that the pulse tube engine's ideal thermal efficiency is highest for a temperature ratio equal to τ_0 and is decreasing monotonously for an increase of the temperature ratio. The experimental test engine delivers a gross efficiency being equal to zero for a temperature ratio equal to τ_0, followed by an increase of the gross efficiency up to a temperature ratio of about $\tau \approx 3$, followed by a numerically calculated decrease of the gross efficiency for higher temperature ratios. This result is discussed in subsection 3.5.4, where numerical investigations up to a temperature ratio of about $\tau = 6$ ($T_h = 1500\,°C$) were performed. The numerically calculated and measured gross efficiency are always below the thermal efficiency calculated with the analytical model. Thus, the derived relation for the thermal efficiency in subsection 2.3.6, which relates the thermal efficiency to design parameters and working gas properties is an upper bound for the efficiency of the pulse tube engine.

The analytical model discloses that — for the ideal engine — the heat converted into pV-work is added to the working gas in the cylinder only. The entire heat delivered to the working gas in the hot heat exchanger and in the pulse tube is rejected in the

cold heat exchanger. This effect − also calculated numerically in subsection 2.9.1 and observed qualitatively at the working engine − enables a pulse tube engine with a non-isothermal cylinder to provide a cooling power. The pulse tube engine can thus act as a thermal driven refrigerator, which absorbs heat in the cylinder and converts it into pV-work. An application for a respective German patent [82] of a thermal driven refrigerator has been made within the framework of this thesis.

The numerical model was successfully used to calculate the non-ideal cycle of the pulse tube engine. The results are presented in subsection 2.9.1. It has been discovered that the underlying working principle of the pulse tube engine is not only the supposed thermal relaxation [24] in the pulse tube, it is more a broken thermodynamic symmetry. Thermodynamic asymmetry results from the fluidic linkage of an adiabatic space (pulse tube) with an isothermal space (regenerator). Thus, the regenerator of the pulse tube engine is essential for its functioning. The thermodynamic asymmetry can be maximized by the correct distribution ratio. Maximum power output is reached for higher, and maximum efficiency for lower distribution ratios. These observations resulting from the numerical model are in accordance with the analytically derived equations in subsection 2.3.6 and with the experimental observations in subsection 3.6.2.

In contrast to the claimed necessity [24] of a non-adiabatic pulse tube, enabling a thermal relaxation or thermal lag [27, 28, 29], a pulse tube engine having a perfect adiabatic pulse tube is able to provide a power output, but not an engine having no regenerator. This is proven in subsection 2.9.4. There, it is also shown, that the thermal lag effect in the pulse tube supports the energy conversion process and increases the efficiency of the engine. Maximum efficiency is obtained for a specific amount of heat transferred between the pulse tube material and the working gas. The pulse tube has thus a regenerative property, which is bound on well adjusted heat transfer conditions.

Moreover, the operating and design parameters temperature ratio, compression ratio and distribution ratio, introduced in section 2.2, are well suited to describe the influence of the operating conditions and design features on the engine performance. This was observed analytically in subsection 2.5, numerically in the subsections 2.9.2 and 2.9.3, and experimentally in section 3.6. Especially the distribution ratio highly influences the engine performance. The higher the distribution ratio, the lower the minimal temperature ratio τ_0, above which the engine is working and the higher its power output, but the lower the achieved efficiency. The pV-work output of the engine is maximal for a certain distribution ratio, which was estimated in subsection 2.5.3 to $r_{d,opt} \approx (\tau + 1)/(\tau - 1)$.

As a very practical disclosure of this research, it was found that a specially designed pulse tube engine is able to take on heat along the pulse tube having the temperature

distribution shown in Fig. 1.2 of subsection 1.2.1. Hence, heat can be added to the working gas at a continuously decreasing temperature between T_h and T_c along the pulse tube. This property of the pulse tube engine — only dependent on its design — was found in the subsections 2.3.4, 2.9.1 and 3.3.4. Thus, the pulse tube engine is able to use heat sources at different temperature levels. It is possible to design a pulse tube engine, which cools down a fluid beginning at the hot heat exchanger temperature, along the pulse tube to the cold heat exchanger temperature. This allows for the absorption of a larger amount of heat from a thermal energy carrying fluid compared to e.g. the Stirling engine, which is due to the regenerative cycle only able to use heat at a small temperature range.

The shaft, net and gross power output as well as the shaft, net and gross efficiency of the developed working pulse tube engine were measured in section 3.5 under variation of the engine filling pressure, the heat input temperature and the operating frequency. The results were compared with the theoretical predictions. According to subsection 3.5.3, the relative difference in the numerically calculated and measured net power outputs is for $T_h \geq 400\,°\mathrm{C}$ smaller than 40%. The measured maximum power outputs of the laboratory-scale working engine having a filling pressure of 10 bar, a heat input temperature of 600 °C and a cooling temperature of 25 °C are: 7.2 W at an operating frequency of 12 Hz and an efficiency of about 8% for the gross power, 6 W at an operating frequency of 9 Hz and an efficiency of about 7.8% for the net power, and 1.1 W at an operating frequency of 5.5 Hz and an efficiency of about 1.2% for the shaft power.

The measured internal power loss is, up to an operating frequency of 8 Hz, with a value of about 0.5 W, very small. Exceeding this frequency it is increasing heavily proportional to f^5. Thus, gross power and net power are comparable for low operating frequencies. This is an advantage of the pulse tube engine, which is related to its simplicity. The main power loss of the built working engine results from external power losses in the crank shaft, which can be reduced by a more efficient crank shaft mechanism or the use of a linear electrical alternator.

In future research, the gained knowledge about the pulse tube engine as well as the developed theoretical and experimental tools can be used symbiotically to further develop this kind of prime mover.

The two prospected main goals of this thesis, formulated in subsection 1.2.2, concerning a deep understanding of the pulse tube engine's underlying thermodynamic processes and the successful development of a working engine within the projected power range have been achieved. The results of this thesis were brought to the international scientific community via three publications in international referred journals [83, 84, 85]. A fourth publication about the results of the analytical model is submitted

to Energy [86]. Furthermore, three German patent applications [82, 87, 88] have been submitted. The results of this research were discussed on national and international conferences and workshops [89, 90, 91, 92, 93, 94, 95].

4.1.2 Conclusions from this thesis

The overall aim of this thesis was to quantify the potential of the pulse tube engine for its usage in internal combustion engine's waste heat recovery and to provide general characteristics of the pulse tube engine, which could be interesting for other applications as well.

Theory and experiment show that the pulse tube engine is able to operate at heat input temperatures present in the exhaust gas of internal combustion engines. Even if its prospected efficiency is with a value under 10% comparably low, its simplicity and especially its ability to use heat along the pulse tube from a heat source continuously decreasing in temperature, a practically operating pulse tube engine can recover a large amount of heat from the exhaust gas of an internal combustion engine. This is an important advantage of a well designed pulse tube engine. As an example, existing thermoelectric energy converters [3] are able to recover heat from the exhaust gas in a temperature range of about 100 K. The exhaust gas enters the thermoelectric energy converter at a temperature of about 400 °C and exits it at about 300 °C. A well designed pulse tube engine, in contrast, would be able to recover heat from the exhaust gas beginning at the heat input temperature of 400 °C theoretically down to the temperature of the cold heat exchanger. Assuming that the exhaust gas leaves the pulse tube engine at a temperature of 200 °C, the amount of heat recovered from the exhaust gas is twice as much as the amount of heat recovered by the respective thermoelectric energy converter. Supposing that the pulse tube engine and the thermoelectric energy converter have comparable thermal efficiencies, the practical efficiency of the pulse tube engine is thus twice as much as that of the thermoelectric energy converter. Moreover, in contrast to state of the art thermoelectric energy converters, the pulse tube engine operates reliably at heat input temperatures higher than 400 °C.

Since the mechanical design of the pulse tube engine is very simple and heat is provided from external heat sources, it can be used in a wide range of other waste heat recovery applications as well. A utilization as a low noise electrical power source or as a thermal driver refrigerator is also possible. The remaining research and development challenge, necessary to provide a breakthrough of the pulse tube engine in waste heat recovery, is to find an efficient and economic mechanism for the conversion of the produced net power into shaft power or electricity. A first approach to meet this challenge is briefly described in the last section of this thesis.

4.2 Concept of an advanced pulse tube engine

Based on the theoretical and experimental results, the design of an advanced powerful prototype-like pulse tube engine is proposed. Optimal design features concerning the distribution ratio and the heat transfer conditions in the pulse tube are used to build up an engine having a comparatively high efficiency at a low heat input temperature. The conversion of the produced pV-power into electrical power is done by a linear electrical alternator, developed in [96].

Fig. 4.1 shows the conceptional design of the engine. The linear electrical alternator
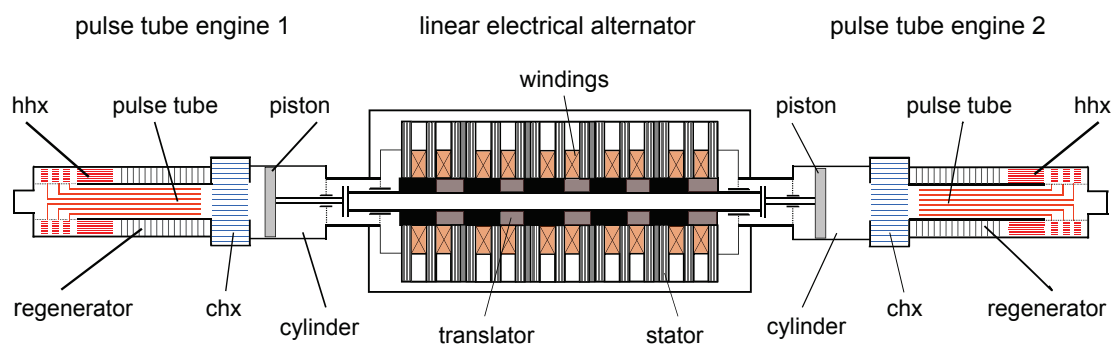
Figure 4.1: Design of the advanced powerful prototype-like pulse tube engine consisting of two coaxial pulse tube engines and a linear electrical alternator, designed as a reluctance machine. The encapsulated engine design enables a high filling pressure up to 50 bar. The coaxial configuration facilitates heat input and cooling, and increases the engine efficiency.

is designed as a reluctance machine [96, 97] having a stator consisting of magnets and magnetic conductive iron material as well as electrical coils. The translator consist only partly of magnetic conductive iron material. Details concerning the design and the functional principle of the linear electrical alternator are given in [97, 98].

At both sides of the linear electrical alternator two equal pulse tube engines in a coaxial configuration are installed. The used cylinder is an AIRPEL Anti-Stiction air cylinder, similar to the one used in the previously built engine of chapter 3. Since the engine is operating as a free piston engine (see subsection 2.9.1), the stroke varies between 0 and 40 mm. Compression/expansion energy is stored as kinetic energy of the translator. The cylinder is fluidically linked with the cold heat exchanger, which is fluidically linked with the pulse tube's cold side. At the pulse tube's hot side a specially designed hot heat exchanger is located, enabling a fluidic linkage between the hot side of the pulse tube and the hot side of the regenerator, placed coaxial around the pulse tube. The cold side of the regenerator is thermally contacted to the cold heat exchanger material. In the pulse tube, three coaxial metal tubes are placed to adjust the heat transfer area of the pulse tube.
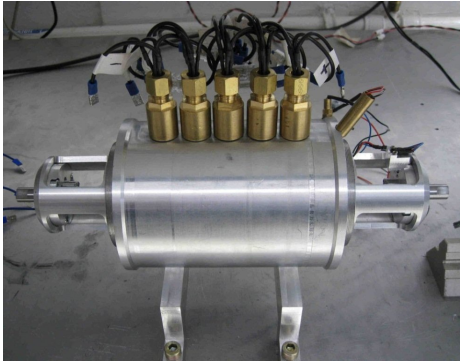
Figure 4.2: Photograph of the current state of the art of the advanced pulse tube engine. The photograph shows the built and tested linear electrical alternator with the flanges for the two coaxial pulse tube engines. It is a result of the Master thesis of Holtmann [96].

The coaxial design of the pulse tube engine has two advantages. First, the two cold heat exchangers of the basic engine shown in Fig. 1.2 of subsection 1.2.1 are substituted by one cold heat exchanger. This facilitates an application of the engine, since the cold heat exchangers of both sides can be cooled together with the linear electrical alternator. On the other hand, the heat supply at the front sides of the engine facilitates a connection to the heat source. Secondly, the coaxial thermal coupling of pulse tube and regenerator enables the exchange of heat between both components [99, 100], which increases the engine efficiency [101].

The entire system, consisting of the linear electrical alternator and the two coaxial pulse tube engines is encapsulated enabling a filling pressure up to 50 bar. The prospected net power output of the two engines is calculated to be 70 W at a filling pressure of 40 bar, a heat input temperature of 300 °C, a cooling temperature of 25 °C and an operating frequency of 30 Hz. The net efficiency at these conditions is calculated to 8%. The linear electrical alternator is designed to have a conversion efficiency of mechanical power into electrical power of about 80%. Thus, the prospected electrical power output of the engine having the mentioned operating conditions shall be around 50 W at an overall efficiency of about 6%.

The linear electrical alternator is designed and built up. First performances measurements are done and presented in [96]. All thermal components are designed and currently in the phase of manufacturing and assembling. A photograph of the existing engine parts, mainly concerning the linear electrical alternator, is shown Fig. 4.2. The engine will be used to demonstrate the feasibility of a powerful low temperature pulse tube engine backing its path into an application. First tests are scheduled for the next couple of month *and shall be in accordance with the following words of the German, Swiss and American physicist Albert Einstein:*

"Das Schönste und Tiefste was der Mensch erleben kann ist das Gefühl des Geheimnisvollen."

Appendix

T: Theory

− **Maple outputs of the analytical model** −

Series expansion of the compression/expansion work:

$$
\begin{aligned}
W_{pV} = &-\frac{V_d\, p_{\min}\, (\tau - \tau_0)}{(r_d + 1)\, \tau_0} \\
&+ \frac{1}{2}\, \frac{\left(r_c\tau_0{}^2 + 2\, r_c r_d \tau_0 + 2\, r_c \tau_0 + 2\, r_c r_d + r_c + 4\, r_d\right) V_d\, p_{\min}\, (\tau - \tau_0)^2}{(1 + \tau_0)\, (r_c r_d \tau_0 + r_c \tau_0 + 2\, r_d + r_c r_d + r_c + 2)\, \tau_0{}^2\, (r_d + 1)} \\
&- \frac{1}{3}\, \left(...^{*)}\right) (\tau - \tau_0)^3 \\
&+ O\left((\tau - \tau_0)^4\right)
\end{aligned}
$$

$^{*)}$ positive constant term

Series expansion of the amount of heat transferred per cycle in the cylinder:

$$
\begin{aligned}
Q_{cyl} = &\frac{V_d\, p_{\min}\, (\tau - \tau_0)}{(r_d + 1)\, \tau_0} \\
&- \frac{1}{2}\, \frac{\left(r_c\tau_0{}^2 + 2\, r_c r_d \tau_0 + 2\, r_c \tau_0 + 2\, r_c r_d + r_c + 4\, r_d\right) V_d\, p_{\min}\, (\tau - \tau_0)^2}{(1 + \tau_0)\, (r_c r_d \tau_0 + r_c \tau_0 + 2\, r_d + r_c r_d + r_c + 2)\, \tau_0{}^2\, (r_d + 1)} \\
&+ O\left((\tau - \tau_0)^3\right)
\end{aligned}
$$

Series expansion of the amount of heat transferred per cycle in the cold heat exchanger:

$$
\begin{aligned}
Q_{chx} = &-\frac{V_d\, \kappa\, p_{\min}\, (\tau - \tau_0)}{(\kappa - 1)\, \tau_0} \\
&- 2\, \frac{V_d\, \kappa\, p_{\min}\, (\tau - \tau_0)^2}{(\kappa - 1)\, (r_c r_d \tau_0 + r_c \tau_0 + 2\, r_d + r_c r_d + r_c + 2)\, \tau_0{}^2} \\
&+ O\left((\tau - \tau_0)^3\right)
\end{aligned}
$$

Series expansion of the amount of heat transferred per cycle in the pulse tube:

$$Q_{pt} = -\frac{(r_d \tau_0 - r_d - 1)\, V_d\, \kappa\, p_{\min}\, (\tau - \tau_0)}{(\kappa - 1)\, \tau_0\, (r_d + 1)}$$
$$+ \frac{1}{2}\frac{V_d\, \kappa\, p_{\min}\, (r_c{}^2 r_d \tau_0{}^3 + 4\, r_c \tau_0 - 4\, r_d \tau_0 - r_c{}^2 r_d \tau_0 + 4\, r_c r_d + 4\, r_c)\, (\tau - \tau_0)^2}{(\kappa - 1)\, r_c\, (1 + \tau_0)\, (r_c r_d \tau_0 + r_c \tau_0 + 2\, r_d + r_c r_d + r_c + 2)\, \tau_0{}^2\, (r_d + 1)}$$
$$+ O\left((\tau - \tau_0)^3\right)$$

Series expansion of the amount of heat transferred per cycle in the hot heat exchanger:

$$Q_{hhx} = \frac{V_d\, \kappa\, p_{\min}\, r_d\, (\tau - \tau_0)}{(\kappa - 1)\, (r_d + 1)}$$
$$- \frac{1}{2}\frac{V_d\, \kappa\, p_{\min}\, (r_c \tau_0 - 2 - r_c)\, r_d\, (\tau - \tau_0)^2}{r_c \tau_0\, (\kappa - 1)\, (1 + \tau_0)\, (r_d + 1)^2}$$
$$+ O\left((\tau - \tau_0)^3\right)$$

Series expansion of the amount of heat transferred per cycle in the regenerator:

$$Q_{reg} = 0$$

Series expansion of the thermal efficiency, via the hot heat exchanger only:

$$\eta_{th}^{=} = \frac{\kappa - 1}{\tau_0\, r_d\, \kappa}$$
$$- \frac{(\kappa - 1)\, (r_c{}^2 \tau_0 + r_c{}^2 r_d \tau_0 + 2\, r_c r_d + r_c{}^2 r_d + 2 + 2\, r_c + r_c{}^2)\, (\tau - \tau_0)}{\kappa\, r_c\, (1 + \tau_0)\, r_d \tau_0{}^2\, (r_d + 1)\, (r_c \tau_0 + r_c + 2)}$$
$$+ O\left((\tau - \tau_0)^2\right)$$

Series expansion of the thermal efficiency, via the hot heat exchanger and pulse tube:

$$\eta_{th}^{<} = \frac{\kappa - 1}{(r_d + 1)\, \kappa}$$
$$- \frac{1}{2}\frac{(r_c \tau_0{}^2 + 2\, r_c r_d \tau_0 + 2\, r_c \tau_0 + 4\, \tau_0 + 2\, r_c r_d + r_c + 4 + 4\, r_d)\, (\kappa - 1)\, (\tau - \tau_0)}{(r_d + 1)\, \tau_0\, (1 + \tau_0)\, \kappa\, (r_c r_d \tau_0 + r_c \tau_0 + 2\, r_d + r_c r_d + r_c + 2)}$$
$$+ O\left((\tau - \tau_0)^2\right)$$

Entropy production in the cylinder:

$$S_{irr,cyl} = 0$$

Entropy production in the cold heat exchanger:

$$S_{irr,chx} = \frac{1}{2} \frac{V_d \, \kappa \, p_{\min} \, (\tau - \tau_0)^2}{T_c \, (\kappa - 1) \, \tau_0{}^2} + O\left((\tau - \tau_0)^3\right)$$

Entropy production in the pulse tube:

$$S_{irr,pt} = \frac{V_d \, \kappa \, p_{\min} \, (r_c \tau_0{}^2 r_d + r_c \tau_0{}^2 + 2\,r_d\tau_0 - r_c r_d - r_c - 2\,r_d)\,(\tau - \tau_0)^2}{(r_c\tau_0 + r_c + 2)\,(r_d + r_d\tau_0 + \tau_0 + 1)^2\,(\kappa - 1)\,T_c r_c \tau_0{}^2} + O\left((\tau - \tau_0)^3\right)$$

Entropy production in the hot heat exchanger:

$$S_{irr,hhx} = \frac{1}{2} \frac{V_d \, \kappa \, p_{\min} \, r_d \, (\tau - \tau_0)^2}{\tau_0{}^2 T_c \, (\kappa - 1) \, (r_d + 1)} + O\left((\tau - \tau_0)^3\right)$$

Entropy production in the regenerator:

$$S_{irr,reg} = 0$$

Sum of enthalpy exchanged between the components

$$\sum_i H_i' + \sum_i H_i'' = 0$$

Sum of entropy exchanged between the components

$$\sum_i S_i' + \sum_i S_i'' = 0$$

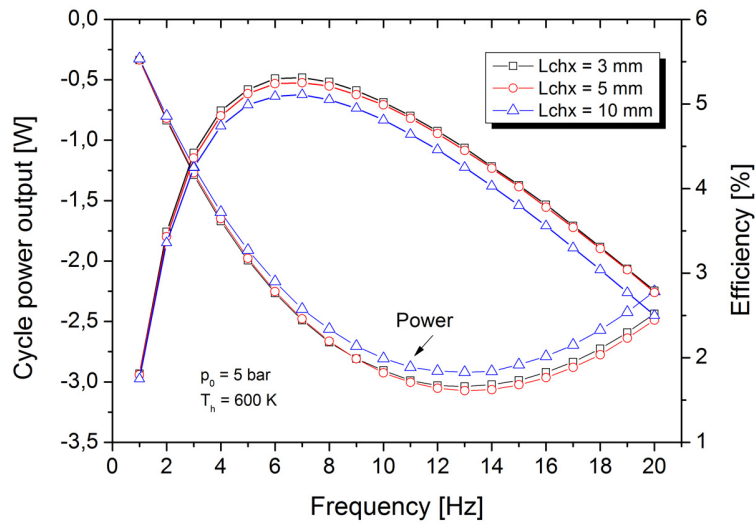**Check cycle energy balance**

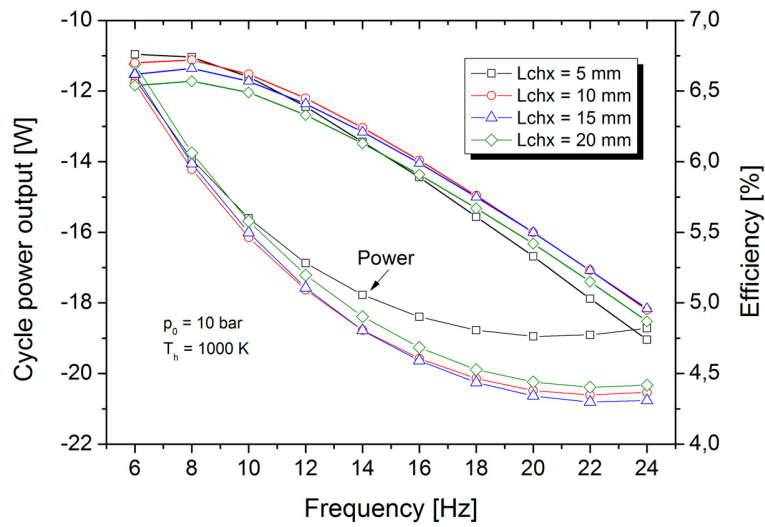$$E_{cycle} = 0$$

Check cycle entropy balance

$$S_{cycle} = 0$$

E: Experiment

− Numerical determination of the optimal cold heat exchanger area −

(a) $p_f = 5\,\mathrm{bar}$, $T_c = 300\,\mathrm{K}$, $T_h = 600\,\mathrm{K}$

(b) $p_f = 10\,\mathrm{bar}$, $T_c = 300\,\mathrm{K}$, $T_h = 1000\,\mathrm{K}$

Numerically calculated net power output and efficiency as functions of the operating frequency for different lengths L_{chx} of the cold heat exchanger chx$_1$, resulting in different heat transfer areas ($A_{hx} \propto L_{chx}$).

References

[1] V. Küntscher, *Kraftfahrzeugmotoren − Auslegung und Konstruktion.* Berlin: Verlag Technik, 1995.

[2] E. Hahne, *Technische Thermodynamik.* München: Oldenbourg Wissenschaftsverlag, 2010.

[3] L. Aixala, "Renoter project." in *Proceedings of 2nd Thermoelectric Applications Workshop, San Diego*, 2011.

[4] D. Burhorn, "Beitrag zur Konzeption eines Abwärme-Compound-Systems an Verbrennungsmotoren in Kraftfahrzeugen." *PhD Thesis, University of Hannover*, 1996.

[5] R. Freymann, J. Ringler, M. Seifert, and T. Horst, "Der Turbosteamer der zweiten Generation." *MTZ − Motortechnische Zeitschrift*, no. 12, 2012.

[6] C. Häfele and H. Friedrich, "Methodical concept development of automotive thermoelectric generators." in *Proceedings of Thermoelectric goes Automotive, Berlin*, 2012.

[7] K. T. Wojciechowski, R. Zybala, J. Tomankiewicz, P. Fuc, P. Lijewski, J. Wojciechowski, and J. Merkiszand, "Influence of back pressure on net efficiency of TEG generator mounted in the exhaust system of a Diesel engine." in *Proceedings of Thermoelectric goes Automotive, Berlin*, 2012.

[8] J. Vazaquez, M. A. Zanz-Bobia, R. Palacios, and A. Arenas, "State of the art of thermoelectric generators based on heat recovered from the exhaust gases of automobiles." in *Proceedings of the 7th European Workshop on Thermoelectrics, Pamplona*, 2002.

[9] J. Kirchner, "Verfahren zur Energiegewinnung aus dem Abgas eines Verbrennungsmotors." Patent DE 19 701 160A1, 1997.

[10] J. Larjola, A. Uusitalo, and T. Turunen-Saaresti, "Background and summary of commercial ORC development and exploitation." in *Proceedings of the 1st International Seminar on ORC Power Systems, Delft*, 2011.

[11] S. Köhler, "Geothermisch angetriebene Dampfkraftprozesse." *PhD Thesis, Technical University of Berlin*, 2005.

[12] N. Elsner and A. Dittmann, *Grundlagen der Technischen Thermodynamik, Band 1.* Berlin: Akademie − Verlag, 1993.

[13] N. N., *Antriebsenergie aus Abwärme.* Düsseldorf: VDI − Verlag, 1980.

[14] M. v. Ardenne, G. Musiol, and U. Klemradt, *Effekte der Physik und ihre Anwendungen.* Frankfurt am Main: Verlag Harri Deutsch, 2005.

[15] J. P. Dismukes, L. Ekstrom, E. F. Steigmeier, I. Kudman, and D. S. Beers, "Thermal and electrical properties of heavily doped Ge-Si alloys up to 1300 K." *Journal of Applied Physics*, vol. 35, no. 10, 1964.

[16] L. Aixala and V. Monnet, "Conclusion of renoter project: Waste heat recovery for trucks and passenger cars." in *Proceedings of Thermoelectric goes Automotive, Berlin*, 2012.

[17] Volkswagen AG Wolfsburg, 2013, personal communication.

[18] W. E. Gifford and R. C. Longsworth, "Pulse tube refrigeration process." *Advances in Cryogenic Engineering*, vol. 10, p. 69ff, 1965.

[19] M. David, J. C. Maréchal, Y. Simon, and C. Guilpin, "Theory of ideal orifice pulse tube refrigerator." *Cryogenics*, vol. 33, pp. 154–161, 1993.

[20] P. C. T. de Boehr, "Thermodynamic analysis of the basic pulse tube refrigerator." *Cryogenics*, vol. 9, pp. 699–710, 1994.

[21] G. Q. Lu and P. Cheng, "Numerical and experimental study of a Gifford-McMahon-type pulse tube refrigerator." *Journal of Thermophysics and Heat Transfer*, vol. 17, pp. 457–463, 2003.

[22] S. Masuyama, Y. H. Kim, S. J. Park, Y. J. Hong, H. B. Kim, and S. H. Lee, "Experimental research of Stirling type pulse tube refrigerator with an active phase control." *Cryogenics*, vol. 46, pp. 385–390, 2006.

[23] K. Hamaguchi, Y. Ushijima, and Y. Hiratsuka, "Basic characteristics of pulse tube engine." in *Proceedings of the 12th International Stirling Engine Conference, Durham*, 2005, pp. 275–284.

[24] A. J. Organ, *The Air Engine: Stirling Cycle Power for a Sustainable Future.* Cambridge: Woodhead Publishing, 2007.

[25] N. C. J. Chen and C. D. West, "A single-cylinder valveless heat engine." in *Proceedings of the 22nd Intersociety Energy Conversion Engineering Conference*, 1987.

[26] P. L. Tailer, "Thermal Lag Machine." Patent US 5 414 997, 1995.

[27] C. D. West, "Some single-piston closed-cycle machines and Peter Tailer's thermal lag engine." in *Proceedings of the 28th Energy Conversion Engineering Conference, Atlanta*, 1993, pp. 2673–2679.

[28] P. L. Tailer, "Thermal lag test engines evaluated and compared to equivalent Stirling engines." in *Proceedings of the 30th Energy Conversion Engineering Conference, Orlando*, 1995.

[29] F. Wicks and C. Caminero, "The Peter Tailer external combustion thermal lag piston/cylinder engine analysis and potential applications." in *DOI: 10.2514/6.1994-3987*, 1994.

[30] A. Hofmann, "Pulsrohr-Leistungsverstärker." Patent DE 10 001 460A1, 2000.

[31] K. Hamaguchi, H. Futagi, T. Yazaki, and Y. Hiratsuka, "Measurement of work generation and improvement in performance of a pulse tube engine." *Journal of Power and Energy Systems*, vol. 2, no. 5, 2008.

[32] Z. Shauwei, "Pulse tube-type heat storage engine." Patent JP 2 009 236 456A, 2009.

[33] S. Shiyoui, "Pulse tube type heat storage engine." Patent JP 2 007 192 443A, 2007.

[34] G. Kaiser and J. Klier, "Wärmekraftmaschine nach dem Pulsröhrenprinzip." Patent DE 102 008 050 653A1, 2010.

[35] A. L. W. Keen and D. Rilling, "Feasibility study of thermoacoustic lamina flow engine for waste heat regeneration in vehicles." *New Aspects of Fluid Mechanics, Heat Transfer and Environment, ISBN 978-960-474-215-8*.

[36] G. Kaiser, J. Klier, and S. Ott, "Exhaust system for motor vehicles comprising a built-in heat engine." Patent WO 2010/037 358A1, 2010.

[37] Y. Ishizaki and T. Matsui, "Pulse Tube Heat Engine." Patent US 5 435 136, 1995.

[38] T. Ki and S. Jeong, "Design and analysis of highly effective pulse tube engine." *Applied Thermal Engineering*, vol. 53, pp. 31–36, 2013.

[39] G. Kaiser, M. Kuhn, M. Schneider, J. Klier, S. Ott, and A. Lang, "Stirling-Verdampfer-Wärmekraftanlage." Patent DE 102 009 057 210A1, 2011.

[40] T. Yoshida, T. Yazaki, H. F. K. Hamaguchi, and T. Biwa, "Work flux density measurements in a pulse tube engine." *Applied Physics Letters*, vol. 95, 2009.

[41] N. Rott, "Thermoacoustics." *Advances in Applied Mechanics*, vol. 20, 1980.

[42] G. W. Swift, *Thermoacoustics: A unifying Perspective for Some Engines and Refrigerators.* New York: Acoustical Society of America, American Institute of Physics Press, 2002.

[43] T. Biwa, "Work flow measurements in a thermoacoustic engine." *Cryogenics*, vol. 41, pp. 305–310, 2001.

[44] T. Biwa, Y. Tashiro, and U. Mizutani, "Experimental demonstration of thermoacoustic energy conversion in a resonator." *Physical Review E*, vol. 69, 2004.

[45] S. Backhaus and G. W. Swift, "New varieties of thermoacoustic engines." in 9th *International Congress on Sound and Vibration*, 2002.

[46] J. Wheatley, T. Hofler, G. W. Swift, and A. Migliori, "Experiments with an intrinsically irreversible acoustic heat engine." *Physical Review Letters*, vol. 50, no. 7, 1983.

[47] P. H. Ceperly, "A pistonless Stirling engine − The traveling wave heat engine." *Journal of the Acoustical Society of America*, vol. 66, pp. 1508–1513, 1979.

[48] S. Backhaus, E. Tward, and M. Petach, "Traveling-wave thermoacosutic electric generator." *Applied Physics Letters*, vol. 85, no. 6, 2004.

[49] S. Backhaus and G. W. Swift, "A thermoacosutic-Stirling heat engine: Detailed study." *Journal of the Acoustical Socienty of America*, vol. 107, no. 6, pp. 3148–3166, 2000.

[50] M. E. H. Tijani, S. Vanapalli, and S. Spoelstra, "Design of a mechanical resonator to be coupled to a thermoacoustic Stirling engine." in *Proceedings of the ASME 2010 3rd Joint US − European Fluids Engineering Summer Meeting and*

8th *International Conference on Nanochannels, Microchannels and Minichannals, Montreal*, 2010.

[51] R. C. Tew and M. B. Ibrahim, "Two-dimensional compressible non-acoustic modeling of Stirling machine-type components." *Journal of Propulsion and Power*, vol. 19, no. 5, 2003.

[52] J. G. Schreiber, L. G. Tieme, and L. S. Mason, "Status of free-piston Stirling power conversion in the United States Space Program." in *Proceedings of the 10th International Stirling Engine Conference, Osnabrück*, 2001.

[53] P. Neveu and C. Babo, "A simplified model for pulse tube refrigeration." *Cryogenics*, vol. 40, pp. 191–201, 2000.

[54] S. K. Andersen, H. Carlsen, and P. G. Thomsen, "Control volume based modelling in one space dimension of oscillating, compressible flow in reciprocating machines." *Simulation Modelling Practice and Theory*, vol. 14, pp. 1073–1086, 2006.

[55] M. J. Moran and H. N. Shapiro, *Fundamentals of Engineering Thermodynamics.* New York: John Wiley & Sons, 1998.

[56] H. K. Iben and J. Schmidt, *Starthilfe Thermodynamik.* Leipzig: B. G. Teubner, 1999.

[57] E. P. Gyftopoulos and G. P. Beretta, *Thermodynamics, Foundations and Applications.* New York: Dover Publications, 2005.

[58] W. M. Kays and A. L. London, *Hochleistungswärmeübertrager.* Berlin: Akademie – Verlag, 1973.

[59] A. R. Ghahremani, M. H. Saidi, and M. Ebrahimian, "Simultaneous analytical solution of the complete system of double-inlet pulse tube refrigerator." *Journal of Thermophysics and Heat Transfer*, vol. 17, pp. 337–344, 2012.

[60] J. Yuan and J. M. Pfotenhauer, "Thermodynamic analysis of active valve pulse tube refrigerators." *Cryogenics*, vol. 39, pp. 283–292, 1999.

[61] A. J. Organ, *The Regenerator and the Stirling Engine.* London: Mechanical Engineering Publications, 1997.

[62] L. Bauwens, "Near-isothermal regenerator: Complete thermal characterization." *Journal of Thermophysics and Heat Transfer*, vol. 12, no. 3, pp. 414–422, 1998.

[63] ——, "The near-isothermal regenerator: A perturbation analysis." in *DOI: 10.2514/6.1994-4035*, 1994.

[64] A. Thess, *The Entropy Principle, Thermodynamics for the Unsatified.* Berlin: Springer − Verlag, 2011.

[65] I. N. Bronstein, K. A. Semendjajew, G. Musiol, and H. Mühlig, *Taschenbuch der Mathematik.* Frankfurt am Main: Verlag Harri Deutsch, 2001.

[66] E. J. Hinch, *Perturbation Methods.* Cambridge: Cambridge University Press, 1991.

[67] W. H. Press, S. Teukolsky, W. T. Vetterling, and B. P. Flannery, *Numerical Recipes.* Cambridge: Cambridge University Press, 1992.

[68] C. Hirsch, *Numerical Computation of Internal and External Flows, Volume 1: Fundamental of Discretization.* New York: John Wiley & Sons, 1997.

[69] S. V. Patankar, *Numerical Heat Transfer and Fluid Flow.* New York: McGraw − Hill, 1980.

[70] J. B. Heywood and E. Sher, *The two-stroke cycle engine: its development, operation, and design.* Philadelphia: Taylor & Francis, 1999.

[71] R. A. Ackermann, *Cryogenic Regenerative Heat Exchangers.* New York: Plenum Press, 1997.

[72] T. S. Zhao and P. Cheng, "Oscillatory pressure drops throught a woven-screen packed column subjected to a cyclic flow." *Cryogenics*, vol. 36, pp. 843–847, 1998.

[73] C. Hirsch, *Numerical Computation of Internal and External Flows, Volume 2: Computation Methods for Inviscid and Viscous Flows.* New York: John Wiley & Sons, 1997.

[74] F. P. Incopera and D. P. DeWitt, *Fundamentals of Heat and Mass Transfer.* New York: John Wiley & Sons, 1996.

[75] N.N., *VDI Wärmeatlas.* Düsseldorf: VDI − Verlag, 1994.

[76] G. Benvenuto and F. de Monte, "Analysis of free-piston Stirling engine/linear alternator systems part 2: Results." *Journal of Propulsion and Power*, vol. 11, no. 5, 1995.

[77] T. Stark, "Experimentelle Charakterisierung eines Pulsrohrmotors." *Bachelor Thesis, Ilmenau University of Technology*, 2012.

[78] I. Rühlig, *Strömungstechnische Optimierung von Regeneratoren für Gaskältemaschinen.* Düsseldorf: VDI − Verlag, 1999.

[79] W. Albring, *Angewandte Strömungslehre.* Berlin: Akademie − Verlag, 1978.

[80] J. C. Ward, "Turbulent flow in porous media." *ASCE Journal of the Hydraulics Division*, vol. 90, pp. 1–12, 1964.

[81] I. F. Macdonald, M. S. El-Sayed, K. Mow, and F. A. L. Dullien, "Flow through porous media − Ergun equation revisited." *Industrial Engineering and Chemical Fundamentals*, vol. 19, pp. 199–208, 1979.

[82] S. Moldenhauer and T. Stark, "Vorrichtung und Verfahren zur Erzeugung einer Kälteleistung." Patent DE 102 013 005 304.8, 2013.

[83] S. Moldenhauer, A. Thess, C. Holtmann, and C. Fernándes-Aballí, "Thermodynamic analysis of a pulse tube engine." *Journal of Energy Conversion and Management*, vol. 65, pp. 810–818, 2013.

[84] S. Moldenhauer, C. Holtmann, T. Stark, and A. Thess, "Theoretical and experimental investigations of the pulse tube engine." *Journal of Thermophysics and Heat Transfer, DOI: 10.2514/1.T4021.*

[85] S. Moldenhauer, T. Stark, C. Holtmann, and A. Thess, "The pulse tube engine: A numerical and experimental approach on its design, performance, and operating conditions." *Energy, DOI: 10.1016/j.energy.2013.03.052.*

[86] S. Moldenhauer, "Analytical model of the pulse tube engine." *submitted to Energy.*

[87] A. Thess, S. Moldenhauer, and T. Stark, "Vorrichtung und Verfahren zur Erzeugung eines heißen Luftstroms." Patent DE 102 012 002 440.1, 2012.

[88] S. Moldenhauer, "Vorrichtung und Verfahren zur Nutzung der Abgaswärme eines Verbrennungsmotors." Patent DE 102 013 002 974.0, 2013.

[89] S. Moldenhauer and A. Thess, "Modelica based simulation model of a pulse tube engine." in *Proceedings of the 13th ITI − Symposium, Dresden*, 2010, pp. 178–182.

[90] ———, "Thermodynamic analysis of a pulse tube engine for waste heat usage." in *Proceedings of the Global Conference on Renewables and Energy Efficiency for Desert Regions, Amman*, 2011.

[91] S. Moldenhauer, C. Holtmann, and A. Thess, "Entwicklung eines Pulsrohrmotors." in *Thermodynamik-Kolloquium, Frankfurt/Main*, 2011, p. 120.

[92] S. Moldenhauer, "Modelica based simulation model of a pulse tube engine." in *Journée Thermoacoustique, Paris*, 2010.

[93] S. Moldenhauer, C. Holtmann, T. Stark, and A. Thess, "Theoretical and experimental investigations of the pulse tube engine." in *Proceedings of the 10th International Energy Conversion Engineering Conference, Atlanta*, 2012.

[94] S. Moldenhauer and A. Thess, "Simplified analysis of a pulse tube engine." in *Proceedings of the 7th International Conference for Renewable Energy, Energy Saving and Energy Education CIER, Havana*, 2011.

[95] S. Moldenhauer, C. Holtmann, and A. Thess, "Extended simulation model of a pulse tube engine." in *4th German − Jordan Workshop: The potential of CSP and Solar Applications in Jordan, Amman*, 2012.

[96] C. Holtmann, "Entwicklung eines Experimentallineargenerators zur Anwendung an einem Pulsrohrmotor." *Master Thesis, Ilmenau University of Technology*, 2012.

[97] J. Wang, W. Wang, G. W. Jewell, and D. Howe, "A low-power, linear, permanent-magnet generator/energy storage system." in *IEEE Transactions on Industrial Electronics*, vol. 49, no. 3, 2002, pp. 640–648.

[98] I. Boldea and S. A. Nasar, *Linear electric actuators and generators.* Cambridge: Cambridge University Press, 1997.

[99] T. Köttig, S. Moldenhauer, R. Nawrodt, M. Thürk, and P. Seidel, "Two-stage pulse tube refrigerator in an entire coaxial configuration." *Cryogenics*, vol. 46, pp. 888–891, 2006.

[100] T. Köttig, S. Moldenhauer, M. Patze, M. Thürk, and P. Seidel, "Investigation on the internal thermal link of pulse tube refrigerators." *Cryogenics*, vol. 47, pp. 137–142, 2007.

[101] S. Moldenhauer, "Numerische und experimentelle Untersuchungen zu den thermodynamischen und strömungsmechanischen Vorgängen in einem Vier-Ventil-Pulsationsröhrenkühler." *Diploma Thesis, University of Jena*, 2005.